

FEDERAL UNIVERSITY OF ABC

Graduate Program in Nanoscience and Advanced Materials

**Titanato de Lantânio e Estrôncio dopado com Cobre e Níquel:
síntese, caracterização e exsolução de nanopartículas para
eletrodos de célula de combustível de óxido sólido**

Antonio Teofanes Bertollo de Oliveira

Advisor:

Prof. Dr. Daniel Zanetti de Florio

Santo André - SP

2023

Antonio Teofanes Bertollo de Oliveira

**Titanato de Lantânio e Estrôncio dopado com Cobre e Níquel:
síntese, caracterização e exsolução de nanopartículas para
eletrodos de célula de combustível de óxido sólido**

Thesis presented to the Nanosciences and Advanced Materials Graduate Program of the Federal University of ABC as a partial requirement to obtain the title of Master of Science in Nanoscience and Advanced Materials.

Advisor: Prof. Dr. Daniel Zanetti de Florio

Santo André - SP

2023

Sistema de Bibliotecas da Universidade Federal do ABC

Elaborada pelo Sistema de Geração de Ficha Catalográfica da UFABC
com os dados fornecidos pelo(a) autor(a).

Oliveira, Antonio

Titanato de Lantânio e Estrôncio dopado com Cobre e
Níquel : síntese, caracterização e exsolução de
nanopartículas para eletrodos de célula de combustível de
óxido sólido / Antonio Oliveira. — 2023.

105 fls. : il.


Orientador: Daniel Zanetti De Florio

Dissertação (Mestrado) — Universidade Federal do ABC,
Programa de Pós-Graduação em Nanociências e Materiais
Avançados, Santo André, 2023.

1. Exsolução. 2. Perovskitas. 3. SOFC. I. De Florio,
Daniel Zanetti. II. Programa de Pós-Graduação em
Nanociências e Materiais Avançados, 2023. III. Título.

Este exemplar foi revisado e alterado em relação à versão original, de acordo com as observações levantadas pela banca examinadora no dia da defesa, sob responsabilidade única do(a) autor(a) e com a anuência do(a) (co)orientador(a).

Santo andré, 15 de Setembro de 2023

 Documento assinado digitalmente
ANTONIO TEOFANES BERTOLLO DE OLIVEIRA
Data: 25/09/2023 11:13:39-0300
Verifique em <https://validar.itl.gov.br>

Assinatura do(a) autor(a): _____

 Documento assinado digitalmente
DANIEL ZANETTI DE FLORIO
Data: 25/09/2023 13:44:09-0300
Verifique em <https://validar.itl.gov.br>

Assinatura do(a) orientador(a): _____



MINISTÉRIO DA EDUCAÇÃO
Fundação Universidade Federal do ABC
Avenida dos Estados, 5001 – Bairro Santa Terezinha – Santo André – SP
CEP 09210-580 · Fone: (11) 4996-0017

FOLHA DE ASSINATURAS

Assinaturas dos membros da Banca Examinadora que avaliou e aprovou a Defesa de Dissertação de Mestrado do candidato, ANTONIO TEOFANES BERTOLLO DE OLIVEIRA realizada em 06 de Setembro de 2023:

Documento assinado digitalmente
gov.br **CRISTIANE BARBIERI RODELLA**
Data: 11/09/2023 11:55:56-0300
Verifique em <https://validar.itl.gov.br>

Prof.(a) CRISTIANE BARBIERI RODELLA
CENTRO NACIONAL DE PESQUISA EM ENERGIA E MATERIAIS

Documento assinado digitalmente
gov.br **MARCIA TSUYAMA ESCOTE**
Data: 11/09/2023 15:01:36-0300
Verifique em <https://validar.itl.gov.br>

Prof.(a) MARCIA TSUYAMA ESCOTE
UNIVERSIDADE FEDERAL DO ABC

Prof.(a) FÁBIO CORAL FONSECA
INSTITUTO DE PESQUISAS ENERGÉTICAS E NUCLEARES

Prof.(a) JOSE ANTONIO SOUZA
UNIVERSIDADE FEDERAL DO ABC

Documento assinado digitalmente
gov.br **DANIEL ZANETTI DE FLORIO**
Data: 07/09/2023 12:20:49-0300
Verifique em <https://validar.itl.gov.br>

Prof.(a) DANIEL ZANETTI DE FLORIO
UNIVERSIDADE FEDERAL DO ABC - Presidente

* Por ausência do membro titular, foi substituído pelo membro suplente descrito acima: nome completo, instituição e assinatura



Universidade Federal do ABC

Financial Support:

The author gratefully acknowledges the Human Resources Program – National Oil Agency (PRH/ANP) for the funding to support the development of this project.

This study was financed in part by the Coordenação de Aperfeiçoamento de Pessoal de Nível Superior – Brasil (CAPES) – Finance Code 001

ACKNOWLEDGEMENT

I would like to first thank my family. To my father and mother, the greatest supporters of my dreams, who never hesitated in making any effort so that I could become who I am today. There are no words to describe all the love, care, affection, and education you have always given me. I am immensely grateful to my beloved partner, Emmanoely, for always being by my side during the most painful and joyful moments of this journey.

To Professor Daniel, who opened the doors of academic life for me, contributing to the development of my research and my personal life, I will be eternally grateful. I also thank Professor Fábio Furlan for the discussions, teachings, and all the help with the refinement of crystal structures.

To my laboratory friends André, Arthur, Bria, Chrystian, Dani, Diego, Débora, Fernando, Renata, Sérgio, and Suzane, you were fundamental to my scientific and personal development. I will cherish every conversation, advice, and lesson shared in these last two years. My sincerest gratitude to all of you.

To my friend since graduation and housemate who embarked with me on this journey, Maycom, thank you so much for being a support and companion during the toughest and happiest moments of these last two years.

To my friend Nathália, who helped, supported, and taught me so much, thank you for all the help with data analysis, encouragement, and teaching of techniques I had never heard of before.

I am grateful to the Federal University of ABC and the Multiuser Experimental Center, to all the professors and technicians in the nanosciences and advanced materials program for all their hard work and dedication.

“Eu sou a continuação de um sonho”

Abebe Bikila

RESUMO

A mudança climática tornou-se uma das maiores preocupações do século devido a possibilidade de aumento de 1,5 °C na temperatura média global, resultando em um impacto profundo na ocorrência de eventos naturais extremos. Nos últimos anos, esforços consideráveis têm sido direcionados para limitar as emissões de carbono, principalmente por meio da substituição da matriz energética baseada em combustíveis fósseis. As Células a Combustível de Óxido Sólido (CCOS) são dispositivos que convertem energia química em energia elétrica com alta eficiência, flexibilidade de combustível e baixa, ou nula, geração de emissões de CO₂. Devido a essas características, as CCOS são consideradas uma alternativa promissora para a substituição da combustão térmica. Os anodos destes dispositivos tem como principal função a oxidação do combustível. Entre os diversos materiais que podem ser aplicados para esse fim, perovskitas destacam-se como um material promissor devido à sua alta condutividade mista, propriedades catalíticas e estabilidade química e térmica. Neste trabalho, o foco está na obtenção de nanopartículas de níquel e cobre ancoradas na superfície de perovskitas cerâmicas, com o objetivo de explorar um material promissor, como anodo de CCOS, pouco explorado na literatura. As composições de $\text{La}_{0.8}\text{Sr}_{0.2}\text{Ti}_{0.7}\text{Ni}_{0.3-x}\text{Cu}_x\text{O}_{3-\delta}$ ($x = 0.1, 0.15, 0.2$) e $\text{La}_{1.2}\text{Sr}_{0.7}\text{Ni}_{0.5}\text{Cu}_{0.5}\text{O}_4$ foram obtidas por meio do método de Pechini modificado e calcinadas a 900 °C por 5 horas. A produção de nanopartículas exsolvidas de NiCu envolveu o tratamento térmico dos pós em uma atmosfera redutora de 3 % vol H₂/N₂ a 900 °C, 850 °C, 800 °C e 750 °C por 10 horas. As amostras foram caracterizadas por termogravimetria e análise térmica diferencial (TGA/DTA), dilatometria, microscopia eletrônica de varredura (MEV), microscopia eletrônica de transmissão (MET), difração de raios X (DRX), espectroscopia de fotoelétrons excitados por raios X (XPS) e espectroscopia de impedância eletroquímica (EIS). As análises de DRX e XPS confirmaram a presença da liga níquel e cobre usando a rota de síntese escolhida e o tratamento de redução. Informações estruturais tais como, parâmetros de redes, tamanho de cristalito e teor de fase, foram determinados usando o refinamento Rietveld nos resultados de DRX. O MEV revelou a presença de nanopartículas esféricas ancoradas na superfície da amostra, e a MET confirmou a composição das nanopartículas de liga de NiCu. Palavras-chave: Perovskitas, Célula a combustível de óxido sólido, Exsolução.

ABSTRACT

Climate emergency has become the most significant concern of the century due to the 1.5 °C increase in the average atmospheric temperature, resulting in a profound impact on natural events. In recent years, considerable efforts have been directed towards achieving net-zero emissions, primarily through the substitution of fossil fuels with decarbonization. Solid oxide fuel cells (SOFCs) are devices that efficiently convert chemical energy into electrical energy, offering fuel flexibility and generating low to zero CO₂ emissions. Due to these features, SOFCs are considered a promising alternative to fossil fuels machines. SOFC anodes play a crucial role in catalyzing fuel oxidation. Among the materials used for this purpose, ceramic perovskites stand out as excellent electrodes due to their high mixed ionic-electronic conductivity, chemical and thermal stabilities, and strong catalytic properties. In this study, our focus is on obtaining exsolved metal alloy nanoparticles anchored to perovskite structures, exploring a more promising, challenging, and less explored material in the existing literature. La_{0.8}Sr_{0.2}Ti_{0.7}Ni_{0.3-x}Cu_xO_{3-δ} (x = 0.1, 0.15, 0.2) and La_{1.2}Sr_{0.7}Ni_{0.5}Cu_{0.5}O₄ samples were obtained through the Pechini synthesis route and were calcined at 900 °C for 5 hours. The production of decorated NiCu nanoparticles involved heat-treating the powders in a 3 vol % H₂/N₂ atmosphere at 900 °C, 850 °C, 800 °C, and 750 °C for 10 hours. The samples were subjected to various characterization techniques, including thermogravimetry (TG/DTA), dilatometry, scanning electron microscopy (SEM), transmission electron microscopy (TEM), X-ray diffraction (XRD), X-ray photoelectron spectroscopy (XPS), and electrochemical impedance spectroscopy (EIS). XRD and XPS analyses confirmed the successful formation of NiCu alloy particles using the chosen synthesis route and the reduction treatment. Structural parameters such as crystal symmetry, crystallite size, and phase content were determined using Rietveld's refinement. SEM revealed the presence of spherical nanoparticles anchored on the sample surface, and TEM confirmed the composition of copper-nickel alloy nanoparticles.

Keywords: Perovskites, Solid oxide fuel cell, Exsolution.

FIGURES INDEX

Figure 1: The global primary energy consumption by source (a) and the global average temperature anomaly (b) ^{20,21}	24
Figure 2: Schematic diagram of Solid Oxide Fuel Cells (a) represents an oxygen ion conduction electrolyte and (b) a protonic fuel cell (adapted) ³⁵	26
Figure 3: Schematic structure of cubic perovskite (ABO_3) ⁷⁴	32
Figure 4: Ruddlesden-Popper phase structure ¹⁴	34
Figure 5: Schematic diagram of exsolution process ⁴⁷	39
Figure 6: (a) schematic diagram showing the difference between the anchored and deposited nanoparticle ¹²⁸ (b) transmission microscopy image showing the alignment between the crystallographic planes of the host solid oxide and the nanoparticles ¹³⁰	40
Figure 7: Gibbs free energy relative to particle radius during the process of nucleation and growth ¹⁴¹	42
Figure 8: Stages of synthesis	46
Figure 9: TG/DTA data of $\text{La}_{0.8}\text{Sr}_{0.2}\text{Ti}_{0.7}\text{Ni}_{0.15}\text{Cu}_{0.15}\text{O}_{3-\delta}$ synthesized by Pechini method.	51
Figure 10: XRD pattern after calcination at 900 °C for 5 h. The diffraction position corresponding to the centered cubic LaTiO_3 structure is highlighted with an orange circle.....	52
Figure 11: Ruddlesden-Popper phase XRD pattern after calcination at 900 °C for 5 h. The diffraction position corresponding to the tetragonal $\text{La}_{1.5}\text{Sr}_{0.5}\text{Ni}_{0.5}\text{Cu}_{0.5}\text{O}_4$ structure is highlighted with a blue square.	53
Figure 12: Rietveld pattern refinement of $\text{La}_{0.8}\text{Sr}_{0.2}\text{Ti}_{0.7}\text{Ni}_{0.1}\text{Cu}_{0.2}\text{O}_{3-\delta}$ as the cubic phase (Pm-3m). The observed XRD pattern is shown with black cruise points, the red line represents the theoretical model while the blue line shows the difference between the theoretical model and the experimental data. Finally, the expected peaks positions are shown above in green bars.....	54
Figure 13: XRD pattern after reduction treatment at 900 °C for 10 h. The diffraction position corresponding to the centered cubic LaTiO_3 structure is highlighted with an orange circle, while the green circle indicates the diffraction position associated with the centered cubic Nickel-Copper alloy.	56

Figure 14: XRD pattern after reduction treatment at 850 °C for 10 h. The diffraction position corresponding to the centered cubic LaTiO ₃ structure is highlighted with an orange circle, while the green circle indicates the diffraction position associated with the centered cubic Nickel-Copper alloy.	57
Figure 15: XRD pattern after reduction treatment at 800 °C for 10 h. The diffraction position corresponding to the centered cubic LaTiO ₃ structure is highlighted with an orange circle, while the green circle indicates the diffraction position associated with the centered cubic Nickel-Copper alloy.	57
Figure 16: XRD pattern after reduction treatment at 750 °C for 10 h. The diffraction position corresponding to the centered cubic LaTiO ₃ structure is highlighted with an orange circle, while the green circle indicates the diffraction position associated with the centered cubic Nickel-Copper alloy.	58
Figure 17: Rietveld pattern refinement of La _{0.8} Sr _{0.2} Ti _{0.7} Ni _{0.15} Cu _{0.15} O _{3-δ} as the cubic phase (Pm-3m) after reduction treatment at 800 °C. The observed XRD pattern is shown with x points within the theoretical model, the blue line shows the difference between the theoretical model and the experimental data. Finally, the expected peaks positions are shown above in green bars.	59
Figure 18: XRD pattern of RP-phase after reduction treatment at 900 °C for 10 h. The diffraction position corresponding to the La ₂ SrO _x structure is highlighted with a black circle, while the green circle indicates the diffraction position associated with the centered cubic Nickel-Copper alloy.....	60
Figure 19 – High-resolution and deconvoluted XPS spectra of Ni 3p spectra of RP phase as prepared and after reduction treatment at 900 °C.....	62
Figure 20 – High-resolution and deconvoluted XPS spectra of Ni 2p _{3/2} and La 3d _{3/2} spectra of La _{0.8} Sr _{0.2} Ti _{0.7} Ni _{0.15} Cu _{0.15} O _{3-δ} as prepared and after reduction treatment at 900 °C.	63
Figure 21: High-resolution and deconvoluted XPS spectra of Cu 2p _{3/2} spectra of RP phase as prepared and after reduction treatment at 900 °C.....	64
Figure 22: High-resolution and deconvoluted XPS spectra of Cu 2p _{3/2} spectra of La _{0.8} Sr _{0.2} Ti _{0.7} Ni _{0.15} Cu _{0.15} O _{3-δ} as prepared and after reduction treatment at 900 °C.	65
Figure 23: High-resolution and deconvoluted XPS spectra of Ti 2p _{3/2} spectra of La _{0.8} Sr _{0.2} Ti _{0.7} Ni _{0.15} Cu _{0.15} O _{3-δ} after reduction treatment at 900 °C.....	66

Figure 24: $\text{La}_{0.8}\text{Sr}_{0.2}\text{Ti}_{0.7}\text{Ni}_{0.1}\text{Cu}_{0.2}\text{O}_{3-\delta}$ calcined at 900 °C for 5 hours. Image obtained with 3 kV acceleration voltage.	67
Figure 25: Scanning Electron Images of treatment $\text{La}_{0.8}\text{Sr}_{0.2}\text{Ti}_{0.7}\text{Ni}_{0.15}\text{Cu}_{0.15}\text{O}_{3-\delta}$ (a), $\text{La}_{0.8}\text{Sr}_{0.2}\text{Ti}_{0.7}\text{Ni}_{0.2}\text{Cu}_{0.1}\text{O}_{3-\delta}$ (b), $\text{La}_{0.8}\text{Sr}_{0.2}\text{Ti}_{0.7}\text{Ni}_{0.1}\text{Cu}_{0.2}\text{O}_{3-\delta}$ (c) after reduction at 750 °C.	68
Figure 26: Scanning Electron Images of treatment $\text{La}_{0.8}\text{Sr}_{0.2}\text{Ti}_{0.7}\text{Ni}_{0.15}\text{Cu}_{0.15}\text{O}_{3-\delta}$ (a), $\text{La}_{0.8}\text{Sr}_{0.2}\text{Ti}_{0.7}\text{Ni}_{0.2}\text{Cu}_{0.1}\text{O}_{3-\delta}$ (b), $\text{La}_{0.8}\text{Sr}_{0.2}\text{Ti}_{0.7}\text{Ni}_{0.1}\text{Cu}_{0.2}\text{O}_{3-\delta}$ (c) after reduction at 800 °C.	68
Figure 27: Scanning Electron Images of treatment $\text{La}_{0.8}\text{Sr}_{0.2}\text{Ti}_{0.7}\text{Ni}_{0.15}\text{Cu}_{0.15}\text{O}_{3-\delta}$ (a), $\text{La}_{0.8}\text{Sr}_{0.2}\text{Ti}_{0.7}\text{Ni}_{0.2}\text{Cu}_{0.1}\text{O}_{3-\delta}$ (b), $\text{La}_{0.8}\text{Sr}_{0.2}\text{Ti}_{0.7}\text{Ni}_{0.1}\text{Cu}_{0.2}\text{O}_{3-\delta}$ (c) after reduction at 850 °C.	68
Figure 28: Scanning Electron Images of treatment $\text{La}_{0.8}\text{Sr}_{0.2}\text{Ti}_{0.7}\text{Ni}_{0.15}\text{Cu}_{0.15}\text{O}_{3-\delta}$ (a), $\text{La}_{0.8}\text{Sr}_{0.2}\text{Ti}_{0.7}\text{Ni}_{0.2}\text{Cu}_{0.1}\text{O}_{3-\delta}$ (b), $\text{La}_{0.8}\text{Sr}_{0.2}\text{Ti}_{0.7}\text{Ni}_{0.1}\text{Cu}_{0.2}\text{O}_{3-\delta}$ (c) after reduction at 900 °C.	69
Figure 29: Scanning Electron Images of treatment $\text{La}_{1.2}\text{Sr}_{0.7}\text{Ni}_{0.5}\text{Cu}_{0.5}\text{O}_{4+x\delta}$ after reduction at 900 °C.	70
Figure 30: High Resolution Transmission Electron Images (HRTEM) of $\text{La}_{0.8}\text{Sr}_{0.2}\text{Ti}_{0.7}\text{Ni}_{0.2}\text{Cu}_{0.1}\text{O}_{3-\delta}$ after reduction treatment at 800 °C for 10 hours. ...	71
Figure 31: High Resolution Transmission Electron Images (HRTEM) of $\text{La}_{0.8}\text{Sr}_{0.2}\text{Ti}_{0.7}\text{Ni}_{0.15}\text{Cu}_{0.15}\text{O}_{3-\delta}$ after reduction treatment at 800 °C for 10 hours. .	72
Figure 32: High Resolution Transmission Electron Images (HRTEM) of $\text{La}_{0.8}\text{Sr}_{0.2}\text{Ti}_{0.7}\text{Ni}_{0.1}\text{Cu}_{0.2}\text{O}_{3-\delta}$ after reduction treatment at 800 °C for 10 hours. ...	73
Figure 33: STEM-HAADF image of $\text{La}_{0.8}\text{Sr}_{0.2}\text{Ti}_{0.7}\text{Ni}_{0.15}\text{Cu}_{0.15}\text{O}_{3-\delta}$ after reduction treatment at 800 °C for 10 hours	74
Figure 34: Dilatometry curve of $\text{La}_{1.2}\text{Sr}_{0.7}\text{Cu}_{0.5}\text{Ni}_{0.5}\text{O}_{4\pm\delta}$ from room temperature to 1500 °C in nitrogen.	75
Figure 35: Ruddlesden-popper phase isothermal curve in 1150 °C for 2 h in function of sample density	75
Figure 36: Dilatometry curve of $\text{La}_{0.8}\text{Sr}_{0.2}\text{Ti}_{0.7}\text{Ni}_{0.15}\text{Cu}_{0.15}\text{O}_{3-\delta}$ from room temperature to 1500 °C in nitrogen.	76
Figure 37: $\text{La}_{0.8}\text{Sr}_{0.2}\text{Ti}_{0.7}\text{Ni}_{0.15}\text{Cu}_{0.15}\text{O}_{3-\delta}$ Isothermal curve in 1150 °C for 2 h in function of sample density	77
Figure 38: Cooling ramp of $\text{La}_{0.8}\text{Sr}_{0.2}\text{Ti}_{0.7}\text{Ni}_{0.15}\text{Cu}_{0.15}\text{O}_{3-\delta}$	77

Figure 39: The Nyquist diagram of $\text{La}_{0.8}\text{Sr}_{0.2}\text{Ti}_{0.7}\text{Ni}_{0.1}\text{Cu}_{0.2}\text{O}_{3.5}$ impedance at 300 °C	79
Figure 40: Arrhenius plot of total conductivity with variation of reciprocal temperature.....	81
Figure 41: Total conductivity of $\text{La}_{1.2}\text{Sr}_{0.7}\text{Ni}_{0.5}\text{Cu}_{0.5}\text{O}_4$ from 400 °C to 650 °C in static air	82
Figure 42: Arrhenius plot of total conductivity with variation of reciprocal temperature under 3% H_2 – 97% N_2 atmosphere.	83

TABLE INDEX

Table 1: Samples and treatments	46
Table 2: Data obtained through Rietveld refinement after powder calcined at 900 °C.	54
Table 3: Data obtained through Rietveld refinement after reduction treatment of all compositions at 900 °C, 850 °C, 800 °C, and 750 °C.	59
Table 4: XPS fitting results of Cu 2p, Ni 3p, and Ti 2p proportions as prepared and after reduction treatment.	65
Table 5: Temperature (K), DC resistance ($\Omega \text{ cm}^{-1}$), and total conductivity (S cm^{-1}) for each sample	79
Table 6: Temperature (K), DC resistance ($\Omega \text{ cm}^{-1}$), and total conductivity (S cm^{-1}) and activation energy for $\text{La}_{1.2}\text{Sr}_{0.7}\text{Ni}_{0.5}\text{Cu}_{0.5}\text{O}_4$	83

ABBREVIATIONS

EIS	Electrochemical impedance spectroscopy
EDX	Energy dispersive X-ray
GDC	Gadolinium doped ceria
GHG	Greenhouse gas
HAADF	High-angle annular dark-field
HRTEM	High-resolution transmission electron microscopy
HT-SOFC	High-temperature solid oxide fuel cell
IEA	International energy agency
IT-SOFC	Intermediate temperature solid oxide fuel cell
LT-SOFC	Low-temperature solid oxide fuel cell
MIEC	Mixed ionic-electronic conduction
ORR	Oxygen reduction reaction
SOFC	Solid oxide fuel cell
SEM	Scanning electron microscope
STEM	Scanning transmission electron microscope
TEM	Transmission electron microscope
TG	Thermogravimetric analysis
TPB	Triple-phase-boundary
XRD	X-ray diffraction
XPS	X-ray photoelectron spectroscopy
YSZ	Yttria-stabilized zirconia

Summary

1.	Introduction	21
2.	Literature Review	23
2.1	Global climate change and new energies.....	23
2.2	Solid Oxide Fuel Cell.....	25
2.2.1	Anodes	27
2.2.2	Electrolyte	29
2.2.3	Cathodes	30
2.3	Perovskites for new energy	31
2.3.1	Ruddlesden-Popper phase	33
2.3.2	Doping in perovskites	35
2.3.3	Lanthanum titanate, nickelate and cuprate systems.....	36
2.4	Exsolution.....	37
3.	Objectives	44
4.	Materials and Methods.....	45
4.1	Synthesis and methods	45
4.2	Characterization	46
4.2.1	Thermogravimetric analysis (TGA)	46
4.2.2	X-ray diffraction (XRD).....	46
4.2.3	X-ray photoelectron spectroscopy (XPS)	47
4.2.4	Scanning electron microscope (SEM).....	48
4.2.5	Transmission electron microscopy (TEM).....	48
4.2.6	Dilatometry analysis.....	49
4.2.7	Electrochemical impedance spectroscopy (EIS).....	49
5.	Results and discussions.....	50
5.1	Structure and morphology	50
5.1.1	Thermogravimetry analysis.....	51

5.1.2	X-ray diffraction.....	52
5.1.2.1	Calcined samples	52
5.1.2.2	Reduced samples.....	56
5.1.3	X-ray photoelectron spectroscopy	61
5.1.4	Electron Microscopy	66
5.1.4.1	Scanning Electron Microscopy (SEM)	67
5.1.4.2	Transmission Electron Microscopy (TEM)	70
5.1.5	Dilatometry	74
5.2	Electrical properties.....	78
6.	Conclusion	85
7.	Future work	87
8.	Awards, congress, events, and schools	88
	Bibliography.....	89
	Appendix 1	103

1. Introduction

The emergence to stop the emission of greenhouse gases (GHG) is unquestionable. The growth of GHG emissions in recent years places us in a global climate emergency, with the mission to stop the increase in the average warming of the earth's atmosphere and the possible catastrophic impacts generated¹. According to the International Energy Agency (IEA), in 2019, about 77% of the world's energy matrix was composed of oil, derivatives, and natural gas. In this context, several global efforts have been agreed to seek a reduction in emissions, through a decrease in the dependence of fossil fuels².

One of the main solutions presented to reduce the emissions of GHG is the decarbonization of the entire production chain and the transition of the energy matrix to more sustainable systems. The electrification by use of renewable energy sources, for agricultural, industrial, and transport processes, appears as a potential solution since it has low or zero GHG emissions^{3–6}.

Solid oxide fuel cells (SOFC) are one of the most promising technologies. These devices convert chemical energy from fuel atom bonds to electrical energy with high efficiency. The main components of SOFC are the anode, electrolyte, and cathode, which are composed of ceramics and cermets and operate at temperatures between 500 °C and 1000 °C. One of the advantages related to SOFC, when compared with other systems, is the ability to operate with different fuels, being able to operate with hydrogen, methane, methanol, propane, and alcohol^{7–10}.

In the Brazilian scenario, the ability to operate with ethanol is a great advantage. The country is the second-largest global producer of this fuel, behind only the United States of America (USA). However, there is a big difference between the two markets. In Brazil, the generation of this biofuel is made, almost exclusively, from sugarcane. In the USA, the bigger part of the production is made from corn. This business model brings to Brazil advantages since there is no competition between the food and energy market^{11,12}. Observing this scenario, SOFCs are

presented as an advantageous alternative to the current means of obtaining energy and demonstrates the possibility of producing high chemical values^{2,13}.

Perovskites have been extensively studied and applied in several fields such as biomedical applications, catalysis, batteries, photovoltaics, and fuel cells. This wide range of applications can be attributed to the magnetic and electrical properties of these materials. In general, these structures exhibit good chemical and structural stability, which allows them to be used at high temperatures and over a large range of oxygen partial pressures¹⁴. Strontium-doped lanthanum titanate-based (LSTO) perovskites have been widely studied as anodes for these devices. LSTO exhibits high chemical and structural stability and a thermal expansion coefficient compatible with yttria-stabilized zirconia, a well-known electrolyte for SOFC. However, it exhibits poor electrochemical performance. To overcome it, the B-site doping with transition metals emerges as a possible alternative^{15,16}.

Another promising solution for enhancing electrochemical properties and avoiding coke deposition during operation with carbon-based fuels is the exsolution phenomenon. In this approach, the metal is solubilized in a solid matrix, and thereafter, the solid solution is placed in a reducing environment at a high temperature. Under these conditions, the metal emerges at the surface in the reduced form. This promotes NP anchored in the solid matrix within the coherence of crystallographic planes between the host oxide and the exsolved NP, which changes the material properties¹⁷.

In this present work, the main objective is the development of ceramics of LSTO type to apply as anode of SOFC. The compositions were double doped with nickel and copper at B-site to improve electrochemical performance. The $\text{La}_{0.8}\text{Sr}_{0.2}\text{Ti}_{0.7}\text{Ni}_{0.2-x}\text{Cu}_x\text{O}_{3-\delta}$ ($x = 0.1, 0.15, 0.2$) and $\text{La}_{1.2}\text{Sr}_{0.7}\text{Ni}_{0.5}\text{Cu}_{0.5}\text{O}_4$ samples were synthesized by the polymeric precursor method. The samples were characterized using thermogravimetry, dilatometry, X-ray diffraction, X-ray photoelectron spectroscopy, and scanning electron microscope.

2. Literature Review

The literature review starts with a brief introduction to global climate change and possibilities to overcome the serious problems caused by the global average temperature increase.

The second section introduces the work principles, elements, and state-of-the-art materials used in SOFC. The discussion will bring it up the main current challenges for SOFC operation and the bottlenecks associated with such devices.

In a third moment, the discussion will be about perovskite properties and why this structure stood out and earned huge attention in recent years. This part will bring information about doping strategies and the system that was selected.

Finally, in the last section, the focus will be the exsolution phenomena. The justification to choose exsolution, how it works, which are the main parameters to control, and why this technique has been so relevant in heterogeneous catalysis and electrochemical improvement.

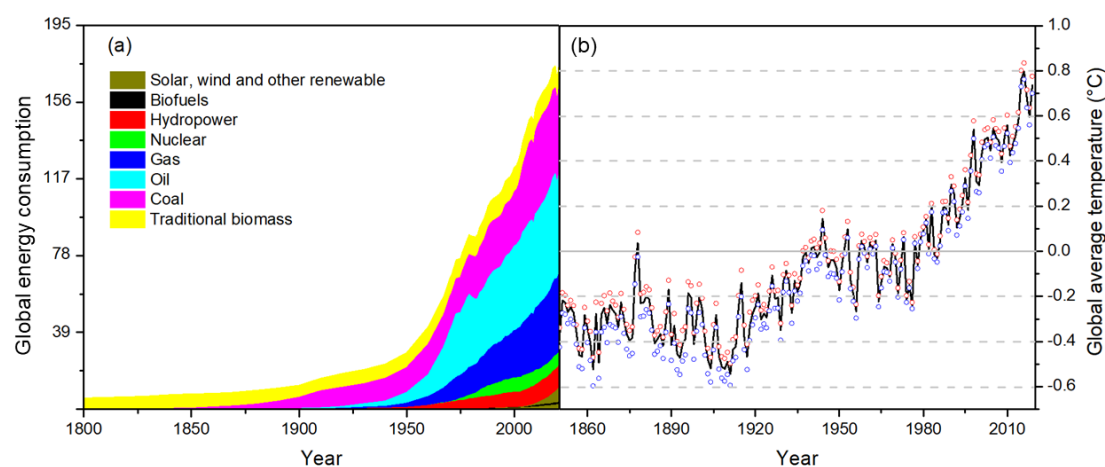
2.1 Global climate change and new energies

Since the end of XIX and beginning of XX century, the average global temperature has changed. The pre-industrial revolution and industrial revolution brought up huge advances in production model and productivity never seen before. However, introduced the steam machine, which led to a wide demand for coal and oil energy supply¹⁸.

Energy production based on carbon fuels is tightly bonded with combustion reactions whereas the main products are carbon dioxide (CO₂), nitrous oxide (N₂O), and carbon monoxide (CO) in low-efficiency motors, these gases are called greenhouse gases (GHG)¹⁹.

The increase of global primary energy consumption by these sources in the last century are shown in **Figure 1a**. As can be observed, since 1950, coal, gas and oil represent at least 60% of global primary energy consumption. In 2021, the last year of actualization, these sources summed to reach about 77% of all global primary energy consumption. The increase in coal, gas and oil global demand is factual and matches with the grow of global temperature average as shown in **Figure 1b**.

Figure 1: The global primary energy consumption by source (a) and the global average temperature anomaly (b)^{20,21}.



According to the last Intergovernmental Panel on Climate Change (IPCC) report, these climate changes in the global context increase the extreme events such as dry and rains severe, coastal erosion and flooding caused by sea level rise and other extreme events.

In the seek for a possible solution, huge efforts and agreements have been made by several countries. One of them is the Paris Agreement, signed by 195 countries in December 2015. The main objective of this accordance is to constraint the global average temperature rises to 2 °C. The solution for this problem goes through the electrification of several economy sectors, such as transportation, agriculture, industry, and residential, to avoid GHG release.

Studies are shown the possibility to integrate new processes of energy production with orthodox energy systems as the main goal to improve its efficiency. This is

possible by photo electrocatalytic water splitting for instance, where it is feasible to use solar energy to splitting water (H_2O) into hydrogen (H_2), that can be used as fuel, and oxygen (O_2)^{22,23}.

An additional realistic solution is SOFC. These devices owing to their high temperature of operation can generate electrical energy and heat. The hot gas that comes out of the device outlet can feed a gas turbine and co-generate energy or even be used for heating in stationary application^{24,25}.

2.2 Solid Oxide Fuel Cell

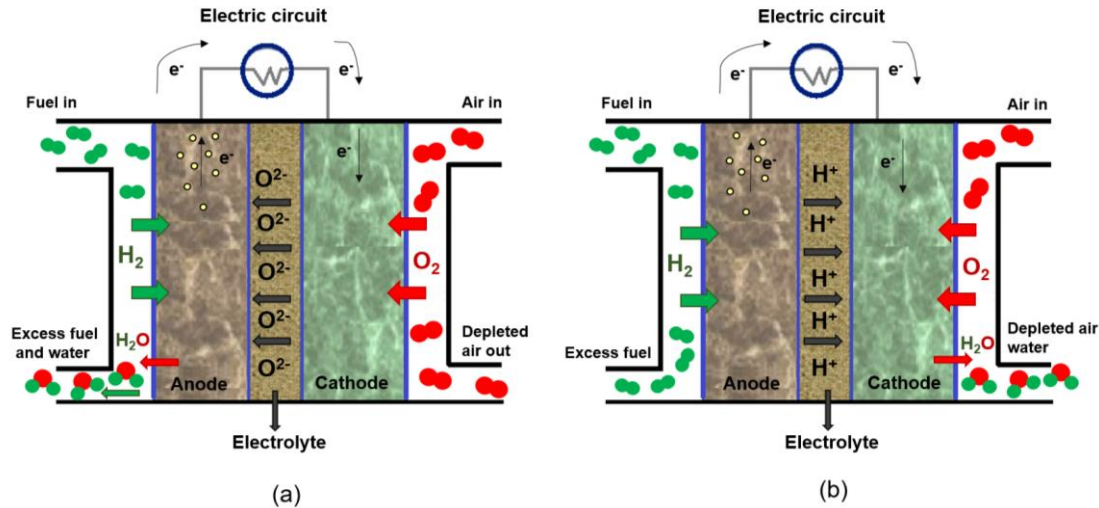
Fuel cells are devices that convert chemical fuels, without combustion, into electrical energy and heat. These electrochemical systems operate on the same principle as batteries. However, unlike these, it has a continuous fuel supply, and the electrodes are not consumed during the reaction^{26–28}.

Due to this electrochemical nature, fuel cells have their efficiency determined by the Gibbs free energy (ΔG) and by the enthalpy variation of the process (ΔH), according to **Equation 1**. Therefore, their efficiency is not determined by the Carnot cycle^{26,29–31}.

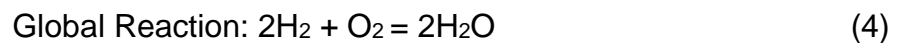
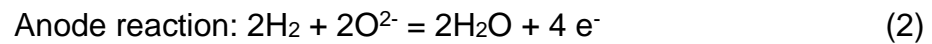
$$\eta = \Delta G / \Delta H \quad (1)$$

In general, fuel cells are composed of three main components: anode, the electrode responsible for the fuel oxidation reactions (hydrogen, methane, alcohol, among others). The electrolyte, component responsible for transporting ions between the electrodes, which can transport anions (O^{2-}), from the cathode to the anode, or cations, from the anode to the cathode, in protonic cells (H^+). Finally, the cathode is the electrode that receives the air supply, responsible for the oxygen reduction reactions (ORR). **Figure 2** shows a schematic diagram of SOFC^{32–35}.

Figure 2: Schematic diagram of Solid Oxide Fuel Cells (a) represents an oxygen ion conduction electrolyte and (b) a protonic fuel cell (adapted)³⁵.



The fuel cell operation is based on electrochemical reactions. The fuel oxidation takes place at the anode and the reaction generates electrons, these are transported by the electrode to the external circuit, **Equation 2**, and schematically shown in **Figure 2(a)**. Subsequently, the electrons will be received at the cathodes and transported to the reaction sites, where they are reactants for the ORR, **Equation 3**. In this step, oxygen ions are obtained as a product. Those ions species will be transported to the anode by the electrolyte, where, finally, water will be produced as the final product of the reaction. **Equation 4** represents the global reaction of an oxygen ions transport SOFC type, operating with H_2 .



Solid oxide fuel cells can be split into two classes, which consider their operating temperature. Devices operating in the range of 700 – 1000 °C are defined as High Temperature Solid Oxide Fuel Cell (HT-SOFC). The HT-SOFCs are the oldest, with the first operational use starting around 1940^{31,36}. However, devices operating in this temperature range encounter problems such as poor

compatibility between components, and high degradation of materials during operation, which leads to a limited lifetime^{10,37–39}.

To overcome such challenges generated by the high operating temperature, it was developed systems that work in a lower temperature range, 500 – 700 °C. Those are called Intermediary Temperature Solid Oxide Fuel Cells (IT-SOFC). The operation of these devices at a lower temperature can partially solve the limitations presented above, related to the operation of HT-SOFC^{30,40}. However, the low operating temperature brings other drawbacks. As they are solid electrolytes, the ionic conductivity of these devices is directly dependent on the operating temperature. Therefore, one of the challenges to overcome related to this process is to find materials that at low temperatures present ionic conductivity comparable to HT-SOFC electrolytes^{40,41}.

In the following items, the main functions, characteristics, and properties of each of the components of the HT-SOFC and IT-SOFC will be described and discussed. Within each topic, the current development scenario and the main advances needed for SOFC will also be presented.

2.2.1 Anodes

The anode is the electrode responsible for fuel reactions. In general, it is the one who determines how efficient is the electro-oxidation reaction. Thus, it required some specific characteristics and properties. The material that constitutes the anode must possess a high catalytic activity, to carry out the oxidation reactions, noble metals and some transition metals present such property. However, when it comes to IT-SOFC, the low operating temperature further restricts the possible metals^{42–44}.

The catalytic performance is dependent on active sites distribution and a high surface area allows such disposal, coupled with an electrode with porous microstructure. In the later, the porous must remain open throughout the cell operation. Later will be discussed that the closing of these pores is the most common problem related of cells operation on carbon-based fuels⁴⁵.

Another important property required for anodes is mixed ionic–electronic conductivity (MIEC). This is important, since at the triple-phase-boundary (TPB), where the reactions occur, while electrons are conducted to the external circuit, ions must also diffuse to the electrolyte to be transported to the cathode and gas diffuses through the pores^{46–48}.

Moreover, the material must be chemically stable because it is exposed for several hours to a reducing environment and high temperature. As well as a coefficient of thermal expansion compatible with the other cell components^{40,49}.

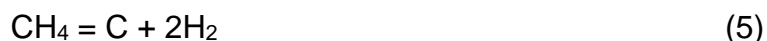
Finally, another important attribute is the low cost associated with its manufacturing since the idea is the industrial scaling of the product. Noble metals, despite their high catalytic activity, have a high cost. Therefore, the search for materials that play the role of catalyst with low aggregate cost is one of the main anode developments focuses^{26,47,48}.

Currently, the materials reported as anodes in SOFC are composites formed by ceramics and metals, cermets. Among them, one of the most prominent has Nickel (Ni) in the composition, since this metal has good electrical, catalytic, and thermal properties, and has a low cost^{31,45,50,51}.

However, some operational issues still need to be overcome for SOFCs to earn even more space in the market. These problems are closely related to degradation problems during operation which decreases its lifetime. Basically, there are two major problems reported in the literature that generate damage during operation, that are coke deposition when carbon-based fuels are applied and the material's microstructure change^{36,52}.

During the reaction with carbon-based fuels, as can be seen in **Equation 5**, coke is formed as a product. Coke is responsible for the coarsening of the anode, causing clogging of the pores and, consequently, the loss of the ceramic microstructure. Another problem related to carbon deposition is the reduction of

the TPB, which generates an increase in cell resistance. These two drawbacks led to a loss of catalytic efficiency and, therefore, a loss of cell efficiency^{38,39,53}.



2.2.2 Electrolyte

The solid electrolyte plays the role of conducting ions through the electrochemical system. This in turn can be separated into two groups, those that conduct oxygen ions (O^{2-}) and those that conduct protons (H^+). In addition to conducting ions, it plays a role in the separation between two gas interfaces. Another important responsibility of electrolytes is to block the electric current flux or flow, that is, forcing the conduction of electrons through the external circuit, avoiding a leakage current, which would decrease the efficiency of the fuel cell^{36,41,49}. Moreover, chemical stability is another determining factor for the choice of material, since the electrolyte must be dense with a low number of pores during the entire cell operation^{29,40,49}.

Rare earth metal oxides are reported as solid electrolytes for HT-SOFCs, whereas materials with fluorite crystalline structures such as stabilized zirconia are widely used in this type of cell. For instance, yttria-stabilized zirconia (YSZ) system is the best-known material. This system, in turn, conducts O^{2-} ions, with an approximate conductivity of 0.1 S cm^{-1} at 1000°C ⁵⁴. The fluorite-type structure has an arrangement that allows better diffusion of oxygen ions, since the cations occupy all tetrahedral interstices leaving a high number of free octahedral interstices, it is through these voids that oxygen ions are conducted⁵⁵.

However, the ionic conductivity in these materials is dependent on the cell operating temperature, the ionic conduction of YSZ at 700°C is less than 0.01 S cm^{-1} , ten times less conductive than at 1000°C ⁵⁶. Lately, materials such as gadolinium doped-ceria (GDC), samarium doped-ceria and strontium-doped lanthanum, gallium, and magnesium (LSGM), have emerged as a suitable alternatives to YSZ in IT-SOFC applications. Whereas, at the same operation temperature, 700°C , they possess higher conductivity compared to YSZ (LSGM at 700°C 0.08 S cm^{-1} and GDC at 700°C 0.04 S cm^{-1})^{54,57,58}.

One of the main bottlenecks related to electrolytes is phase changes during the operation, mainly in HT-SOFC. As previously mentioned, YSZ is the most common electrolyte in HT-SOFCs, and when exposed to high temperatures for a long time, it undergoes a crystalline system change, from cubic to tetragonal. The tetragonal phase, prejudices the transport of oxygen ions, bringing a loss of efficiency to the cell^{59,60}.

2.2.3 Cathodes

Cathode is the interaction interface between oxygen and electrolyte. The main electrode function is the catalysis of ORR, to conduct oxygen ions to electrolyte and receive electrons from the external circuit (in a SOFC with oxygen ions conduction electrolyte)⁵⁷.

The requirements for the material to be used as a cathode are a high surface area, high catalytic activity for ORR, porous microstructure, chemical and thermal stability, MIEC, and low cost associated with manufacturing. These material properties are similar to those of the anode, as mentioned in the previous section. Ceramic with a porous structure, high surface area, and catalytic sites is necessary. These properties will provide a suitable TPB area for ORR and transport of oxygen ions to the electrolyte by the diffusion mechanism^{61,62}.

Regarding the oxides used for HT-SOFC, manganese-based materials are the most used for cathodes. For instance, the perovskite structure $(\text{La,Sr})\text{MnO}_3$, LSM, is used because it is chemically, thermally, and morphologically stable, and is an excellent electronic conductor at temperatures above 850 °C. However, to achieve ionic conduction, it must be mixed with the electrolyte material. Nevertheless, this structure has an oxygen excess that is caused by the formation of defects, which in turn, are generated by cation vacancies. As a consequence the cell losses efficiency which is caused by the increase of polarization resistance^{63,64}.

With the development of IT-SOFC technology, new materials have been presented as promising cathodes, with great emphasis on cobalt-based composition. The perovskite $\text{La}_{1-x}\text{Sr}_x\text{Co}_{1-y}\text{Fe}_y\text{O}_3$, LSCF, has been widely studied because it presents at temperatures around 600 °C, electrical conductivity between 10^2 - 10^3 S cm^{-1} , and ionic conductivity between 10^{-3} - 10^{-1} S cm^{-1} ^{65–67}. However, the use of this material is not yet cost-effective, due to the high cost associated with cobalt and problems of phase segregation after a long time of operation^{40,68}.

One of the consequences related to the decrease in operating temperature is a loose in the catalytic activity of perovskite-type ceramics for ORR and also a decrease in ionic conduction. Another structure that stands out for application in IT-SOFC is the perovskites with the Ruddlesden-Popper (RP) phase. These are not necessarily composed of 2A elements, alkaline earth metals, which avoids the problem of segregation, and the arrangement of the structure type allows a high number of interstitial oxygens which enable rapid transport of oxygen ions across the surface, facilitating ORR^{69–71}.

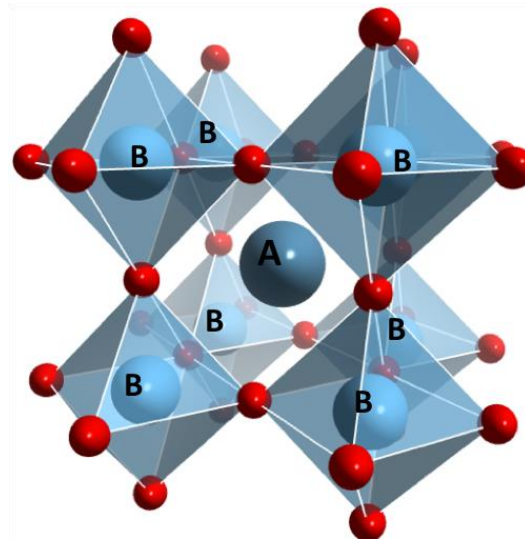
2.3 Perovskites for new energy

Perovskites refer to a class of materials with structures analogue to calcium titanate (CaTiO_3). Perovskites are ABX_3 -type structures, where the A and B sites are occupied by different cations and the X site can be occupied by oxygen or 7A elements family (halides). In the present work, the focus will be on perovskite oxides, which are structures where the X site is occupied by oxygen atoms, ABO_3 . The A and B sites can be occupied by elements of family 1A, 2A, rare earths, and transition metals. Regarding the electro-neutrality of the structure, the atoms occupying the A and B sites must have an oxidation number summed up equal to +6, since with three oxygen occupying the X site there is an oxidation number equal to -6^{14,53}.

The atom that occupies the A-site is in 12-fold coordination with oxygen anions and the cation that fills the B-site is in 6-fold coordination with oxygen anions. **Figure 3** presents the ideal structure of perovskites. The crystalline systems of

perovskites can vary according to the elements that compose them, being able to transit between tetragonal, orthorhombic, and cubic systems. One of the determining parameters for a perovskite crystalline system is the ratio of the radii of participating species, which is strictly related to the geometric restriction of the structure^{72,73}.

Figure 3: Schematic structure of cubic perovskite (ABO_3)⁷⁴.



This parameter is known as the Goldschmidt tolerance factor, which has a strong relationship with the microstrain present in the structure. The tolerance factor (t) is given by **Equation 6**, where r_a, r_b, r_o are the radii of the species that occupy the A and B sites and of oxygen, respectively.

$$t = \frac{(r_a + r_o)}{\sqrt{2} (r_b + r_o)} \quad (6)$$

The perovskite structure is only formed if $0.80 < t < 1.10$, and for an ideal cubic system, $t = 1$. When the cation occupying the A site is very small, the value of t is less than 1, which generates an octahedral distortion in the system and a decrease in the symmetry of the system. At this point, it is important to note that some properties of interest in perovskites, such as superconductivity, high mixed conductivity, and piezoelectricity, arise exactly through the mismatch of bonds between atoms^{42,63}.

It is worth noting that the tolerance factor is not the only parameter to be considered, it is vital to observe the nature of bonding between the atoms occupying the A and B sites. In order, to form the perovskite structure, the bonds need to have greater ionic than covalent character. This is owing to the form in which atoms that have a higher covalent nature coordinate with each other. Generally, this class of atoms has a coordination number lower than 6 and, therefore, does not stabilize in a perovskite structure^{75,76}.

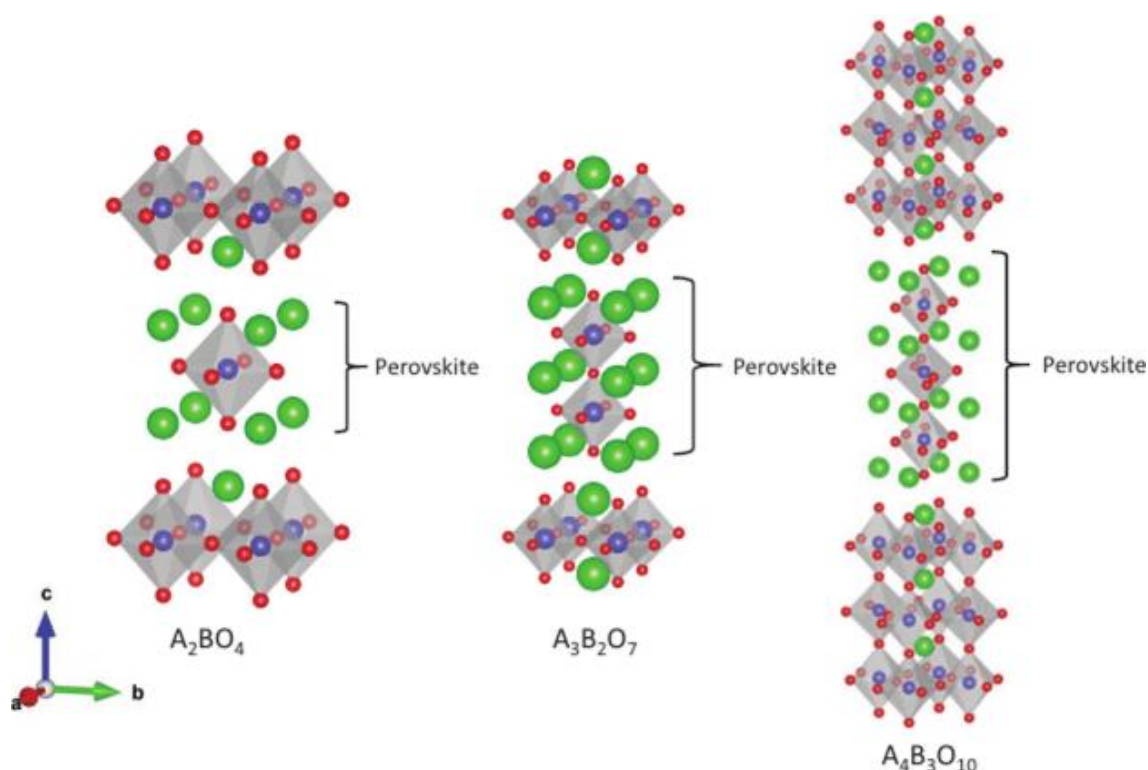
Among many systems, perovskites have attracted attention because they can incorporate a wide variety of cations in their structure, with several different oxidation states. The structural flexibility of perovskites promotes the formation of a large amount of oxygen vacancies, thereby maintaining the architecture of the structure. This capability to accommodate cations and create oxygen vacancies can further electrocatalytic processes and control the electronic conductivity, leading to different physical, chemical, and photocatalytic properties.

Regarding energy conversion technologies, perovskites are widely studied to be applied as SOFC electrodes. As discussed above in this section, owing to the electrocatalytic, electrical, and mechanical properties. Perovskite structures can be applied as all components of SOFC.

2.3.1 Ruddlesden-Popper phase

Among the possible variations in perovskites structures, one that has been extensively explored in literature, with great prominence in fuel cells application, is the Ruddlesden-Popper (RP) perovskite system. The phase takes the name from the researchers Ruddlesden and Popper, who in 1958 managed to synthesize and stabilize the phase. The basic chemical formula of the RP phase is known as $A_{n+1}B_nO_{3n+1}$. Where n is the number of perovskite octahedrons. It generally has a tetragonal crystal system, with the ABO_3 perovskites being intercalated with layers of rock salt AO along the c axis. **Figure 4** schematically presents the RP structure^{77,78}.

Figure 4: Ruddlesden-Popper phase structure¹⁴.



The RP phase is widely applied for IT-SOFC application, this is owing to the properties that the material presents in the operating temperature range of these cells. Initially, the RP phase was extensively studied for application as cathodes, since at intermediate temperatures (500 °C – 700 °C) it presents a high oxygen conduction and catalytic activity for ORR. This property can be easily explained it is the structure, which provides, through the mechanisms of interstitial oxygen diffusion, rapid conduction of oxygen ions when compared to common perovskites. Another important characteristic related to the RP structure is that these materials are not necessarily composed of 2A family elements, which reduces the possibility of phase segregation during operation^{79–81}.

Recently, the use of the same structure for application in anodes has been proposed due to the chemical stability that the structure presents in a reducing environment. Furthermore, RP phase presents a coherent coefficient of thermal expansion, providing compatibility between the elements of the cells. In addition,

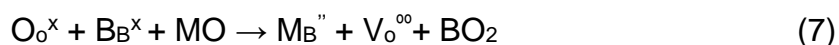
it is important to put in relevance again the high capacity of the structure to store interstitial oxygen and oxygen vacancies, mainly due to the intercalation of layers between rock salt and perovskites, which promotes a high conductivity of ions through the mechanism of diffusion through interstices or for vacancies^{68,82,83}.

Chen's group studied the properties of $\text{La}_{1.5}\text{Sr}_{0.5}\text{NiO}_{4+\delta}$ doped with copper as a cathode for electrolysis in solid oxide electrolysis cells. The research group found a high current density, improved catalytic activity with an increase in the copper content, and no degradation after the reaction. These results show that the system is promising for use in electrochemical applications^{84,85}.

2.3.2 Doping in perovskites

One strategy for changing the material properties is to add defects in a controlled manner. One method is the addition of dopants to occupy crystalline sites A or B. Depending on the radius, size, valence, or nature of the ion, it is possible to create oxygen vacancies or increase the interstitial oxygen number, which can lead to a change in electrical or ionic conductivity, for example.

The creation of oxygen vacancies and the increase in interstitial oxygen can be provided by doping elements that have nearly radii but are aliovalent, that is, cations with a different ion valence at higher concentrations. The addition of ions at the B-site with lower valence generates oxygen ion vacancies, as shown in **Equation 7**, in the Kröger-Vink notation. However, if there is an increase in impurities with a valence number greater than that of the cation that originally occupies the B site, in this case, there is an increase in the number of oxygen ions in the interstices of the structure^{86–88}.



The same doping strategy and considerations can be applied to site A. Doping with aliovalent species is expected to generate vacancies that promote a greater transport capacity in the material. This is predictable since the increase in the number of carriers can increase the ion conduction in the material^{89,90}.

2.3.3 Lanthanum titanate, nickelate and cuprate systems

Lanthanum titanate has a tolerance factor of 0.90, indicating that the A-site is small and can create distortions in a certain direction. This deformation is known as octahedral distortion, and this leads to a system symmetry decrease⁹¹.

Lanthanum titanate perovskite is a typical Mott insulator at room temperature and at high temperature behaves as metallic. In perovskites systems, the B-site element plays a fundamental role in electronic conduction and catalytic behavior, thus it is substantial that the B-site cation has the potential to adopt multiple oxidation states. In lanthanum titanate, the behavior mentioned above can be explained by the presence of Ti^{3+} . In a reduction atmosphere, as in SOFC anodes, it remains Ti^{4+}/Ti^{3+} , this forms a redox couple which allows the acceptance of electrons from hydrogen gas or hydrocarbon to promote a dissociation. Besides that, the couple redox increases the electronic conductivity by charge compensation effect. In titanates, the concentration of charge carriers has a high dependence on the concentration of Ti^{3+} . The control of Ti^{3+} can be made in several ways, one strategy is controlling the sintering or calcination atmosphere. These structures have been widely studied because of their good structural stability in reducing and oxidizing atmospheres.^{92–96}

However, lanthanum titanate-based perovskites show poor electrochemical properties which impedes a good electrocatalytic activity. Therefore, these structures need to be improved whether it is to be applied as anodes in SOFC⁹⁷.

It is possible to improve ionic conductivity by creating and controlling oxygen vacancies. With an increase in the number of vacancies, the mobility of the ions improved because there were several sites available for jumping. One way of overcoming the poor catalytic activity is by doping the B-site with transition metals. Nickel and copper are common metals used for B-site occupation in perovskites. These metals are well known as good species for their catalytic activity and are widely used as catalysts in the dry reforming of methane (DRM) and partial oxidation of methane (POM). These features allow us to study them

as anodes for direct carbon-based solid oxide fuel cells. In addition, nickel presents excellent electrical and thermal properties and, finally, Brazil holds about 16% of the world's nickel reserves, which lowers the production cost^{43,98,99}.

Another promising element to substitute the B-site is copper. Cu has been widely reported as an excellent element to improve material electrical properties. Copper-based perovskites are well known as excellent conductors with conductivity reported in 10^6 S cm^{-1} ¹⁰⁰. This can be associated with the presence of redox couple $\text{Cu}^{3+}/\text{Cu}^{2+}$, which works in the same way as $\text{Ti}^{4+}/\text{Ti}^{3+}$ couple redox^{101–103}. Another important characteristic, as well as nickel, copper presents good catalytical properties to DRM and POM reactions^{43,98}. At least, Brazil is responsible for 7% of copper production in the world, which allows a low cost associated with raw material¹⁰⁴.

In the case of Lanthanum based perovskite, another common strategy to improve electrical properties is doping the A-site with Sr that has a similar La radius ($\text{La}^{3+} = 1.06 \text{ \AA}$)^{105,106} ($\text{Sr}^{2+} = 1.12 \text{ \AA}$)^{107,108}. It has been widely reported the increase of electrical conductivity with the Sr content growth, the presence of Sr induces the oxidizing of the B-site which heightens carrier concentrations. Several research groups have been studying the strontium doping at the A-site^{109–113}, this material was reported to be a chemically stable in reducing atmosphere⁹⁷.

Several research groups have been studying lanthanum titanate-based perovskites to apply as anode of SOFC and direct methane SOFC due to their properties. Wang's group prepared a cell with $\text{La}_{0.3}\text{Sr}_{0.7}\text{TiO}_3$ as anode of direct methane fuel cell, YSZ was the electrolyte and $(\text{La}_{0.6}\text{Sr}_{0.4})_{0.95}\text{Co}_{0.2}\text{Fe}_{0.8}\text{O}_{3-\delta}$ as cathode. The cell reached 292 mW cm^{-2} at $850 \text{ }^\circ\text{C}$ feed with methane containing H_2S and CO ¹¹⁴.

2.4 Exsolution

Structured nanomaterials have been widely applied in several research areas, such as catalysts, photochemistry, disease treatments, electronic devices, drug delivery, electrochemical conversion, and energy conversion devices, among

others. The nanostructures application has earned increasing relevance in these areas due to the different properties that nanostructured materials present in concerning their bulk form^{115–119}.

Regarding catalysts, there are several ways to obtain nanostructures such as the infiltration technique, sputtering deposition, chemical vapor deposition (CVD), Pulsed Laser Deposition (PLD), impregnation, and among others. Due to its characteristic at the nanometer scale, one of the main problems related to the formation of these nanostructures is linked to the long-term stability and catalytic activity^{120–123}.

For catalysts that act in reactions containing hydrocarbons, these methods are not as efficient as one would like, because when nanostructures are exposed to high temperatures, there is a tendency for these structures to agglomerate, taking to grain growth, and carbon to deposit on the catalyst surface^{124,125}.

The grain growth of these nanostructures is a major problem for the catalytic activity. At first, this problem is related to the increase in the dimension of the structures, which first removes the material from the nanometric scale and consequently loses the properties that these materials have only in that scale. In a second moment, the agglomeration will be responsible for the decreasing of the surface area of these structures^{126,127}.

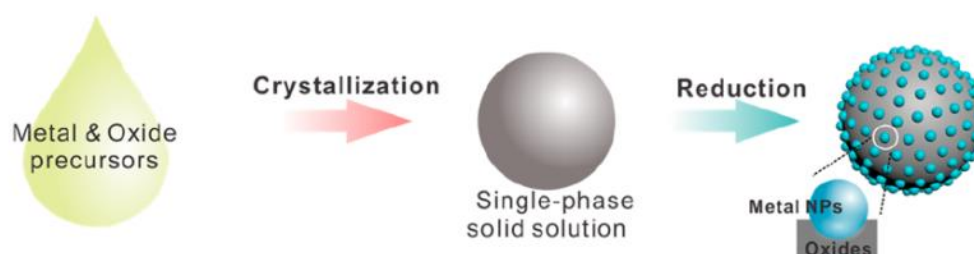
Regarding the coke formation, the deposition of carbon over the catalyst surface causes problems such as the loss of efficiency and sometimes the pores closing. This occurs due to the coarsening of the carbon layer, which leads to a decrease of active sites, therefore, the efficiency of the catalyst also decreases dramatically¹²⁴.

To overcome these problems related to the traditional methods of obtaining nanostructures, one solution that has attracted tremendous attention is the exsolution phenomenon. This process occurs in a single step to obtain anchored nanoparticles, with high catalytic activity and resistance to poisoning in a solid matrix, which has applications in several areas. When compared to the common

methods for nanoparticles obtention presented above, exsolution is less time-consuming and cheaper¹²⁸.

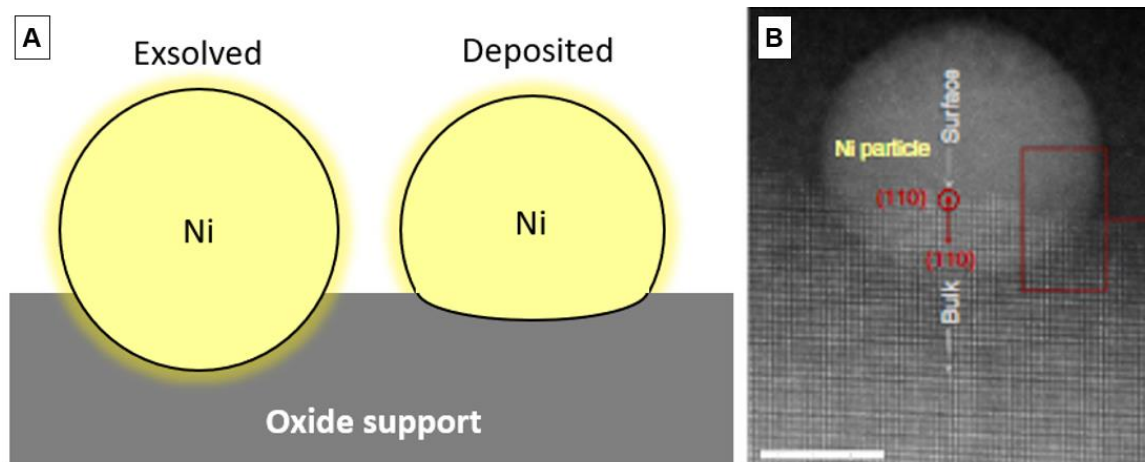
Nanoparticle exsolution is the in-situ growth of nanoparticles anchored in a solid matrix. In this approach, the metal of interest is solubilized in a solid matrix (the most common is perovskite ceramic) to form a solid solution. Thereafter, this solid solution is placed in a reducing environment and at a controlled temperature, so that the metal that is dissolved in the solid solution emerges to the surface and reduces. Basically, the exsolution is a decomposing process of one phase in a controlled way^{47,129}. **Figure 5** schematically shows the exsolution process.

Figure 5: Schematic diagram of exsolution process⁴⁷



The huge difference between exsolution and the traditional deposition methods is that the nanoparticles are embedded in the solid matrix, these nanoparticles are anchored in the matrix (**Figure 6A**). This socketing is the result of an alignment of the crystallographic plane of the solid matrix with the generated nanoparticle (**Figure 6B**). This unique way of obtaining nanostructures promotes different properties when compared to common methods^{130–132}.

Figure 6: (a) schematic diagram showing the difference between the anchored and deposited nanoparticle¹²⁸ (b) transmission microscopy image showing the alignment between the crystallographic planes of the host solid oxide and the nanoparticles¹³⁰



The first major difference is that nanoparticles generated by this method can be regenerated, in the presence of temperature and an oxidizing atmosphere, the metal present is redissolved in the solid matrix. This regeneration property increases the structure lifetime and avoids agglomeration problems associated with other methods^{133,134}.

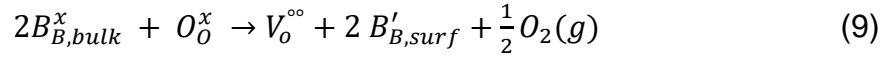
Another extremely important point regarding the alignment of the crystallographic plane of these structures is the poisoning tolerance to the catalyst in the presence of sulfur-containing gases and the protection from carbon deposition during the catalysis of the hydrocarbon dehydrogenation reaction^{130,135–137}.

In the presence of a reducing atmosphere and high temperature, the desorption of the oxygen present in the solid matrix occurs. This oxygen taken from the crystal lattice leaves an oxygen vacancy in the lattice and electrons (**Equation 8**).



Through the mechanism of vacancy diffusion, the metallic species and the oxygen ions present in the solid matrix exchange positions, with the vacancies left by the oxygen ion diffusing to the surface. Due to the higher concentration of

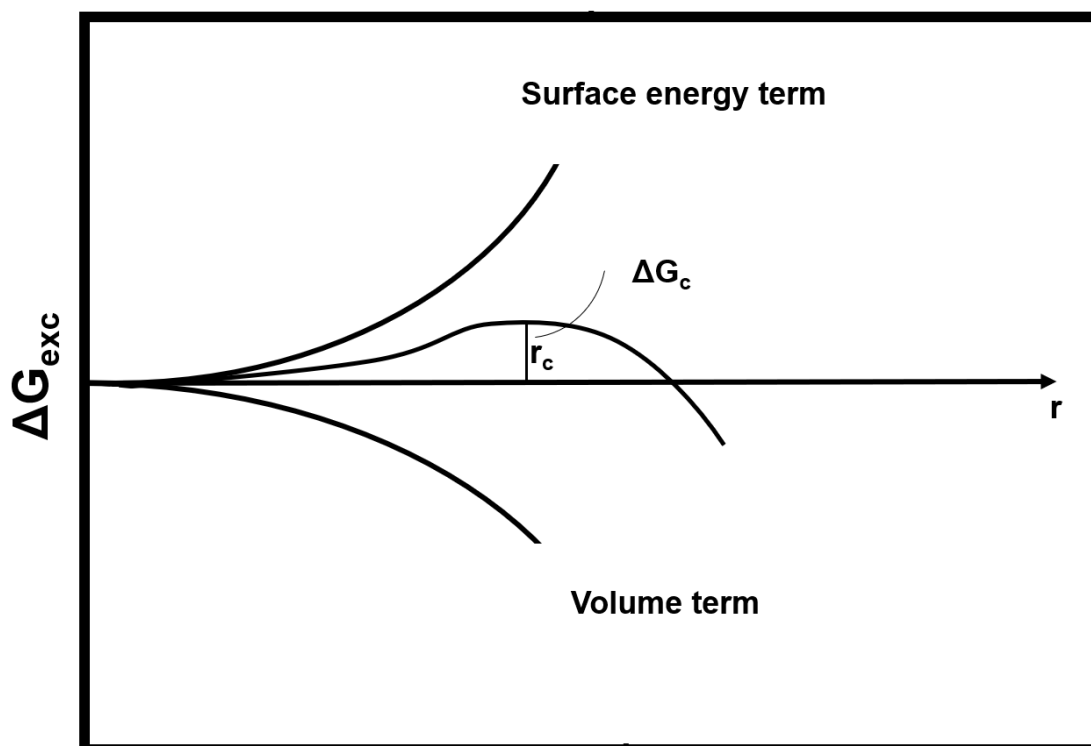
crystallographic defects, the surface is the place where the nucleation of nanoparticles is favoured, this nucleation in turn is continuously fed by the diffusion mechanism of metal ions present in the bulk of this solid matrix (**Equation 9**)^{138–141}.



One of the ways to understand the nucleation process caused by the phenomenon of exsolution is through the classical model of nucleation. This model is based on the change in Gibbs free energy at the expense of two factors, the first is the change in volume free energy before and after the nanostructures' exsolution phenomena. The second is related to the surface and interface energy due to the formation of a new phase. The nanostructure critical radius (r_c) will only have thermodynamic stability when the critical free energy barrier is overcome (ΔG_c). However, during the exsolution process, there is a change in free energy caused by the transformation coming from the emergence of the newly reformed nucleus in the solid matrix (ΔG_v). Finally, γ represents the interface free energy per area unit. Mathematically, the energy required for the critical free energy to form the nanoparticle is described in **Equation 10** and graphically in **Figure 7**¹⁴¹.

$$\Delta G_c^* = \frac{4}{3}\pi\gamma^2(r_c)^2 = \frac{16\pi\gamma^3}{3\Delta G_v^2} \quad (10)$$

Figure 7: Gibbs free energy relative to particle radius during the process of nucleation and growth¹⁴¹.



The exsolution is a function of three factors, diffusion of the interest metallic ions through the solid matrix, crystalline structure strains involved in the nucleation process and growth of nanoparticles, and the local availability of the interest ions^{128,137}.

Due to the factors presented above, not all crystalline structures could serve as a host solid oxide for exsolution. This is expected since these phases sometimes do not have physicochemical characteristics to play such a role. As previously mentioned, perovskites are structures known to have a great capacity to transport cations, oxygen ions, and electrons through their crystal lattice. In addition, this crystalline system can accommodate different types of metals in the B site. Other crystalline structures such as fluorites, wurtzites, spinels, halites, and rutile, among others, do not have these same characteristics as perovskites^{128,142,143}.

Another advantage of perovskites is their ability to create defects to improve the diffusion of ions through the crystal lattice. There are several methods to improve the interest ions diffusion in the host solid oxide such as deficient A-sites and

doping with aliovalent ions of different ionic radii to create oxygen vacancies through which the ions will be transported. One of the examples of this defect engineering is the partial replacement of La^{3+} ions by Sr^{2+} ions at the perovskites A-site. This substitution of ions with different valences promotes the creation of oxygen vacancy which, as discussed, increases the transport capacity of ions that occupy the B-site and therefore facilitates the transport of cations of interest^{52,144}.

It is worth noting that when dealing with perovskites, the cations that can exsolve usually occupy the B-site of the structure, this is directly linked to the Gibbs free energy related to the reduction phenomenon. The ions that occupy the A-site demand high energy for the transformation, which makes them inactive for redox reactions¹²⁸.

There are several factors to control the size and shape of the exsolved nanoparticle, such as temperatures, time, and reducing gas, among others. The literature has shown that, depending on the metal of interest, high temperatures and long exposure times can promote an increase in the average size of the generated nanoparticles^{135,145}.

Finally, exsolved nanoparticles have found applications in various research fields, including energy conversion, energy storage, sensors, catalysis, and others. In the context of energy conversion, metallic nanoparticle exsolution has been extensively employed to enhance the performance of Solid Oxide Fuel Cells (SOFCs), particularly at the anodes^{146,147}. As discussed earlier, exsolved nanoparticles are strongly anchored to the host oxide solid, leading to a robust interaction between the nanoparticles and the matrix. Recent papers argue that this interaction results in tailored properties, such as sulfur-poisoning resistance, and helps to prevent coke deposition when operating with carbon-based fuels^{109,148–150}.

3. Objectives

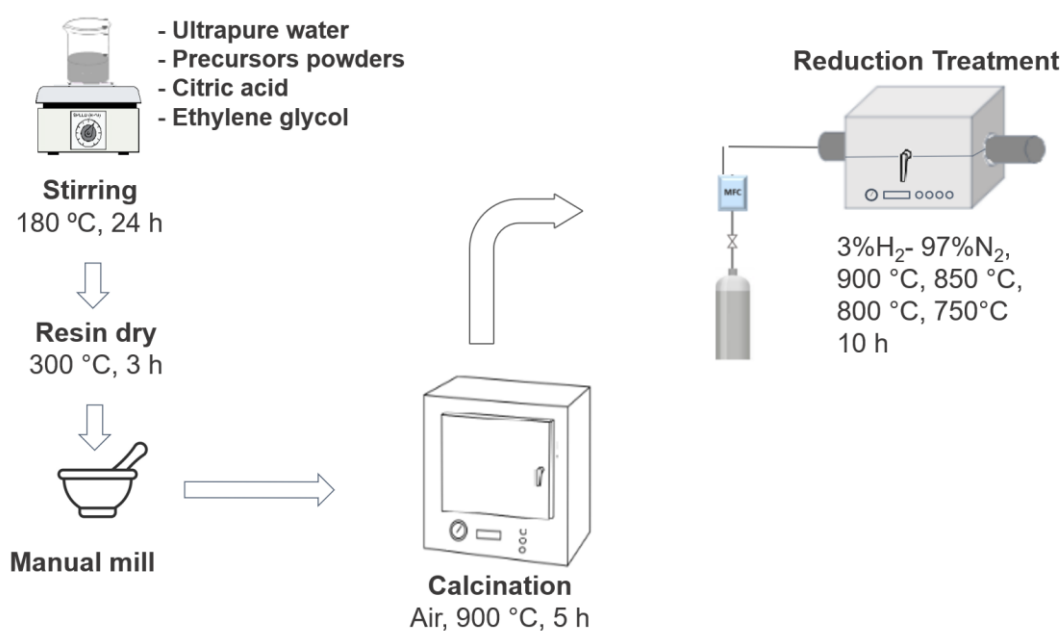
The main objectives of the present work are:

- Synthesis of $\text{La}_{0.8}\text{Sr}_{0.2}\text{Ti}_{0.7}\text{Cu}_{0.3-x}\text{Ni}_x\text{O}_{3-\delta}$ ($x = 0.1; 0.15; 0.2$) and $\text{La}_{1.2}\text{Sr}_{0.7}\text{Cu}_{0.5}\text{Ni}_{0.5}\text{O}_{4\pm\delta}$ using the Pechini Method.
- Promote copper and nickel exsolution as an alloy.
- Investigate titanate crystal structure before and after the exsolution process.
- Comprehend how temperature and strain modify the exsolution phenomena in titanates.
- Explore titanates electrical properties in reducing and oxidizing atmosphere.

4. Materials and Methods

4.1 Synthesis and methods

The samples with compositions $\text{La}_{0.8}\text{Sr}_{0.2}\text{Ti}_{0.7}\text{Ni}_{0.3-x}\text{Cu}_x\text{O}_{3-\delta}$ ($x=0.1, 0.15, 0.2$) and $\text{La}_{1.2}\text{Sr}_{0.7}\text{Ni}_{0.5}\text{Cu}_{0.5}\text{O}_{4\pm\delta}$ were synthesized in batches with 5 g each via a Chemical route based on modified Pechini method. The starting chemicals reagents were grade >99.5% by Sigma-Aldrich: $\text{La}(\text{NO}_3)_3 \cdot 6\text{H}_2\text{O}$, $\text{Sr}(\text{NO}_3)_2$, $\text{Cu}(\text{NO}_3)_2 \cdot 3\text{H}_2\text{O}$, Titanium isopropoxide, nickel acetate, citric acid (CA) and ethylene glycol (EG). Titanium isopropoxide was diluted in EG and CA to avoid precipitation. The other precursors were dissolved in ultrapure water (Milli-Q Type 1) with CA under constant stirring at 80 °C for 2 h. After EG with CA and Titanium isopropoxide was added to the solution with other precursors, the temperature was raised to 180 °C to promote polymerization. After 24 h it was formed a brick orange resin, which was milled to a fine powder. The powder samples were calcined at 900 °C in air for 5 h (controlled temperature ramp 5 °C min⁻¹). To perform exsolution of nickel-copper alloy, the calcined powder was subsequently treated in a tubular furnace with a reduction atmosphere, hydrogen (3% H₂/N₂), at 900 °C, 850 °C, 800 °C, 750 °C for 10 h (controlled temperature ramp 5 °C min⁻¹). **Figure 8** shows all stages of synthesis and **Table 1** presents all prepared samples and the respective treatments.

Figure 8: Stages of synthesis**Table 1:** Samples and treatments

Sample	Calcination	Reduction Treatment	Abbreviation
La _{0.8} Sr _{0.2} Ti _{0.7} Ni _{0.1} Cu _{0.2} O _{3-δ}	Air, 900 °C, 5 h	3%H ₂ - 97%N ₂ , 900 °C, 850 °C, 800 °C, 750 °C 10 h	N ₁₀ C ₂₀
La _{0.8} Sr _{0.2} Ti _{0.7} Ni _{0.15} Cu _{0.15} O _{3-δ}			N ₁₅ C ₁₅
La _{0.8} Sr _{0.2} Ti _{0.7} Ni _{0.2} Cu _{0.1} O _{3-δ}			N ₂₀ C ₁₀
La _{1.2} Sr _{0.7} Ni _{0.5} Cu _{0.5} O _{4±δ}			RP

4.2 Characterization

4.2.1 Thermogravimetric analysis (TGA)

The thermogravimetric analysis/differential thermal analysis (TGA/DTA) was performed using a LABSYS EVO STA, from Setaram, with the accuracy of this equipment it is possible to observe the mass change and sample chemical or physical variation as a function of temperature. The samples used were the dried gels obtained by the Pechini method synthesis. All analysis was done in Ar atmosphere, from room temperature to 1500 °C at a heating and cooling rate of 10 °C min⁻¹.

4.2.2 X-ray diffraction (XRD)

To perform the XRD analyses it was used an X-ray diffractometer D8 focus model, manufactured by Bruker. The configuration used was $\theta/2\theta$ with Bragg-

Brentano geometry and use $\text{CuK}\alpha$ radiation with a silicon strip linear LynxEye 1D detector accoupled. The system includes a primary Soller slit and a secondary 2.5° of divergence and anti-spreading. All data were acquired with maximum voltage and current, 40 kV and 40 mA, in $20^\circ - 80^\circ$ (2θ) angular range with step of $0.02^\circ/\text{sec}$. Another diffractometer was employed, the STADI-P diffractometer, manufactured by STOE. This equipment operates in transmission model with monochromatic radiation of copper. The data were acquired between $15^\circ - 110^\circ$ (2θ) angular range.

The Rietveld method was applied to refine and extract information from XRD data. Two databases were used for the diffraction patterns: ICSD – Inorganic Crystal Structure Database and COD – Crystallography Open Database. For refinement, three XRD patterns were used, with the respective collection codes: 4124868 – LaTiO_3 , space group 221 (Pm-3m), 253255 – $\text{La}_{1.85}\text{Sr}_{0.15}\text{Cu}_{0.8}\text{Ni}_{0.2}\text{O}_4$, space group 139 (I4/mmm), and 152432 – NiCu , space group 225, (Fm-3m). The mathematical method was performed using TOPAS Academic 7 software. Instrumental peak broadening was addressed by carrying out a fundamental parameter (FP) function refinement using data from a strain-free Al_2O_3 standard sample of micrometer size. The size and peak shape information obtained from the standard sample through a modified pseudo-Voigt function (TCHZ) was utilized in conjunction with the TOPAS macros *LVol_FWHM_CS_L* (for size) and *e0_from_Strain* (for strain) to make corrections. Aiming to obtain structural information background, lattice parameter, atom occupancy, and fraction composition were refined.

4.2.3 X-ray photoelectron spectroscopy (XPS)

X-ray Photoelectron Spectroscopy is a technique used to analyze chemically the material surface (1-10 nm). The measurements were performed at the Brazilian National Nanotechnology Laboratory (LNNano) that is part of the Brazilian Center for Research in Energy and Materials (CNPEM). Survey and high-resolution spectra were obtained using a Thermo Fisher Scientific X-ray excited photoelectron spectrometer (XPS), K-Alpha model. The equipment is equipped with an $\text{Al K}\alpha$ (10 kV, 20 mA, and power 1,486.6 eV) X-ray source with a

monochromator coupled to a variable spot size. In addition, the machine contains an Argonium ion gun to eliminate contamination.

The curve adjustments were made using the Thermo Fisher Advantage data system software, taking the Smart^{151,152} function as a baseline and the spectra was calibrated based on the C 1s line with energy at 284.6 eV¹⁵³. The peaks were identified using the NIST XPS database, and quantification was performed using the relative area method with the peaks of interest (Cu 2p and Ni 3p).

4.2.4 Scanning electron microscope (SEM)

Scanning electron images were obtained through a SEM manufactured by JEOL, FEG-SEM JMS-6701F. The machine is equipped with a Field Emission Gun which allows a high resolution due to a lower energy dispersion, this source provides a high magnification when compared with regular sources. All samples were analyzed with 3 kV acceleration voltage and with a magnification of 50000, 70000, and 100000 times. The images were obtained through Secondary Electron Imagin (SEI) detector. The powder samples were dispersed in isopropanol by sonication. Thereafter, the samples were dripped in doped silicon substrate.

4.2.5 Transmission electron microscopy (TEM)

Transmission electron microscopy was employed aiming to investigate exsolved nanoparticles and attachment on perovskite host solid oxide. The analysis was performed after proposal submission to LNNano. Images were obtained through a JEOL JEM-2100 F, manufactured by JEOL. The machine possesses a Field Emission Gun (FEG) and operates at 200 kV acceleration voltage in Transmission Electron Microscopy (TEM) in high contrast and Scanning Transmission Electron Microscopy (STEM) with 0.19 nm of spatial resolution. All data collected were treated using the software ImageJ and digital micrograph. The powder samples were dispersed in ultrapure water using an ultrasound. Thereafter were dripped onto a carbon film supported on a gold grid.

4.2.6 Dilatometry analysis

The dilatometry experiments were applied to investigate the densification conditions. The measurements were performed using a DIL 402 PC (Netzsch). The samples previously prepared were pressed into cylindrical bodies of 5 mm diameter and about 5.8 mm in thickness under a uniaxial press with a pressure of 1 ton cm^{-1} . The analysis of the green body was done in N_2 atmosphere, whereas the sample was heated from room temperature to 1500 °C at a rate of 10 °C min^{-1} .

4.2.7 Electrochemical impedance spectroscopy (EIS)

Electrochemical impedance spectroscopy is a technique used to analyze the carriers transport properties of the samples, including capacitance and resistance. The tests were conducted at the Laboratory for Materials and Energy (LaME_n). The impedance spectra were obtained using a Solatron (1287 and 1260) controlled by a microcomputer. The measurements were performed over a frequency range from 0.1 Hz to 13 MHz, with an amplitude of 100 mV.

For the measurements in high-temperature it was used platinum electrodes, and all samples were painted with platinum ink, subsequently heat treated at 800 °C, with a controlled temperature ramp of 1 °C min^{-1} (both for heating and cooling) to cure the platinum paste. These measurements were carried out in a high-temperature range of 450 °C to 650 °C, in an air atmosphere.

To investigate the electrical behavior at low temperatures, the samples were painted with silver ink and heat treated at 600 °C, with a controlled temperature ramp of 1 °C min^{-1} . The measurements were conducted between 200 °C and 450 °C.

5. Results and discussions

5.1 Structure and morphology

In this chapter, it is presented all the results obtained concerning the crystal structure and sample morphology. The first section discusses the carefully chosen calcination process, which was determined using TGA/DTA. Subsequently, we analyze the crystal structure of all samples through XRD analyses before and after the reduction treatment. For a comprehensive understanding of the lattice parameter changes and quantification of the exsolved phase, we employ Rietveld refinement.

Identifying exsolution proves to be a challenging task, as in some cases, XRD analysis fails to confirm the presence of exsolved metallic nanoparticles. Therefore, to corroborate the existence of the metallic phase, we employ complementary techniques. Specifically, XPS analysis provides a detailed discussion of the sample chemical surface properties and the structural changes obtained after reduction treatment.

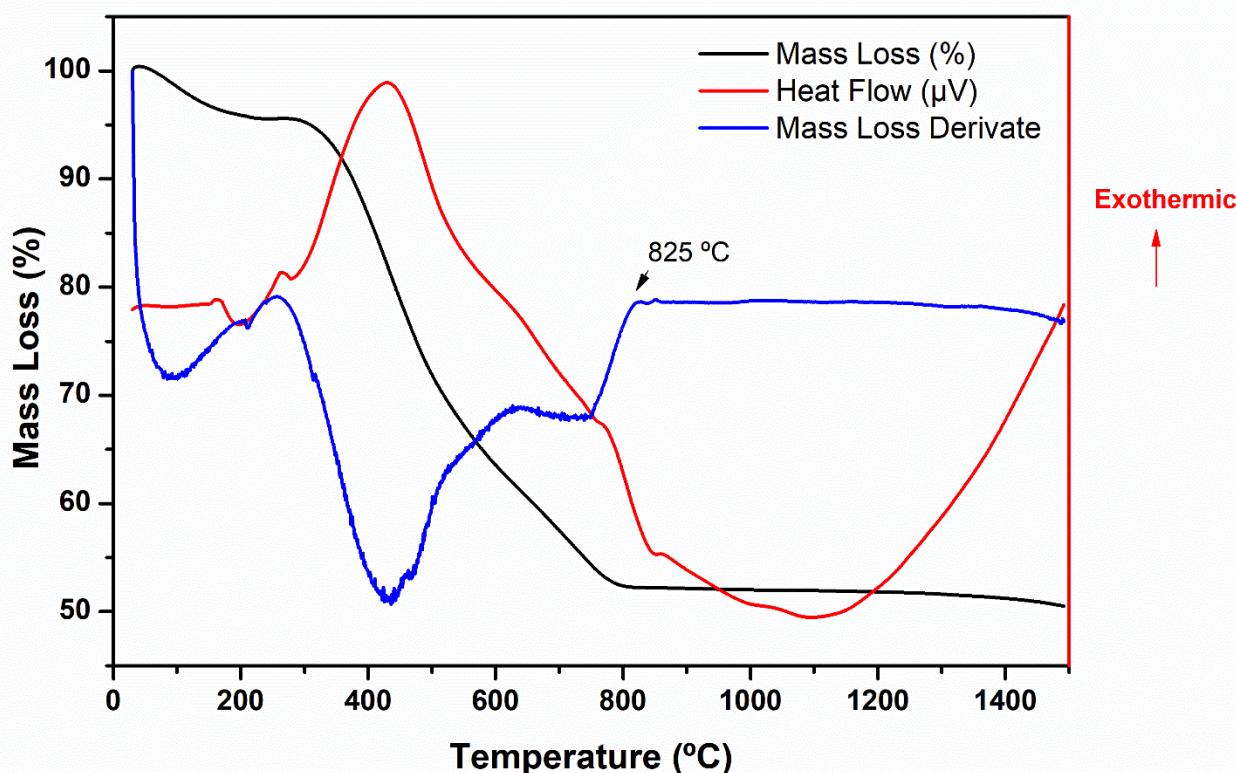
The presence of nanoparticles anchored on the host solid oxide surface was investigated through SEM images analysis. Additionally, TEM images were crucial in providing insights into the nanoparticle's composition.

Lastly, we employ dilatometry to characterize the samples, obtaining valuable information about the sintering temperature, to further investigate their electrical behavior using electrochemical impedance spectroscopy. This comprehensive approach allows for a thorough examination and understanding of the experimental results.

5.1.1 Thermogravimetry analysis

Thermal analysis of $N_{15}C_{15}$ dried gel is shown in **Figure 9**. All the samples showed similar TG/DTA profiles due to the employed synthesis method and structural semblance. The weight loss between room temperature and 250°C can be attributed to the elimination of absorbed and structural water from the sample. The second stage occurred between 250°C and 500°C, owing to the elimination of the citrate and nitrate phases present in the dried gel. This weight loss is correlated with a sharp endothermic peak in the DTA curve, resulting from the decomposition of the dried gel. In the third stage, 450°C to 625°C, another weight loss occurred, which was associated with the elimination of organics and carbon dioxide from the metal oxides. Finally, the last step is associated with oxygen loss and the formation of the perovskite structure, where it is expected the titanium coordinated by six oxygen atoms at the B-site of the perovskite structure. Hence, with the accuracy of the TG/DTA data, it was possible to conclude that the Lanthanum Titanate samples could be calcined at 900°C to obtain the perovskite phases.

Figure 9: TG/DTA data of $La_{0.8}Sr_{0.2}Ti_{0.7}Ni_{0.15}Cu_{0.15}O_{3-\delta}$ synthesized by Pechini method.



5.1.2 X-ray diffraction

5.1.2.1 Calcined samples

XRD analysis is crucial for better comprehension of crystalline structure as prepared and after the exsolution process. All findings outlined in this section were obtained using the powder samples. After the resin was calcined, all samples underwent XRD characterization. **Figure 10** shows the titanate series XRD patterns calcined at 900 °C in static air for 5 h. Characteristic peaks of cubic perovskite are observed at $2\theta = 23^\circ$, 32° , 45° , and 58° (COD n°:4124868) with the respective reflections shown in **Figure 10**. These data indicate that all calcined titanate powders have a primitive cubic perovskite system with the space group Pm-3m. No secondary phases were detected in the XRD results. Therefore, the experimental data suggest that Cu and Ni substituted Ti at B-site without segregation of CuO and NiO. Moreover, it can be concluded that Sr substituted La at A-site without La_2O_3 or SrO segregations.

Figure 10: XRD pattern after calcination at 900 °C for 5 h. The diffraction position corresponding to the centered cubic LaTiO_3 structure is highlighted with an orange circle.

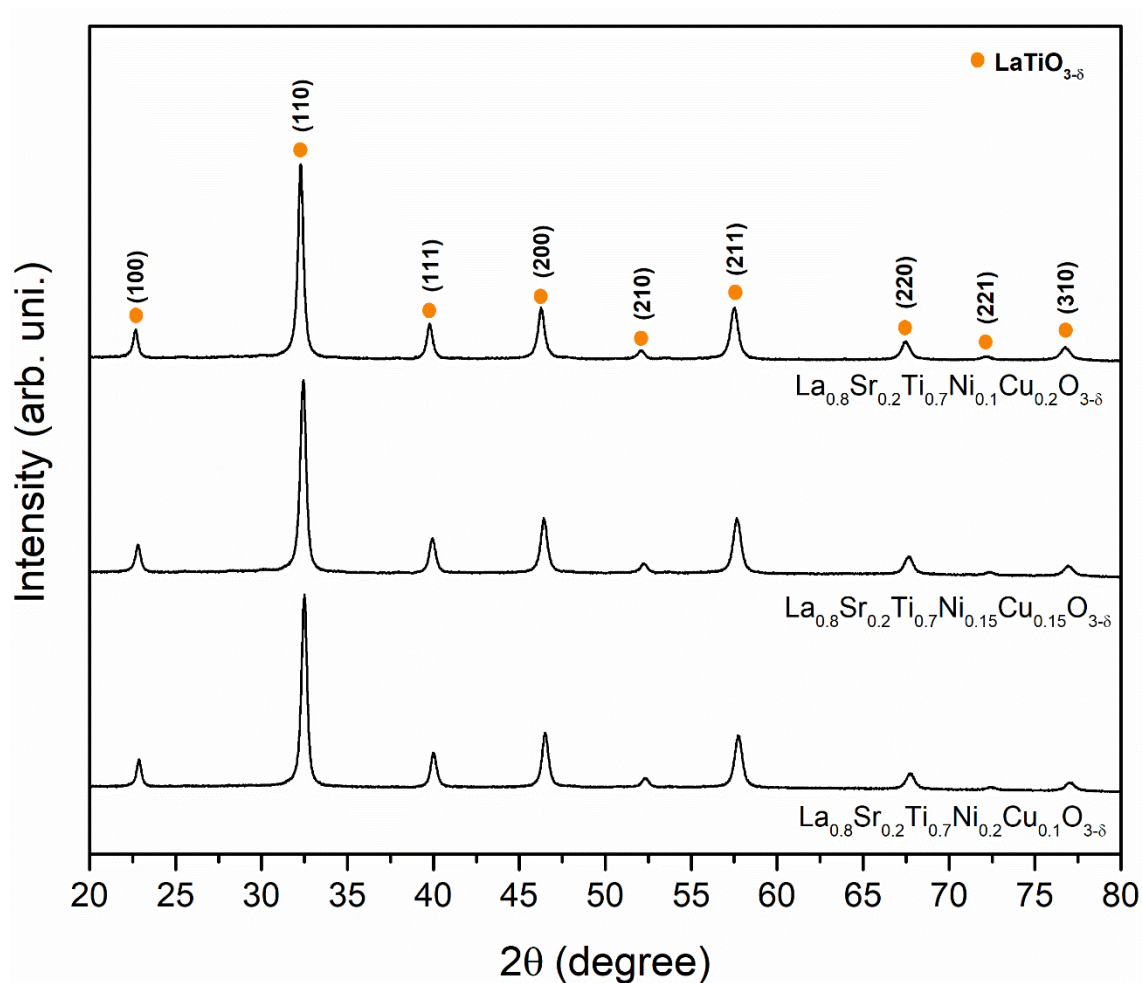
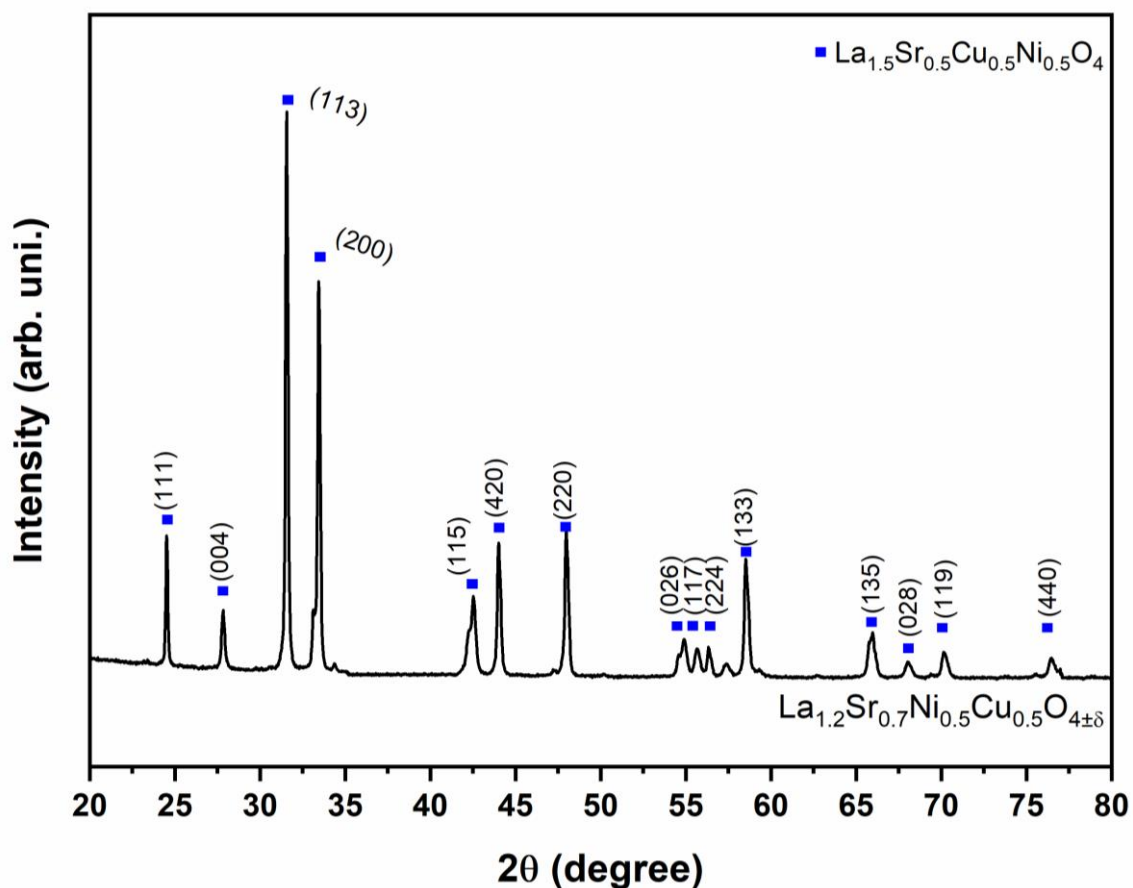


Figure 11 shows $\text{La}_{1.2}\text{Sr}_{0.7}\text{Ni}_{0.5}\text{Cu}_{0.5}\text{O}_{4+x}$ XRD pattern, the phase crystallized in a tetragonal system (ICSD n^o:253255) with space group $I4/mmm$. Within the accuracy of XRD, the experimental data indicates that the Cu substituted Ni without segregation of CuO and NiO. Moreover, it can be concluded that Sr substituted La without causing any segregation.

Figure 11: Ruddlesden-Popper phase XRD pattern after calcination at 900 °C for 5 h. The diffraction position corresponding to the tetragonal $\text{La}_{1.5}\text{Sr}_{0.5}\text{Ni}_{0.5}\text{Cu}_{0.5}\text{O}_4$ structure is highlighted with a blue square.



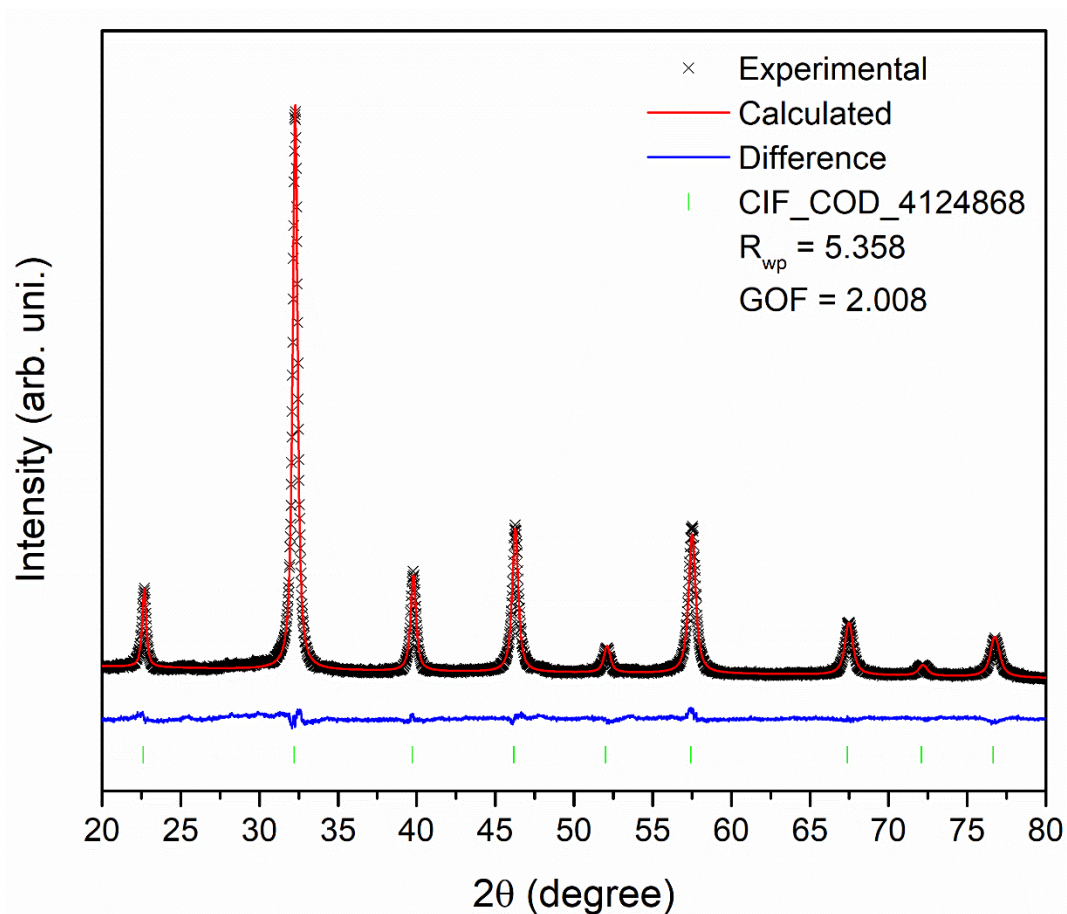
Rietveld refinement was performed, and **Table 2** summarized the main crystal structure information. **Figure 12** shows an example of the Rietveld refinement of $\text{La}_{0.8}\text{Sr}_{0.2}\text{Ti}_{0.7}\text{Ni}_{0.1}\text{Cu}_{0.2}\text{O}_{3-\delta}$.

Table 2: Data obtained through Rietveld refinement after powder calcined at 900 °C.

	Samples	A (Å)	C (Å)	Crystallite Size (nm)	Strain (10^{-6})	R_{wp}	Gof	R_{braag}
Calcined	N ₁₀ C ₂₀	3.929(4)	-	70(2)	100(6)	5.358	2.008	1.35
	N ₁₅ C ₁₅	3.928(1)	-	62(1)	90(4)	5.966	2.198	2.548
	N ₂₀ C ₁₀	3.927(1)	-	25(2)	60(2)	5.688	2.036	2.203
	RP	3.795(5)	12.848(2)	153(2)	367(3)	6.926	3.428	2.912

Figure 12: Rietveld pattern refinement of $\text{La}_{0.8}\text{Sr}_{0.2}\text{Ti}_{0.7}\text{Ni}_{0.1}\text{Cu}_{0.2}\text{O}_{3-\delta}$ as the cubic phase (Pm-3m). The observed XRD pattern is shown with black cruise points, the red line represents the

theoretical model while the blue line shows the difference between the theoretical model and the experimental data. Finally, the expected peaks positions are shown above in green bars.



In **Table 2**, it is worth noting the increase in lattice parameter with the rise of copper content. This was expected since the Ni ionic radius is smaller than Cu ($\text{Cu}^{2+} = 0.73 \text{ \AA}$ and $\text{Ni}^{2+} = 0.69 \text{ \AA}$). Another crucial parameter obtained through Rietveld refinement was strain. As explained in the literature review chapter, the exsolution process is dependent on crystal strain. An increase in crystal strain facilitates the exsolution process due to the structure's tendency to eliminate crystal defects. An increase in crystal strain was anticipated with the increment of copper content, as previously shown, copper possesses a larger ionic radius than nickel, and B-site doping with a larger radii atom creates strain in the crystal structure. According to the data is possible to conclude that $\text{La}_{0.8}\text{Sr}_{0.2}\text{Ti}_{0.7}\text{Ni}_{0.1}\text{Cu}_{0.2}\text{O}_{3-\delta}$ composition is the most promising for producing a NiCu nanoparticle alloy after reduction treatment.

5.1.2.2 Reduced samples

After calcining all powder samples at 900°C for 5 hours, all compositions were subsequently reduced at four different temperatures (900°C, 850°C, 800°C, 750°C) for 10 hours. In this section, the XRD patterns and Rietveld refinement of all samples will be thoroughly discussed and compared. To clarify the exsolution process, **Equation 11** presents a general chemical equation of the exsolution phenomena, and **Equation 12** specifically represents the statement for this system.

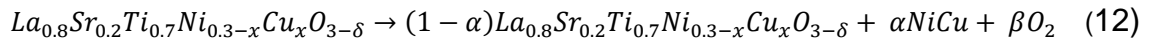
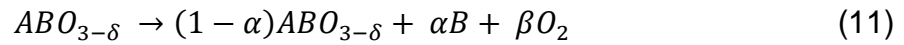


Figure 13 shows the XRD pattern of all titanate samples reduced at 900°C. It is possible to observe new peaks emerging around 44° and 52° in 2 theta, and these peaks correspond well with a nickel-copper alloy face-centered cubic structure (ICSD n° 103063). The same behavior was observed in all samples reduced at lower temperatures. **Figure 14**, **Figure 15**, and **Figure 16** display the XRD patterns after reduction treatment at 850°C, 800°C, and 750°C for 10 hours, respectively.

Figure 13: XRD pattern after reduction treatment at 900 °C for 10 h. The diffraction position corresponding to the centered cubic LaTiO₃ structure is highlighted with an orange circle, while the green circle indicates the diffraction position associated with the centered cubic Nickel-Copper alloy.

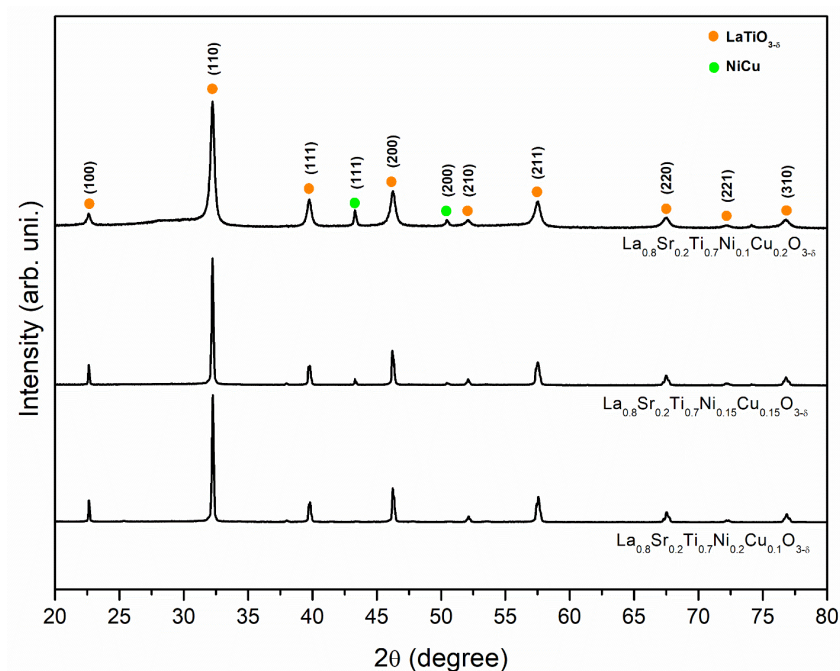


Figure 14: XRD pattern after reduction treatment at 850 °C for 10 h. The diffraction position corresponding to the centered cubic LaTiO_3 structure is highlighted with an orange circle, while the green circle indicates the diffraction position associated with the centered cubic Nickel-Copper alloy.

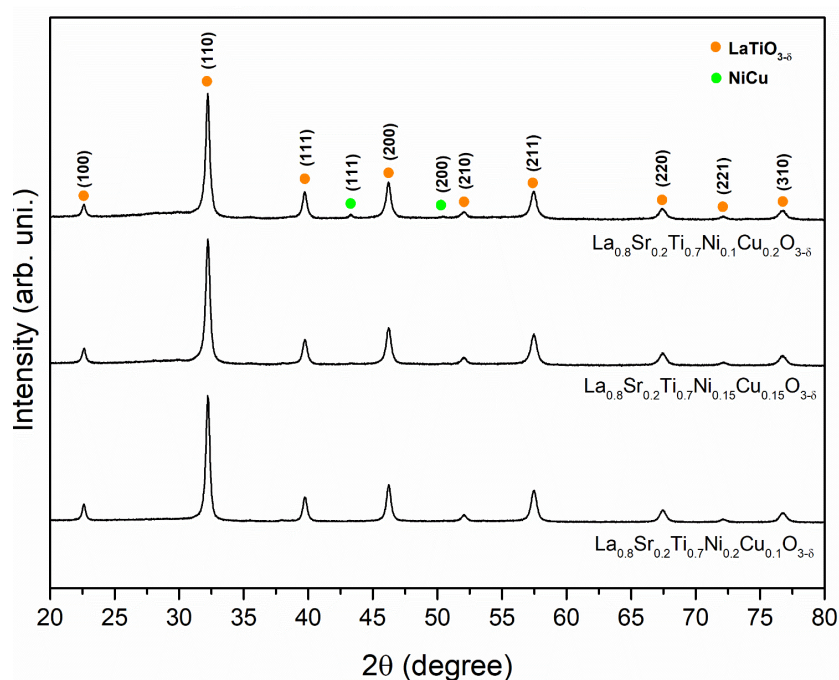


Figure 15: XRD pattern after reduction treatment at 800 °C for 10 h. The diffraction position corresponding to the centered cubic LaTiO_3 structure is highlighted with an orange circle, while the green circle indicates the diffraction position associated with the centered cubic Nickel-Copper alloy.

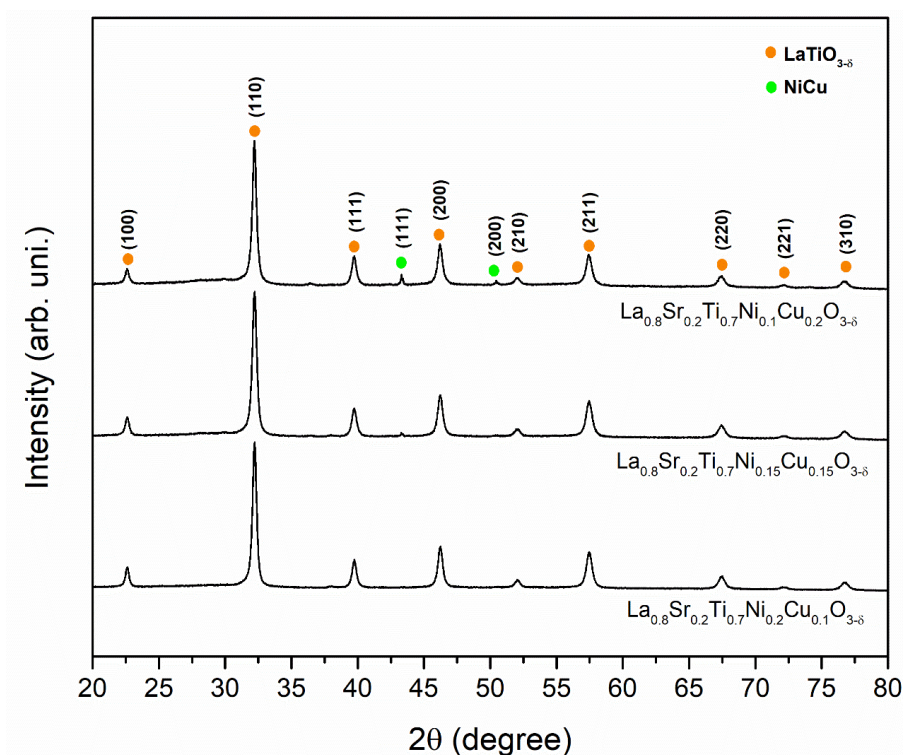
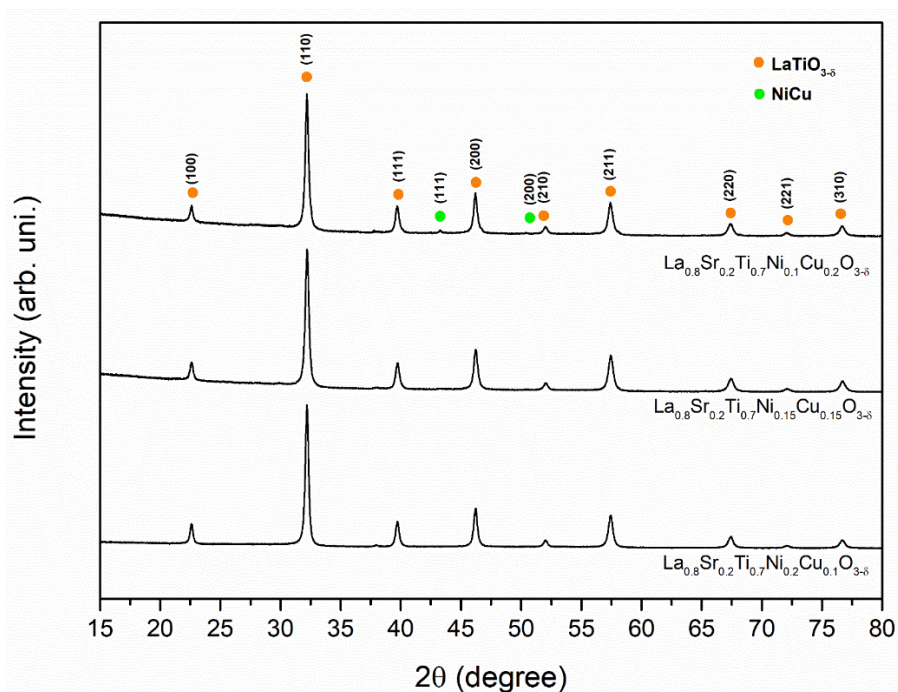


Figure 16: XRD pattern after reduction treatment at 750 °C for 10 h. The diffraction position corresponding to the centered cubic LaTiO_3 structure is highlighted with an orange circle, while the green circle indicates the diffraction position associated with the centered cubic Nickel-Copper alloy.



The Rietveld refinement was performed to verify the changes in the crystal structure, and **Table 3** summarizes the main results after the reduction treatment. Larger fractions of the metallic phase were observed at higher reducing

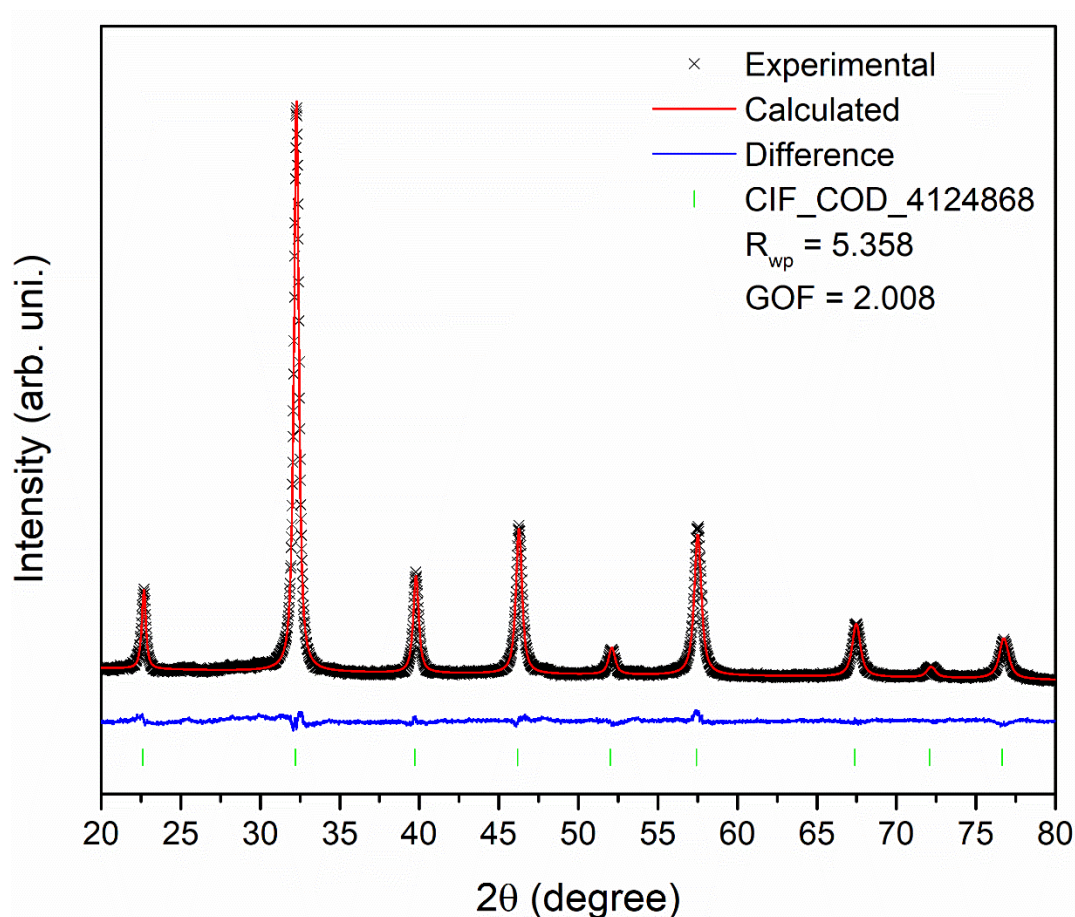
temperatures. These results lead to the conclusion that a rise in temperature favors the exsolution process. As previously discussed, strain plays a key role in exsolution phenomena. Hence, it was expected that compositions with higher strain values exsolve more easily than samples with lower strain. It is worth noting that copper content also plays another crucial role in the exsolution process. The Gibbs free energy in a reducing atmosphere of copper at 1000 K is around -150 kJ mol^{-1} , while for nickel, this value is around -50 kJ mol^{-1} . Thus, it is possible to conclude that copper facilitates the exsolution process from a thermodynamics viewpoint.

Finally, the refinement revealed that after the reduction treatment, all compositions experienced a crystal lattice parameter contraction. This phenomenon is due to the oxygen released during exsolution, which has been previously discussed by numerous research groups.^{7,130,154,155} **Figure 17** shows an example of the Rietveld refinement of $\text{La}_{0.8}\text{Sr}_{0.2}\text{Ti}_{0.7}\text{Ni}_{0.15}\text{Cu}_{0.15}\text{O}_{3-\delta}$ reduced at 800 °C.

Table 3: Data obtained through Rietveld refinement after reduction treatment of all compositions at 900 °C, 850 °C, 800 °C, and 750 °C.

	Samples	a(Å)	Crystallite Size (nm)	Strain (10^{-6})	LaTiO ₃ (%)	NiCu (%)	R _{wp}	Gof	R _{braag}
900 °C	N ₁₀ C ₂₀	3.925(1)	34(2)	87(4)	92.05	6.95	5.621	2.162	2.824
	N ₁₅ C ₁₅	3.923(1)	59(4)	7(1)	96.26	3.74	7.487	3.092	1.462
	N ₂₀ C ₁₀	3.921(1)	60(4)	7(1)	99.63	0.37	8.88	3.567	2.251
850 °C	N ₁₀ C ₂₀	3.927(1)	34(1)	100(5)	97.43	2.57	4.315	1.557	0.664
	N ₁₅ C ₁₅	3.926(1)	27(1)	86(2)	99.5	0.5	3.77	1.413	0.602
	N ₂₀ C ₁₀	3.925(1)	33(1)	80(3)	100	-	3.921	1.5	1.001
800 °C	N ₁₀ C ₂₀	3.927(1)	18(1)	135(7)	97.53	2.47	5.321	1.922	2.297
	N ₁₅ C ₁₅	3.926(1)	24(1)	84(4)	99.38	0.62	4.357	1.627	1.499
	N ₂₀ C ₁₀	3.925(1)	41(2)	11(1)	100	-	4.807	1.828	2.081
750 °C	N ₁₀ C ₂₀	3.929(4)	47(2)	128(7)	98.22	1.78	6.506	2.304	1.592
	N ₁₅ C ₁₅	3.928(1)	45(3)	134(5)	100	-	6.111	2.114	2.043
	N ₂₀ C ₁₀	3.927(1)	52(1)	127(7)	100	-	8.450	1.869	2.442

Figure 17: Rietveld pattern refinement of $\text{La}_{0.8}\text{Sr}_{0.2}\text{Ti}_{0.7}\text{Ni}_{0.15}\text{Cu}_{0.15}\text{O}_{3-\delta}$ as the cubic phase (Pm-3m) after reduction treatment at 800 °C. The observed XRD pattern is shown with x points within the theoretical model, the blue line shows the difference between the theoretical model and the experimental data. Finally, the expected peaks positions are shown above in green bars.



Discussing the RP-phase, it is evident from the results that new phases have emerged in the Ruddlesden-Popper (RP) phase, **Figure 18**. Among these phases, one is identified as a cubic nickel-copper alloy (ICSD n° 103063), and the other is identified as La_2SrO_x . However, it is apparent that the Ruddlesden-Popper perovskite host solid oxide was not preserved during the reduction treatment. In this context, it can be concluded that A_2O_3 was preferentially formed at the expense of the perovskite host solid oxide, **Equation 13**. Another critical factor influencing the evolution of the two new phases is the ease of Cu and Ni reduction. The B-site of the perovskite typically ensures the system's stability, and it is likely that all the content of the B-site was reduced, leading to damage to the host oxide phase.

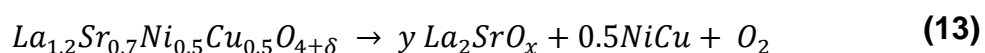
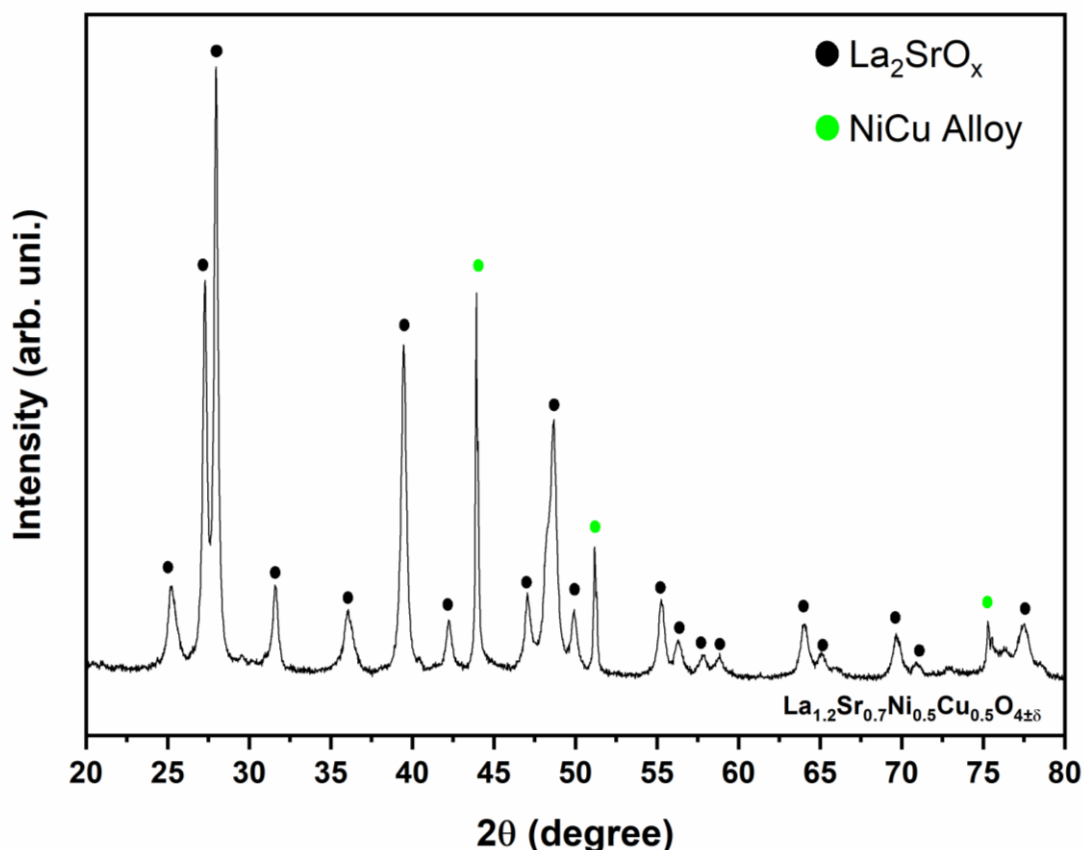


Figure 18: XRD pattern of RP-phase after reduction treatment at 900 °C for 10 h. The diffraction position corresponding to the La_2SrO_x structure is highlighted with a black circle, while the green circle indicates the diffraction position associated with the centered cubic Nickel-Copper alloy.



5.1.3 X-ray photoelectron spectroscopy

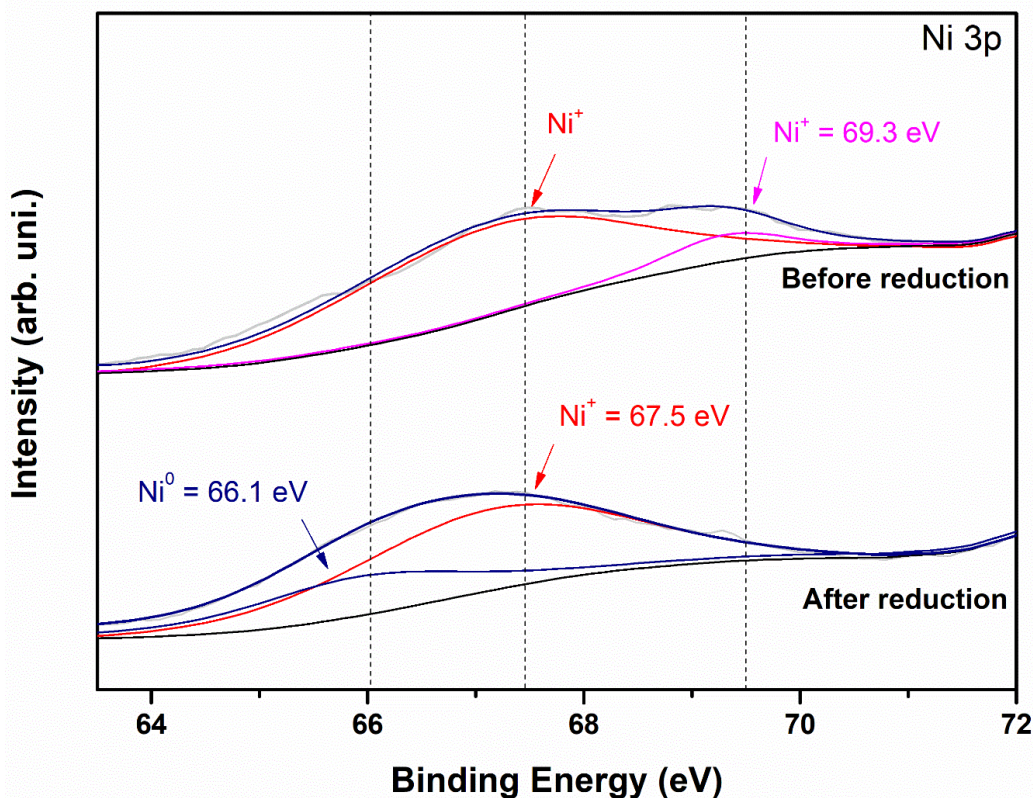
In perovskite structures, the valence of the B-site cations is a critical factor influencing electro-activity and structural stability. This characteristic can be harnessed to evaluate the effectiveness of the exsolution process. To achieve this, high-resolution X-ray Photoelectron Spectroscopy (XPS) measurements were used to analyze the surface composition and chemical state of copper and nickel in the sample both before and after the reduction treatment.

XPS analysis provides valuable information about the chemical environment and oxidation state of the elements on the sample's surface. By comparing the XPS spectra before and after reduction, it becomes possible to detect changes in the chemical species present, particularly in the case of metallic exsolved nanoparticles.

XPS analysis is commonly employed to identify the presence of metallic exsolved nanoparticles^{7,134,149}. However, due to the exsolution process, the metallic fraction is typically less than 1 wt%, which may fall below the sensitivity threshold of certain diffractometers¹⁵⁶. Nevertheless, XPS analysis remains valuable for providing accurate surface information, disclosing the valence state of species, and quantifying their concentrations.

The Ni 3p spectra was used to investigate the valence state of Ni in the RP phase, while for the titanates phase, the Ni 2p spectra was employed. **Figure 19** displays the 3p sublevel high-resolution spectra data acquired before reduction treatment. The peaks observed at a binding energy of 67.5 eV and 69.3 eV, are associated with the presence of Ni⁺ and Ni²⁺ respectively, in the RP phase¹³⁶. After reduction, it can be observed the presence of Ni⁰ at binding energy 66.1 eV, along with Ni⁺ at 67.5 eV^{136,157}.

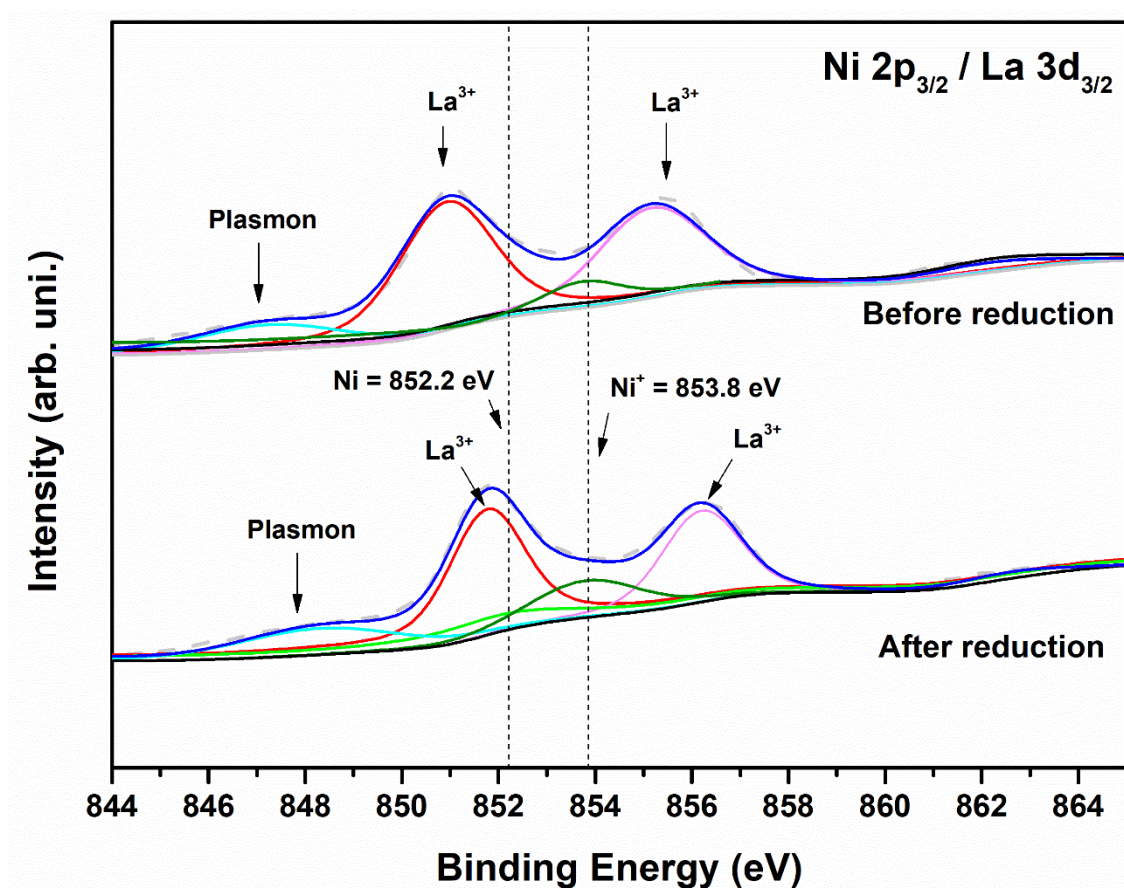
Figure 19 – High-resolution and deconvoluted XPS spectra of Ni 3p spectra of RP phase as prepared and after reduction treatment at 900 °C.



To investigate the presence of Ni on the titanate surface, high-resolution Ni 2p spectra were used. However, analyzing the Ni 2p spectra is challenging because

the Ni 2p_{2/3} peak partly overlaps with La 3d_{2/3}. To address this issue, a complex fitting approach was adopted, following the procedure described in a recent work by Martinez's group¹⁵⁸. In **Figure 20** it can be observed the Ni 2p_{2/3} / La 3d_{2/3} sublevel high-resolution spectra. The broad peak around ~848 eV is attributed to a plasmon peak, which is associated with the excitation of the conduction band electrons. The peaks at the binding energies of ~851 eV and ~856 eV were assigned to the presence of lanthanum on the surface sample. Additionally, peaks around 852.5 eV and 854.6 eV are ascribed to metallic nickel (Ni⁰) and Ni⁺, respectively.

Figure 20 – High-resolution and deconvoluted XPS spectra of Ni 2p_{3/2} and La 3d_{3/2} spectra of La_{0.8}Sr_{0.2}Ti_{0.7}Ni_{0.15}Cu_{0.15}O_{3-δ} as prepared and after reduction treatment at 900 °C.



In **Figure 21** and **Figure 22**, the Cu 2p_{3/2} of RP-phase and N₁₅C₁₅, respectively, are shown. In the 937 eV – 945 eV range, a broad peak is observed, which is attributed to a shake-up peak, the signal can be observed before and after reduction treatment. The shake-up peak arises from the reorganization caused by the electron ejection from the inner level, and one possibility in this phenomenon is the transition of the electron to a higher energy level (shake-up).

The peaks at the binding energy of ~ 932.1 eV, ~ 933.1 eV, and ~ 934.3 eV are attributed to Cu^0 , Cu^+ , and Cu^{2+} , respectively^{85,143}. Despite nickel and copper being more stable in the +2-oxidation state, they are reduced to the +1-oxidation state to maintain the principle of electroneutrality. As listed in **Table 4**, it can be observed the relative atomic percentage of all species. Hence, XPS data confirms the exsolution of NiCu nanoparticles in RP phase.

Figure 21: High-resolution and deconvoluted XPS spectra of Cu $2p_{3/2}$ spectra of RP phase as prepared and after reduction treatment at 900 °C.

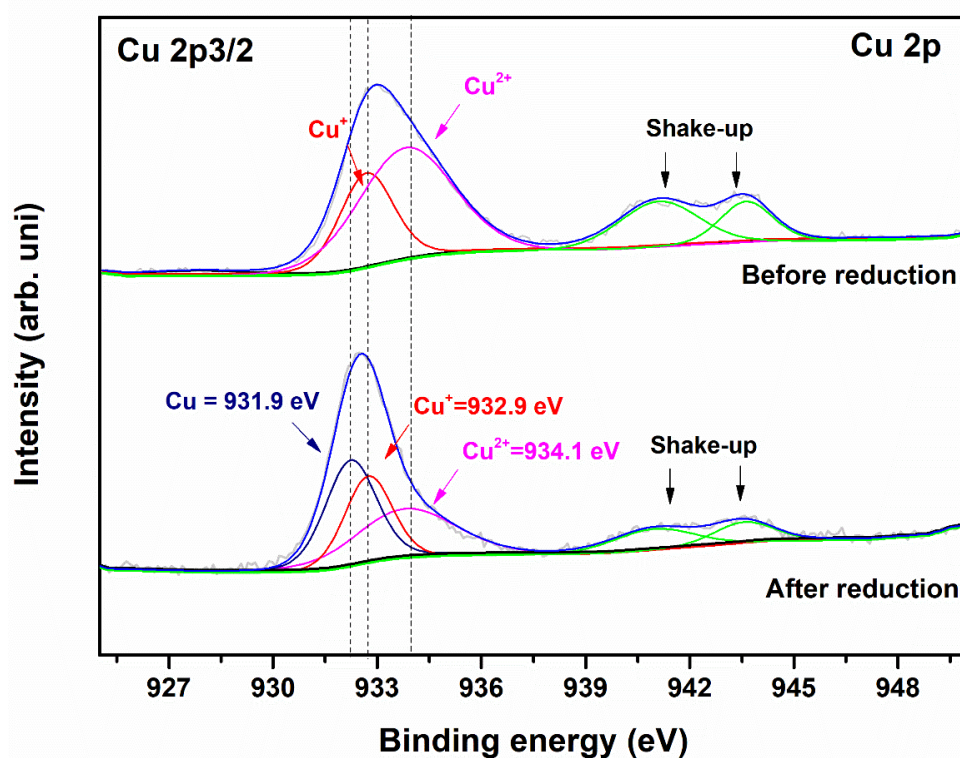


Figure 22: High-resolution and deconvoluted XPS spectra of Cu 2p_{3/2} spectra of La_{0.8}Sr_{0.2}Ti_{0.7}Ni_{0.15}Cu_{0.15}O_{3- δ} as prepared and after reduction treatment at 900 °C.

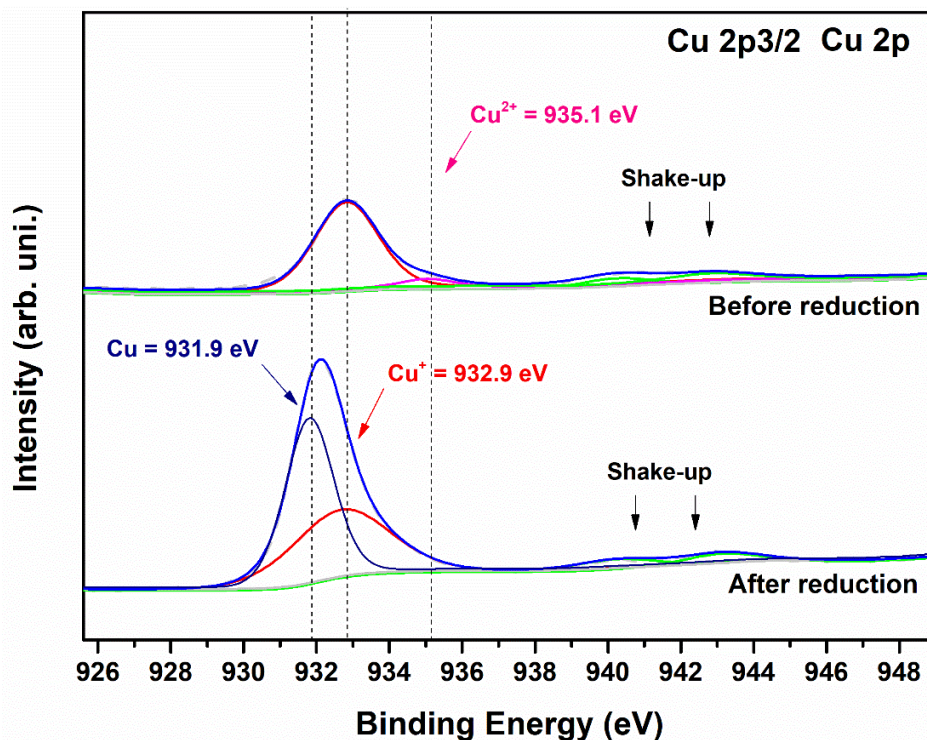


Table 4: XPS fitting results of Cu 2p, Ni 3p, and Ti 2p proportions as prepared and after reduction treatment.

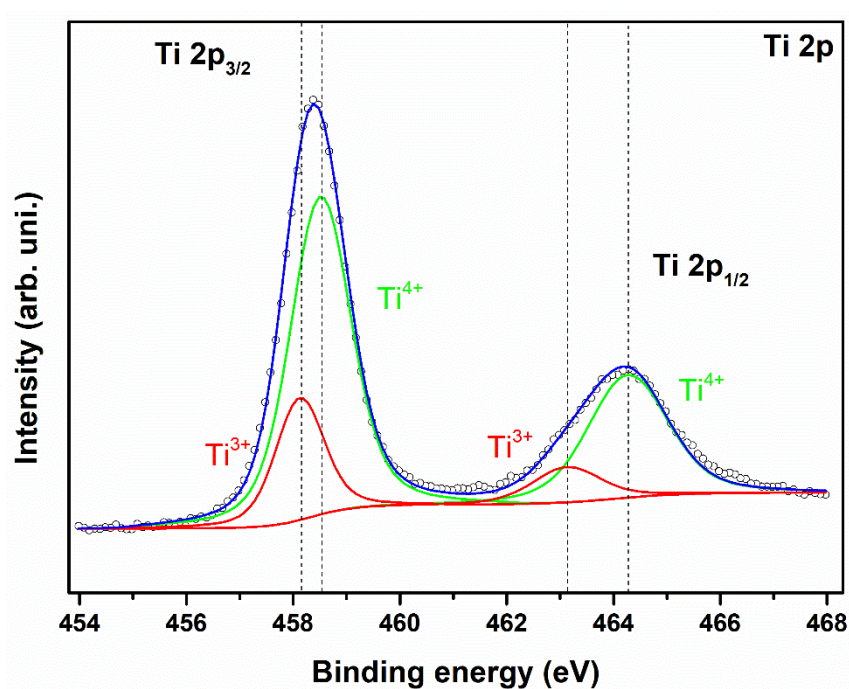
Sample	Cu ⁰ /Cu ⁺	Cu ⁰ /Cu ²⁺	Ni ⁰ /Ni ⁺	Ni ⁰ /Ni ²⁺	Ti ³⁺ /Ti ⁴⁺
N ₁₀ C ₂₀ calcined	0.0	0.0	0.0	0.0	0.2
N ₁₀ C ₂₀ exsolved	1.1	0.0	0.1	0.0	0.4
N ₁₅ C ₁₅ calcined	0.0	0.0	0.0	0.0	0.3
N ₁₅ C ₁₅ exsolved	1.2	0.0	0.1	0.0	0.5
N ₂₀ C ₁₀ calcined	0.0	0.0	0.0	0.0	0.3
N ₂₀ C ₁₀ exsolved	0.8	0.0	0.1	0.0	0.3
RP calcined	0.0	0.0	0.0	0.0	0.0
RP exsolved	0.6	1.1	0.3	0.0	0.0

Finally, XPS analysis provide crucial insights into the interference of titanium on electrical properties. **Figure 23** displays titanium 2p of La_{0.8}Sr_{0.2}Ti_{0.7}Ni_{0.15}Cu_{0.15}O_{3- δ} after reduction treatment at 900 °C. The main peaks are observed around 458.3 eV and 463.3 eV, indicating the presence of trivalent titanium (Ti³⁺). The presence of Ti³⁺ before reduction can be explained by the doping of copper and

nickel at the B-site, which can facilitate the reduction of titanium for better accommodation. After the reduction treatment, the increase in Ti^{3+} content is attributed to the reduction treatment itself.

In titanate-based perovskites, the electrical properties are closely tied to the presence of Ti^{3+} in the structure. This is due to the existence of the $\text{Ti}^{3+}/\text{Ti}^{4+}$ redox couple, which will be further discussed in the electrical properties section. For now, it is worth noting that XPS reveals a higher atomic percentage of Ti^{3+} in $\text{La}_{0.8}\text{Sr}_{0.2}\text{Ti}_{0.7}\text{Ni}_{0.2}\text{Cu}_{0.1}\text{O}_{3-\delta}$ and $\text{La}_{0.8}\text{Sr}_{0.2}\text{Ti}_{0.7}\text{Ni}_{0.15}\text{Cu}_{0.15}\text{O}_{3-\delta}$ samples.

Figure 23: High-resolution and deconvoluted XPS spectra of Ti $2p_{3/2}$ spectra of $\text{La}_{0.8}\text{Sr}_{0.2}\text{Ti}_{0.7}\text{Ni}_{0.15}\text{Cu}_{0.15}\text{O}_{3-\delta}$ after reduction treatment at 900 °C.



5.1.4 Electron Microscopy

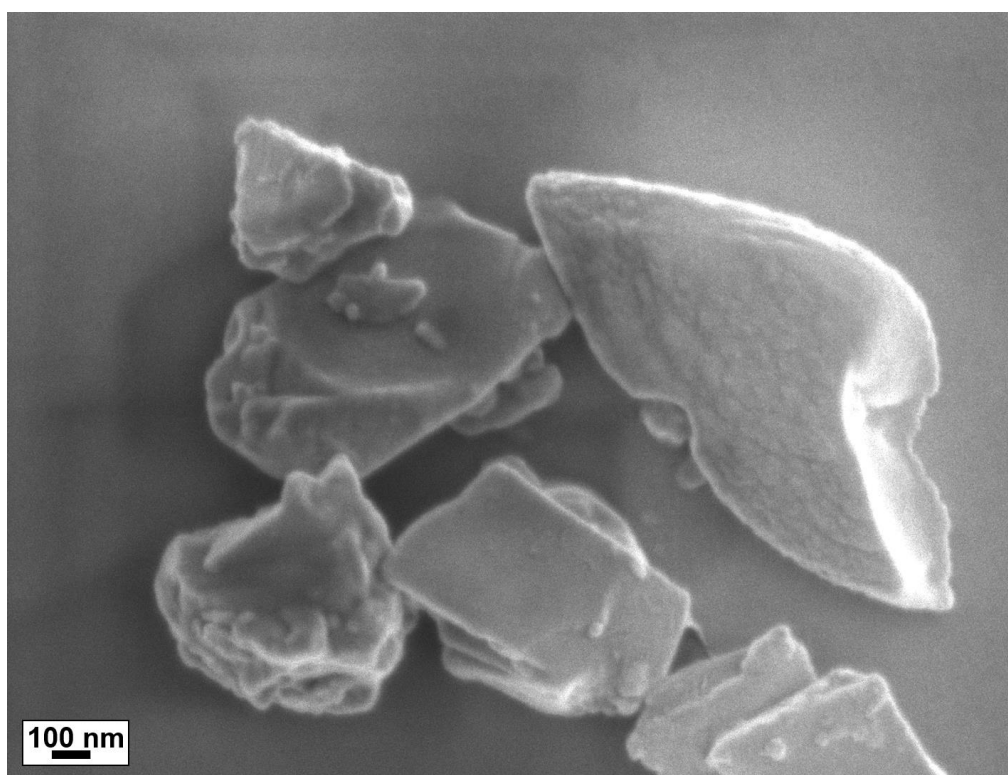
As discussed in previous topics verifying exsolved nanoparticles is not a trivial job. Indeed, the low metallic fraction and local distortions promoted by the

phenomenon turns tough the characterization through the most common characterization methods such as X-ray diffraction. Thus, other techniques must be employed aiming to identify and characterize the samples.

5.1.4.1 Scanning Electron Microscopy (SEM)

All the samples were characterized after calcination, the main goal of the analysis was to verify the morphology and observe the surface of each sample. **Figure 24** shows $\text{La}_{0.8}\text{Sr}_{0.2}\text{Ti}_{0.7}\text{Ni}_{0.1}\text{Cu}_{0.2}\text{O}_{3-\delta}$ after calcined. It can be observed particles bigger than 500 nm with no specific morphology, it was expected particles smaller than 1 μm due to the synthesis route. However, the size can be affected by furnace time and temperature, which leads to particle growth through sintering, this can explain why the particles were bigger than expected.

Figure 24: $\text{La}_{0.8}\text{Sr}_{0.2}\text{Ti}_{0.7}\text{Ni}_{0.1}\text{Cu}_{0.2}\text{O}_{3-\delta}$ calcined at 900 °C for 5 hours. Image obtained with 3 kV acceleration voltage.



After reduction treatment at 750°C, 800°C, 850°C, and 900°C, all samples were also characterized using a scanning electron microscope to investigate possible morphological changes and determine the effectiveness of the treatment on

nanoparticle exsolution. **Figure 25, Figure 26, Figure 27, and Figure 28** show the samples after reduction treatment at 750 °C, 800 °C, 850 °C, and 900 °C, respectively.

Figure 25: Scanning Electron Images of treatment $\text{La}_{0.8}\text{Sr}_{0.2}\text{Ti}_{0.7}\text{Ni}_{0.15}\text{Cu}_{0.15}\text{O}_{3-\delta}$ (a), $\text{La}_{0.8}\text{Sr}_{0.2}\text{Ti}_{0.7}\text{Ni}_{0.2}\text{Cu}_{0.1}\text{O}_{3-\delta}$ (b), $\text{La}_{0.8}\text{Sr}_{0.2}\text{Ti}_{0.7}\text{Ni}_{0.1}\text{Cu}_{0.2}\text{O}_{3-\delta}$ (c) after reduction at 750 °C.

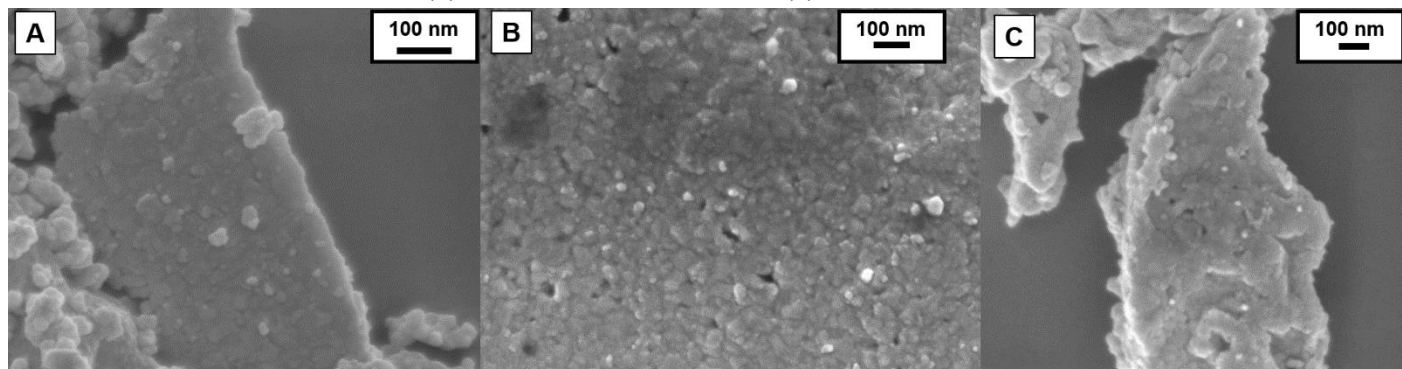


Figure 26: Scanning Electron Images of treatment $\text{La}_{0.8}\text{Sr}_{0.2}\text{Ti}_{0.7}\text{Ni}_{0.15}\text{Cu}_{0.15}\text{O}_{3-\delta}$ (a), $\text{La}_{0.8}\text{Sr}_{0.2}\text{Ti}_{0.7}\text{Ni}_{0.2}\text{Cu}_{0.1}\text{O}_{3-\delta}$ (b), $\text{La}_{0.8}\text{Sr}_{0.2}\text{Ti}_{0.7}\text{Ni}_{0.1}\text{Cu}_{0.2}\text{O}_{3-\delta}$ (c) after reduction at 800 °C.

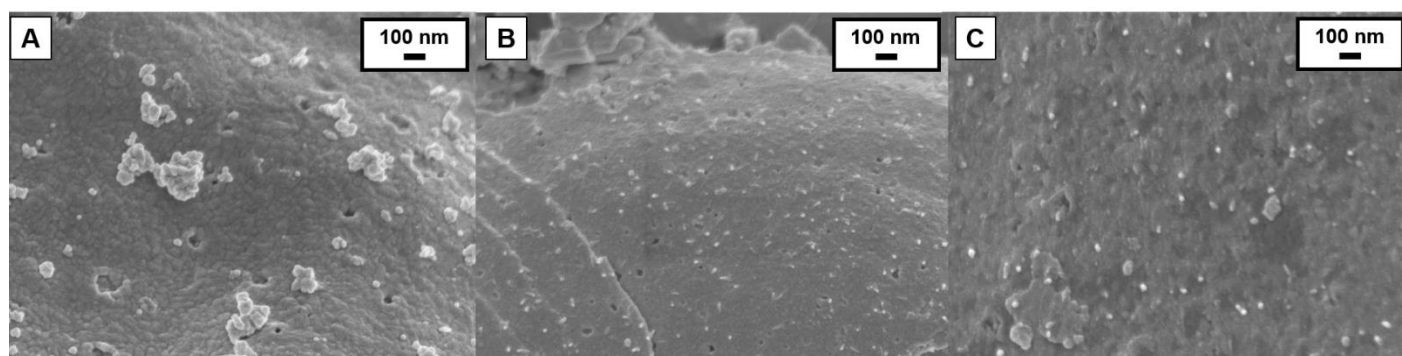


Figure 27: Scanning Electron Images of treatment $\text{La}_{0.8}\text{Sr}_{0.2}\text{Ti}_{0.7}\text{Ni}_{0.15}\text{Cu}_{0.15}\text{O}_{3-\delta}$ (a), $\text{La}_{0.8}\text{Sr}_{0.2}\text{Ti}_{0.7}\text{Ni}_{0.2}\text{Cu}_{0.1}\text{O}_{3-\delta}$ (b), $\text{La}_{0.8}\text{Sr}_{0.2}\text{Ti}_{0.7}\text{Ni}_{0.1}\text{Cu}_{0.2}\text{O}_{3-\delta}$ (c) after reduction at 850 °C.

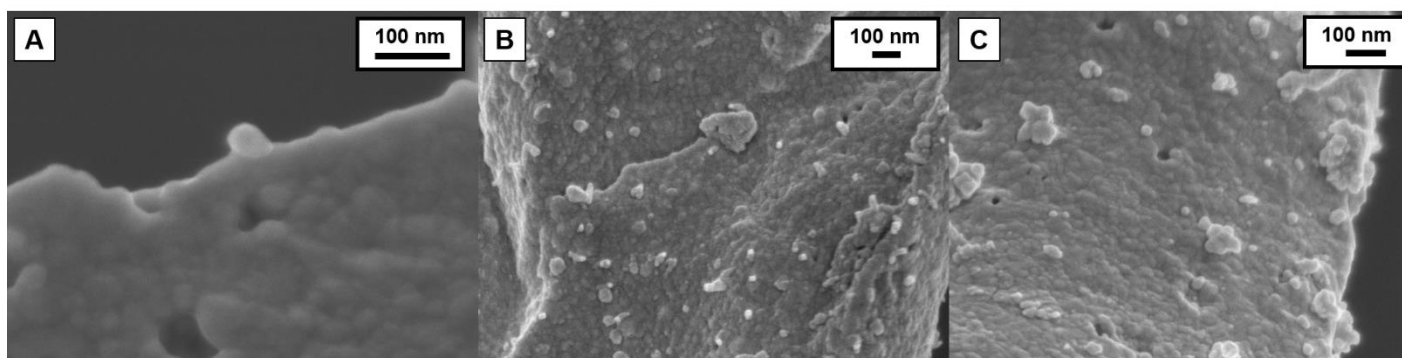
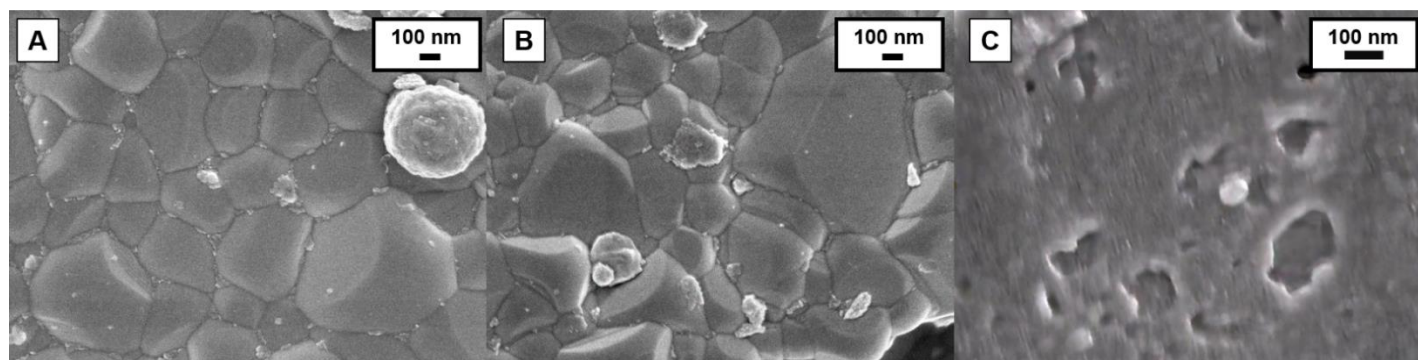


Figure 28: Scanning Electron Images of treatment $\text{La}_{0.8}\text{Sr}_{0.2}\text{Ti}_{0.7}\text{Ni}_{0.15}\text{Cu}_{0.15}\text{O}_{3-\delta}$ (a), $\text{La}_{0.8}\text{Sr}_{0.2}\text{Ti}_{0.7}\text{Ni}_{0.2}\text{Cu}_{0.1}\text{O}_{3-\delta}$ (b), $\text{La}_{0.8}\text{Sr}_{0.2}\text{Ti}_{0.7}\text{Ni}_{0.1}\text{Cu}_{0.2}\text{O}_{3-\delta}$ (c) after reduction at 900 °C.

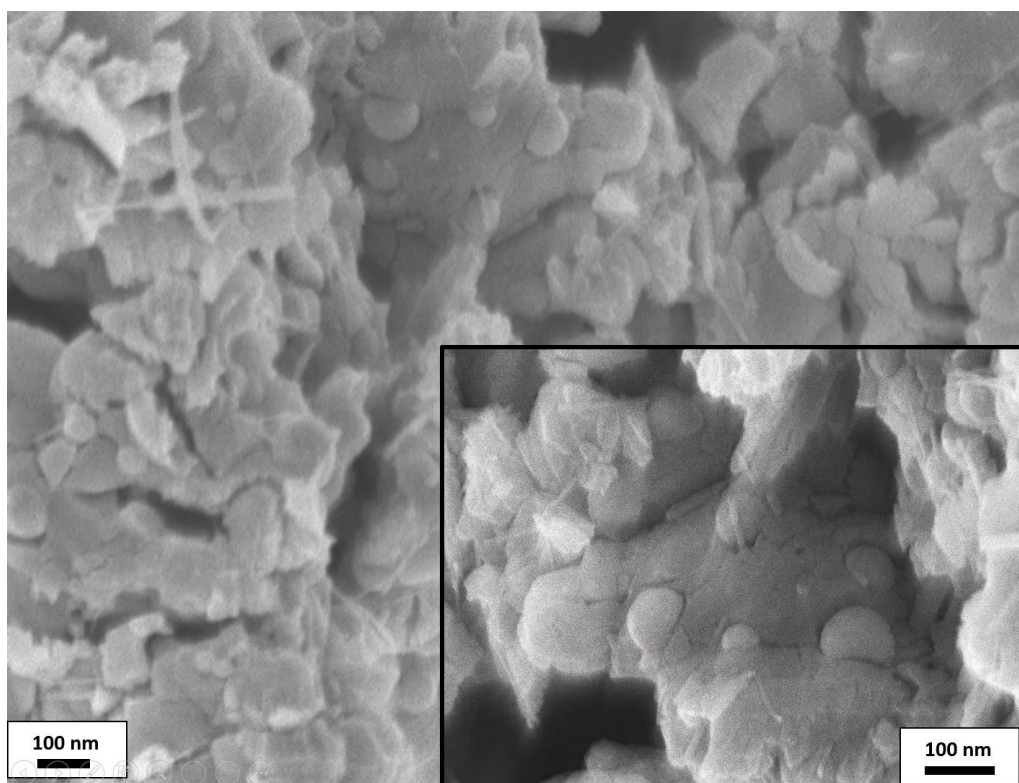


In contrast to the findings obtained through XRD analysis and Rietveld refinement, SEM corroborates the presence of spherical-shaped nanoparticles firmly anchored to the surface of the samples across all compositions. However, it is worth noting that during the measurements, certain limitations arose due to technical issues with the video card, resulting in compromised image quality and resolution. Nonetheless, despite these limitations, the observed spherical nanoparticles exhibited an average size ranging from 30 nm to 50 nm.

It can be observed that at 900 °C the sample sintered and formed some grain boundaries. Owing to the higher diffusion rate of atoms through the grain boundary, it is possible to observe that most of the exsolved nanoparticles are on top of the grain boundary or close to it. It is important to emphasize that the SEM analysis provided invaluable insights into the morphology and distribution of the nanoparticles, shedding light on their behavior under the influence of temperature variations. Nonetheless, the technical limitations should be acknowledged when interpreting the SEM results.

Finally, **Figure 29** shows the RP phase after the reduction step. As previously discussed in the XRD analysis section, probably all Nickel and Copper content at B-site was exsolved. This fact could explain the presence of a bigger spherical nanoparticles shape, with size around of 70 nm.

Figure 29: Scanning Electron Images of treatment $\text{La}_{1.2}\text{Sr}_{0.7}\text{Ni}_{0.5}\text{Cu}_{0.5}\text{O}_{4+x\delta}$ after reduction at 900 °C.



5.1.4.2 Transmission Electron Microscopy (TEM)

Scanning electron microscopy (SEM) proved to be effective in showing nanoparticles anchored on the sample surface; however, without EDX analysis support, the technique is not capable of determining the chemical nanoparticle composition. In contrast, transmission electron microscopy (TEM) is well-suited for investigating local distortions such as exsolution phenomena and allows for the investigation of nanoparticle content through electron diffraction. Therefore, TEM was applied with the aim of investigating the nanoparticle composition.

Figure 30 displays $\text{La}_{0.8}\text{Sr}_{0.2}\text{Ti}_{0.7}\text{Ni}_{0.2}\text{Cu}_{0.1}\text{O}_{3-\delta}$ HRTEM image that was taken after reduction at 800 °C for 10 hours, revealing a clear heterojunction between the host solid oxide and the nanoparticle. In the image, the blue square highlights the perovskite host. The Inverse Fast Fourier Transform (IFFT) was performed on the area within the blue square, allowing the observation of two main diffraction points that index with planes (1 1 1) with a plane distance of 0.223 nm and (1 1

0) with a plane distance of 0.271 nm. Both values are close to those of lanthanum titanate perovskite, which corroborates with the XRD analysis.

Additionally, in the same image shown in **Figure 30**, a spherical nanoparticle is observed attached to the surface, and a red square indicates the IFFT of that area. In the IFFT, only one diffraction point is observed, presenting the same distance as the copper-nickel (2 0 0) plane. Another crucial piece of information obtained from the TEM images is the presence of amorphous regions around the nanoparticle. Nickel and copper easily oxidize at room temperature, and the amorphous region around the nanoparticle is likely the formation of nickel and copper oxides.

Figure 30: High Resolution Transmission Electron Images (HRTEM) of $\text{La}_{0.8}\text{Sr}_{0.2}\text{Ti}_{0.7}\text{Ni}_{0.2}\text{Cu}_{0.1}\text{O}_{3-\delta}$ after reduction treatment at 800 °C for 10 hours.

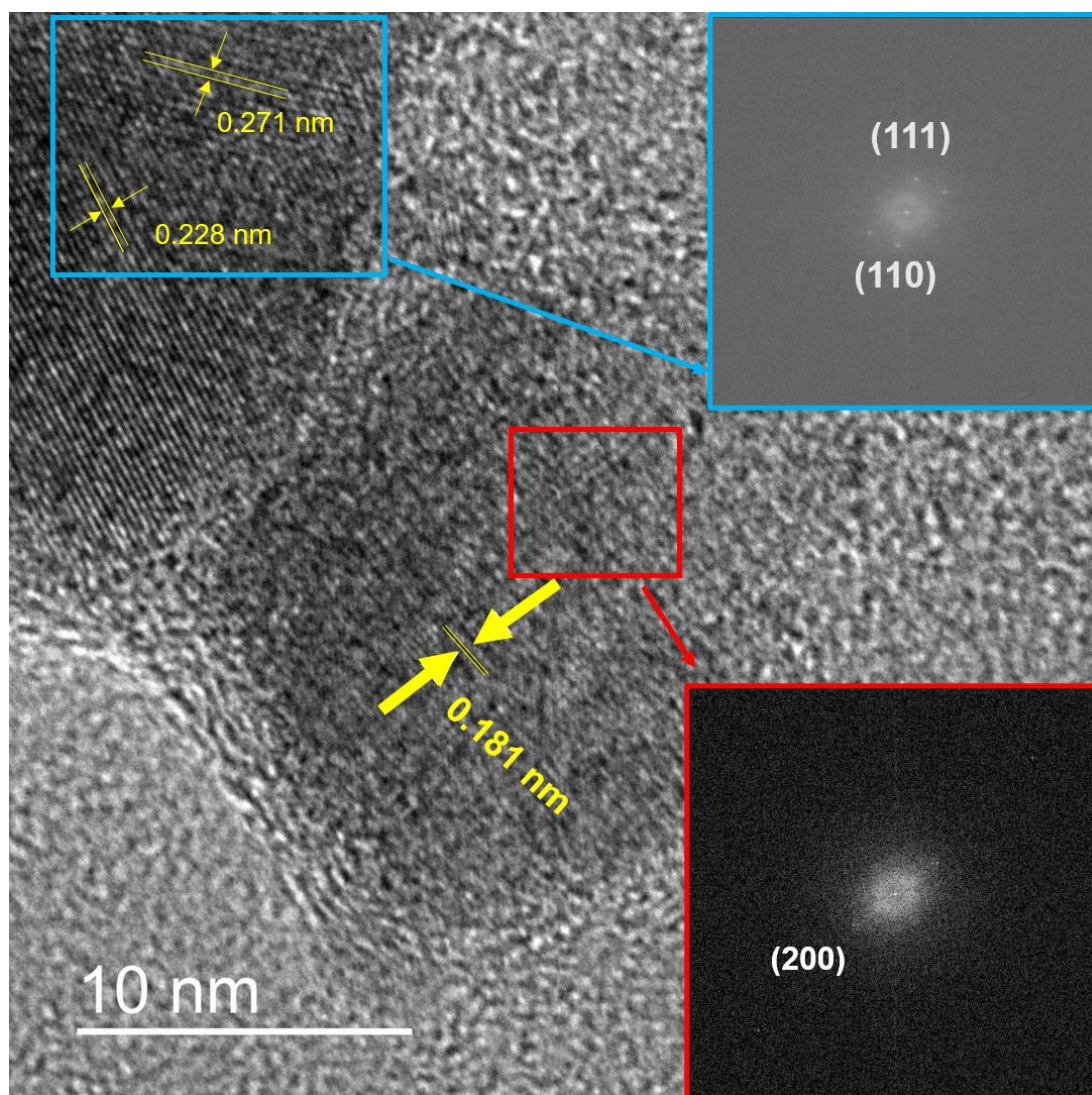


Figure 31 displays $\text{La}_{0.8}\text{Sr}_{0.2}\text{Ti}_{0.7}\text{Ni}_{0.15}\text{Cu}_{0.15}\text{O}_{3-\delta}$ reduced at 800 °C for 10 hours HRTEM images. It can be observed that the nanoparticle is strongly anchored at the matrix surface. The red square indicates the spherical nanoparticle IFFT and shows only one diffraction point which index with (2 0 0) plane and 0.177 nm interplanar spacing. The difference between this interplanar spacing and the previous is owing to the nanoparticle composition, probably this nanoparticle can present a high content of copper. The results present coherence with XRD and Rietveld refinement analysis.

Figure 31: High Resolution Transmission Electron Images (HRTEM) of $\text{La}_{0.8}\text{Sr}_{0.2}\text{Ti}_{0.7}\text{Ni}_{0.15}\text{Cu}_{0.15}\text{O}_{3-\delta}$ after reduction treatment at 800 °C for 10 hours.

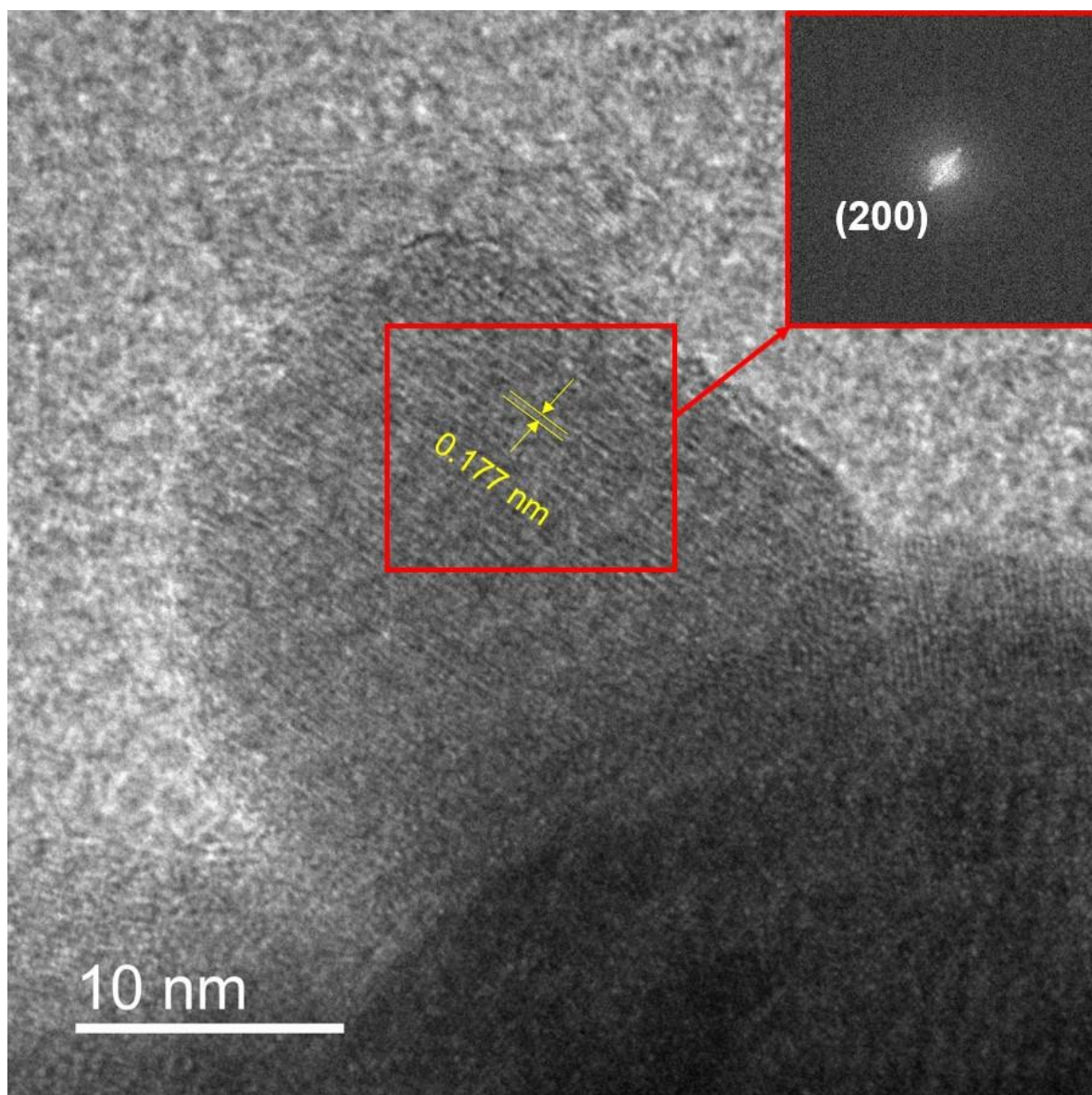
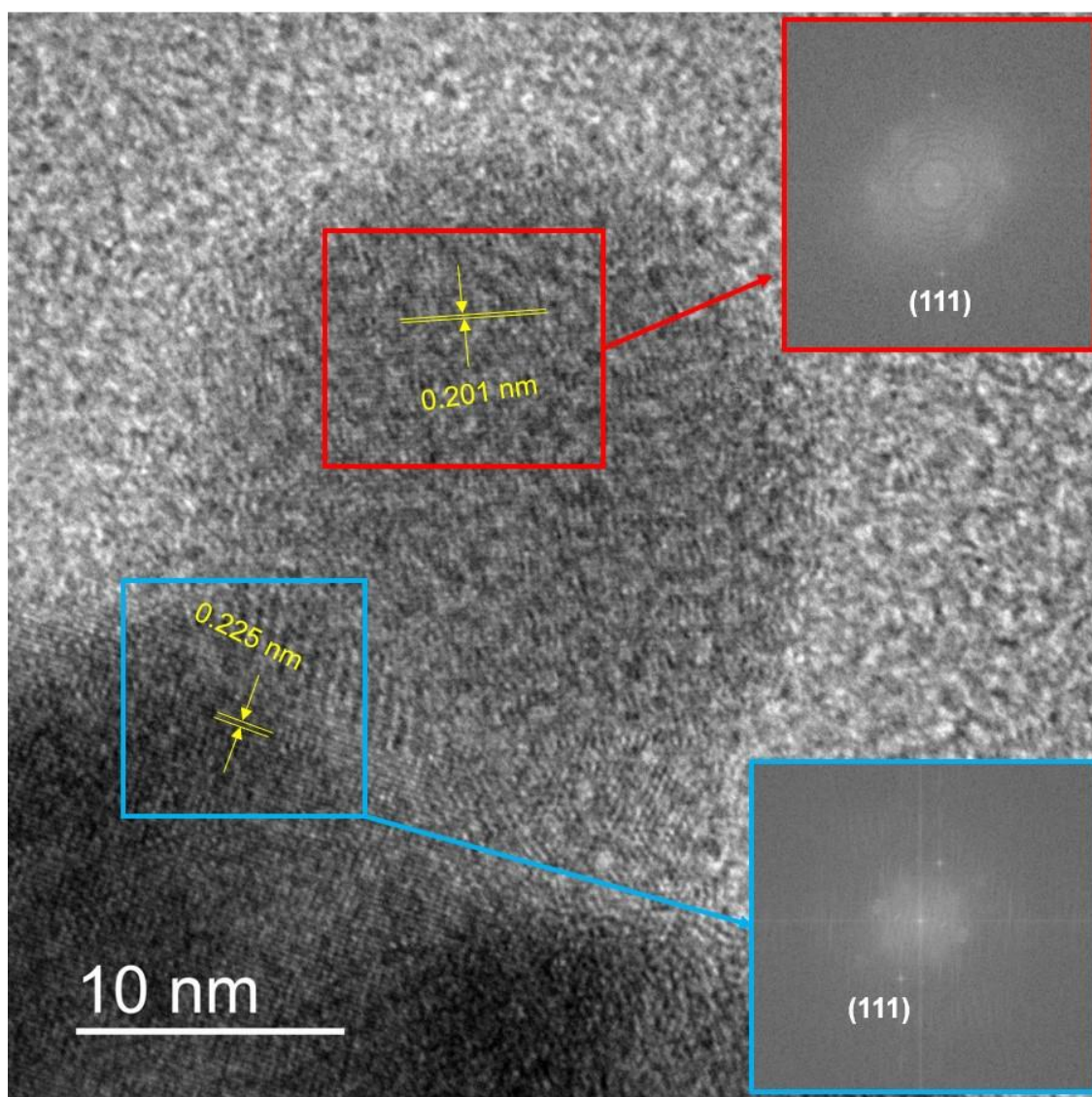


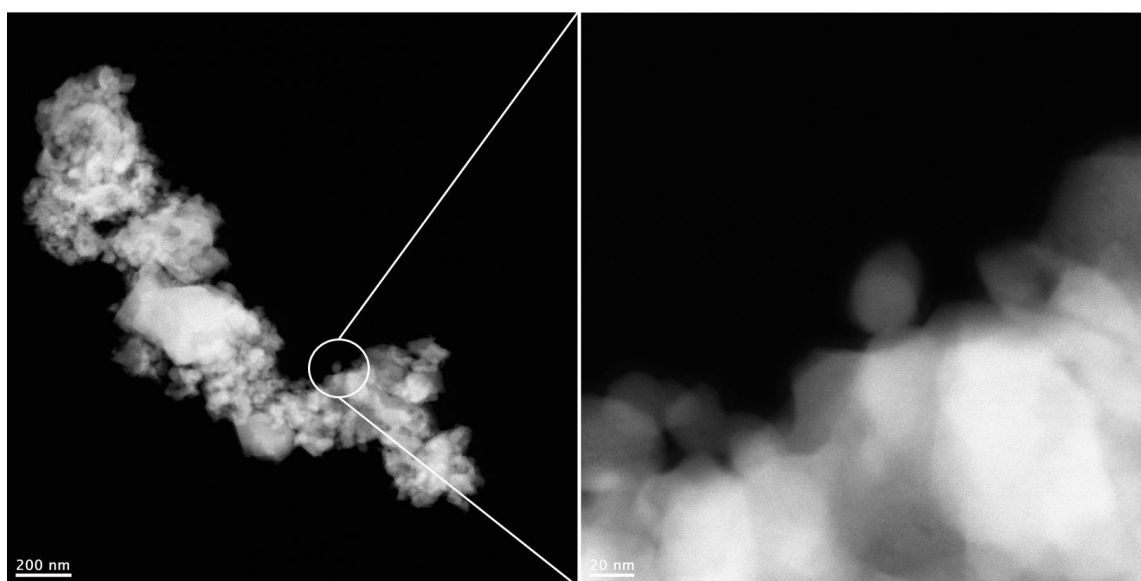
Figure 32 shows $\text{La}_{0.8}\text{Sr}_{0.2}\text{Ti}_{0.7}\text{Ni}_{0.15}\text{Cu}_{0.15}\text{O}_{3-\delta}$ reduced at 800 °C for 10 hours HRTEM images. One more time, it can be easily observed a heterojunction between nanoparticle and host solid oxide. Due to low signal only one distance could be found which is 0.201 nm and indexes with (1 1 1) copper-nickel plane. The red square shows the spherical nanoparticle area IFFT. Matrix analysis show only one diffraction point with a plane distance equal 0.225 nm which closely corresponds to plane (1 1 1) conforming previous results obtained at XRD analysis.

Figure 32: High Resolution Transmission Electron Images (HRTEM) of $\text{La}_{0.8}\text{Sr}_{0.2}\text{Ti}_{0.7}\text{Ni}_{0.1}\text{Cu}_{0.2}\text{O}_{3-\delta}$ after reduction treatment at 800 °C for 10 hours.



Finally, **Figure 33** shows STEM images acquired with a High-angle annular dark-field (HAADF) detector of the same region of the TEM image is displayed at **Figure 31**. A clear contrast difference can be observed between the nanoparticle and matrix. HAADF detector strongly relies on sample composition as the higher atomic number greater are the scattering. Hence, it can be concluded that contrast is owing to the compositional difference.

Figure 33: STEM-HAADF image of $\text{La}_{0.8}\text{Sr}_{0.2}\text{Ti}_{0.7}\text{Ni}_{0.15}\text{Cu}_{0.15}\text{O}_{3-\delta}$ after reduction treatment at 800 °C for 10 hours



5.1.5 Dilatometry

Verifying ceramics electrical properties in some cases requires a sintering process to densify and promote ionic or electronic conduction. Aiming to investigate the samples sintering temperature and furnace time, dilatometry tests were performed.

The RP and $\text{N}_{15}\text{C}_{15}$ samples were submitted to this test. **Figure 34** shows the dilatometry curve of the RP phase, two sintering phenomena can be observed at approximately 1055 °C and 1150 °C. The higher temperature with the biggest densification tax was employed to sinter the sample, in that case approximately 1150 °C. Thereafter, an isothermal analysis of the RP phase was performed at the sintering temperature aiming to predict the time required to obtain 92% densification. This percentage is related to the minimum densification to avoid the

direct passage of hydrogen and water throughout the anode. **Figure 35** shows isothermal analysis at 1150 °C for 2 h, the data treatment provides the calculation of 12 h in a furnace to reach a 92% densified ceramic.

Figure 34: Dilatometry curve of $\text{La}_{1.2}\text{Sr}_{0.7}\text{Cu}_{0.5}\text{Ni}_{0.5}\text{O}_{4\pm\delta}$ from room temperature to 1500 °C in nitrogen.

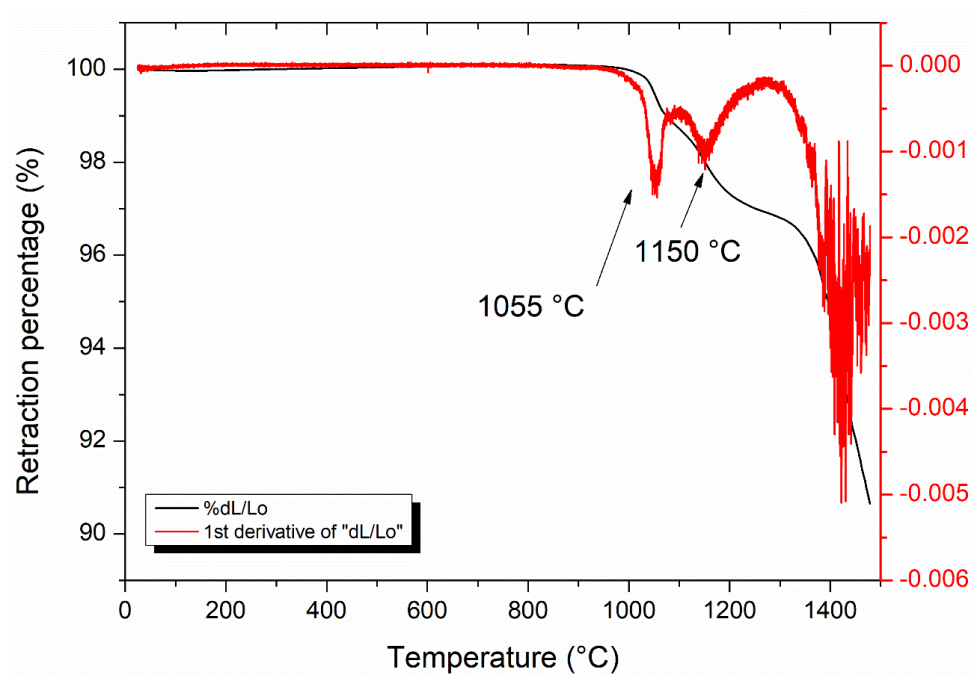
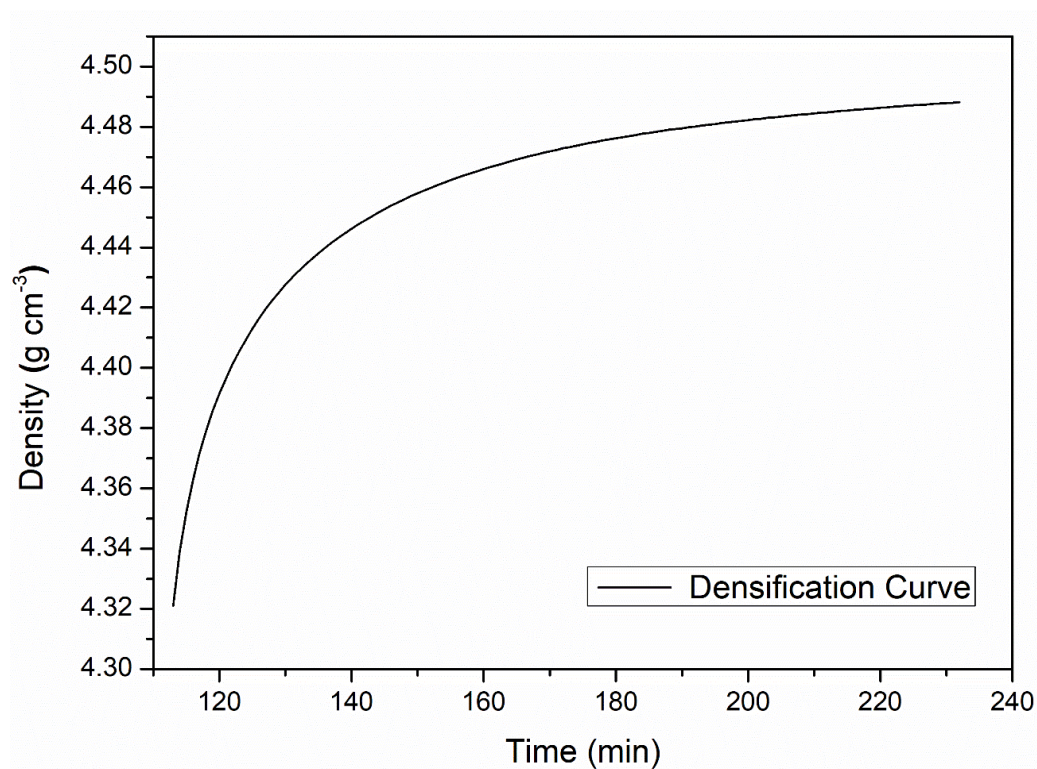
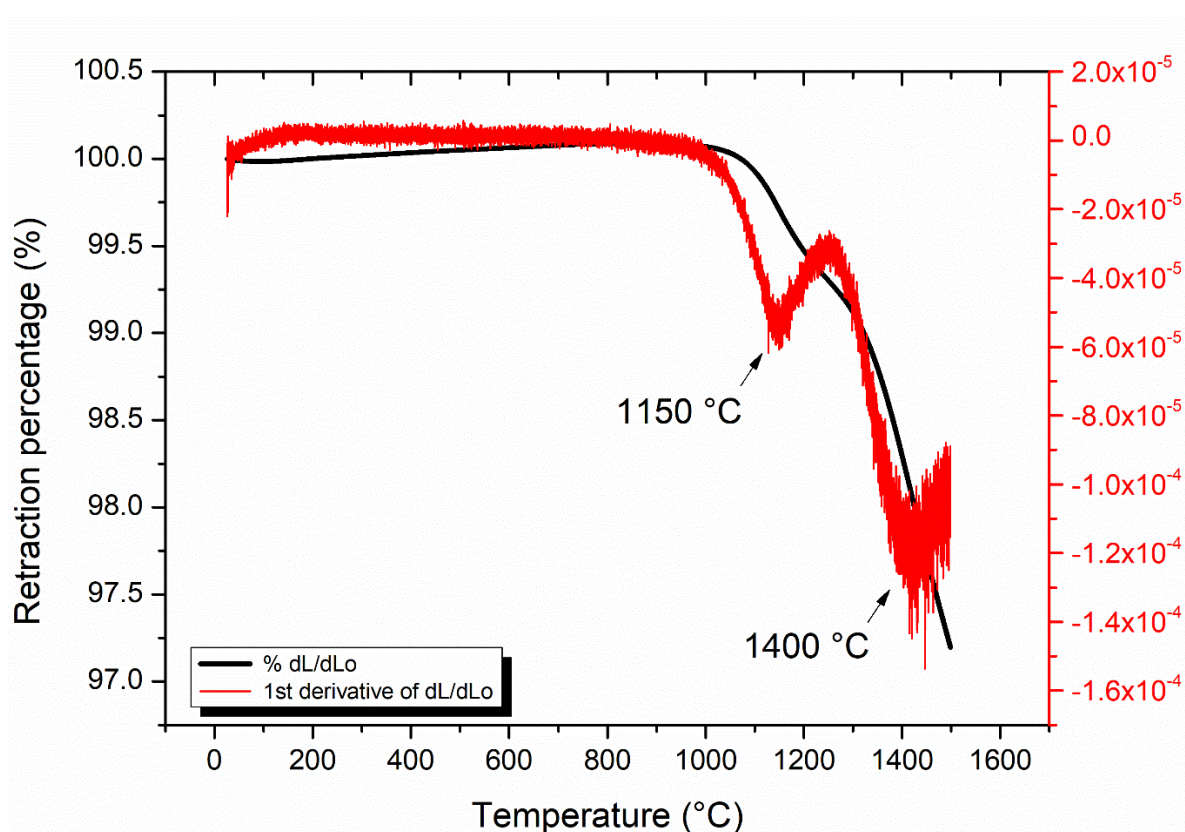


Figure 35: Ruddlesden-popper phase isothermal curve in 1150 °C for 2 h in function of sample density



A similar process was performed to understand the titanate samples behavior. **Figure 36** shows the dilatometry curve of the $N_{15}C_{15}$. Two sintering phenomena can be observed during the heating ramp. The first one rises to approximately 1150 °C, followed by another at 1400 °C. The accuracy of these data allowed the choice of the sintering temperature. **Figure 37** shows isothermal analysis at 1400 °C for 1 h, within this data was able to predict that the heat treatment should be around 13 h in a furnace to reach a 92% densified ceramic.

Figure 36: Dilatometry curve of $La_{0.8}Sr_{0.2}Ti_{0.7}Ni_{0.15}Cu_{0.15}O_{3-\delta}$ from room temperature to 1500 °C in nitrogen.



Another relevant data acquired with the accuracy of dilatometry was the thermal coefficient of expansion (TEC). **Figure 38** shows the cooling ramp of $N_{15}C_{15}$. TEC was determined by the slope of the curve, for the sample was found as $6.41 \times 10^{-6} \text{ K}^{-1}$ and $7.15 \times 10^{-5} \text{ K}^{-1}$ for RP phase. It is substantially lower when compared with the most common electrolytes TEC values, which vary from 10 to $12 \times 10^{-6} \text{ K}^{-1}$ for LSGM, YSZ, SDC, and CGO^{159,160}.

Figure 37: $\text{La}_{0.8}\text{Sr}_{0.2}\text{Ti}_{0.7}\text{Ni}_{0.15}\text{Cu}_{0.15}\text{O}_{3-\delta}$ Isothermal curve in 1150 °C for 2 h in function of sample density

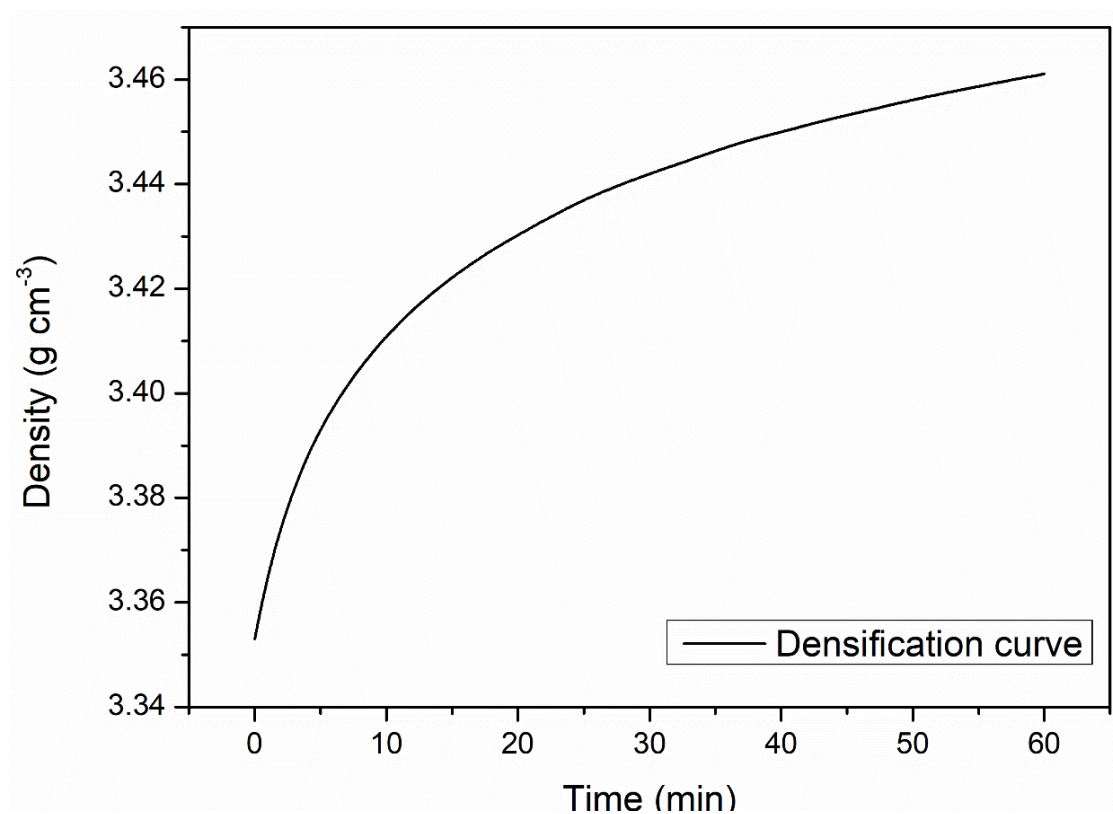
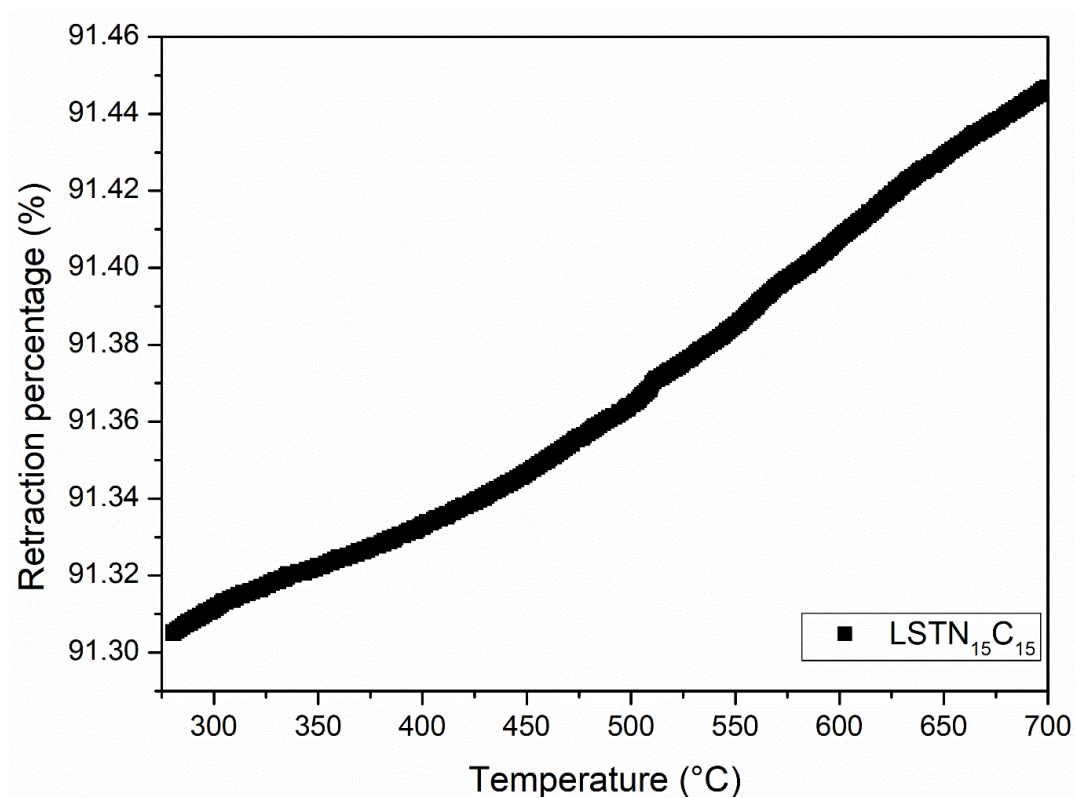


Figure 38: Cooling ramp of $\text{La}_{0.8}\text{Sr}_{0.2}\text{Ti}_{0.7}\text{Ni}_{0.15}\text{Cu}_{0.15}\text{O}_{3-\delta}$.



5.2 Electrical properties

In this section, the electrical properties will be discussed, focusing on the results obtained through electrochemical impedance spectroscopy. This technique sheds light on the electrical behavior of all samples under different conditions, including static air atmosphere, reducing atmosphere, and temperatures ranging from 250 °C to 650 °C.

The electrical impedance of a system can be described by **Equation 14**, where Z represents the impedance associated with the system, Z' (resistive) is the real part, and Z'' (capacitive) is the imaginary part.

$$Z = Z' + jZ'' \quad (14)$$

The Nyquist diagram is a way to present the impedance results, and the plot shows both the imaginary and real parts of impedance. Typically, the diagrams display a succession of semicircles, representing various contributions to the total electrical impedance of the material under test. The resistance can be determined by observing the intersection on the Z' axis or through extrapolation. Additionally, the capacitance can be calculated using **Equation 15**, where ω_{Apex} is the frequency of maximum loss.

$$C = \frac{1}{R\omega_{apex}} \quad (15)$$

Figure 39 shows the Nyquist diagram of $Ni_{10}C_{20}$, it can be observed two semicircles related to the bulk resistance and other with grain boundary resistance associated with the properties of the sample. The total conductivity can be calculated using **Equation 16**. Where σ is the total conductivity, l is the thickness, A is the surface area of the sample and, finally, R_s is the resistance of the sample.

$$\sigma = \frac{l}{R_s A} \quad (16)$$

In these perovskite systems, charged oxygen vacancies are the most important factors for electrical conduction, and this process is thermally activated. The total conduction in $La_{0.8}Sr_{0.2}Ti_{0.7}Ni_{0.2-x}Cu_xO_{3-\delta}$ is mainly attributed to the presence of oxygen vacancies, which create conditions for electron or ion conduction. In this case, the vacancies are created by doping at the B-site and A-site. All resistance

values are accessible in **Table 5**, which presents the total conductivity and resistance of each sample under a static air atmosphere.

Figure 39: The Nyquist diagram of $\text{La}_{0.8}\text{Sr}_{0.2}\text{Ti}_{0.7}\text{Ni}_{0.1}\text{Cu}_{0.2}\text{O}_{3-\delta}$ impedance at 300 °C

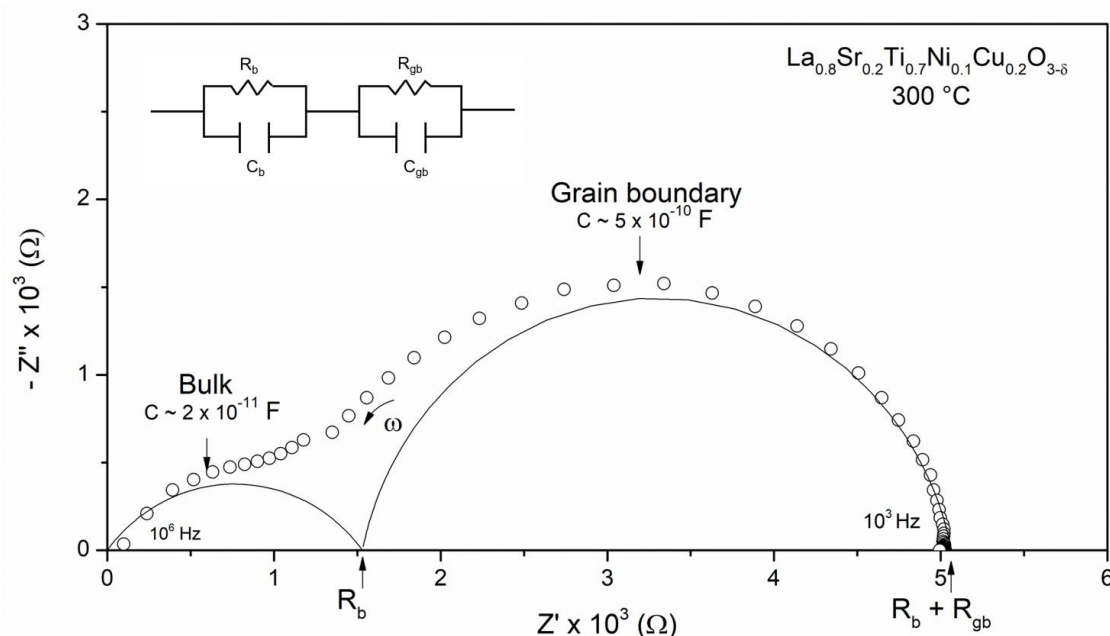


Table 5: Temperature (K), DC resistance ($\Omega \text{ cm}^{-1}$), and total conductivity (S cm^{-1}) for each sample

Sample	Temperature (K)	$\rho_{\text{DC}} (\Omega \cdot \text{cm}^{-1})$	$\sigma (\text{S cm}^{-1})$
$\text{La}_{0.8}\text{Sr}_{0.2}\text{Ti}_{0.7}\text{Ni}_{0.2}\text{Cu}_{0.1}\text{O}_{3-\delta}$	432	1.2×10^7	7.8×10^{-8}
	445	1.1×10^7	9.0×10^{-8}
	478	2.3×10^6	4.3×10^{-7}
	528	8.1×10^5	1.2×10^{-6}
	575	1.5×10^5	6.4×10^{-6}
	620	8.6×10^4	1.1×10^{-5}
	664	21278.6	4.7×10^{-5}
	714	8897.3	1.1×10^{-4}
	749	4203.0	2.4×10^{-4}
	798	2073.8	4.8×10^{-4}
	839	1034.0	9.7×10^{-4}
	880	552.9	1.8×10^{-3}
	920	291.3	3.4×10^{-3}
$\text{La}_{0.8}\text{Sr}_{0.2}\text{Ti}_{0.7}\text{Ni}_{0.15}\text{Cu}_{0.15}\text{O}_{3-\delta}$	960	160.0	6.2×10^{-3}
	446	2.9×10^7	3.4×10^{-8}
	478	2.4×10^6	4.1×10^{-7}
	530	1.2×10^6	8.3×10^{-7}
	576	2.4×10^5	4.1×10^{-6}
	622	1.3×10^5	7.7×10^{-6}
	665	18338.5	5.4×10^{-5}

	714	7537.8	1.3×10^{-4}
	748	3454.8	2.9×10^{-4}
	797	1682.6	5.9×10^{-4}
	839	815.7	1.2×10^{-3}
	879	435.3	2.3×10^{-3}
	918	225.2	4.4×10^{-3}
	961	124.0	8.0×10^{-3}
La _{0.8} Sr _{0.2} Ti _{0.7} Ni _{0.1} Cu _{0.2} O _{3-δ}	442	2.6×10^7	3.8×10^{-8}
	485	9.3×10^6	1.0×10^{-7}
	529	4.5×10^6	2.2×10^{-7}
	575	7.8×10^5	1.2×10^{-6}
	617	3.5×10^5	2.8×10^{-6}
	665	28350.0	4.4×10^{-6}
	714	15528	8.1×10^{-6}
	748	9919.3	1.3×10^{-5}
	797	6030.7	2.1×10^{-5}
	839	3884.1	3.2×10^{-5}
	879	2359.7	5.3×10^{-5}
	918	1512.8	8.3×10^{-5}
	961	948.3	1.3×10^{-4}

In comparison, Ashok's group found $4.9 \times 10^{-4} \text{ S cm}^{-1}$ for La_{0.8}Sr_{0.2}TiO_{3-δ} at 923 K. This work shows that the presence of nickel and copper in the composition enhanced 10 times the total conductivity of the samples at the same temperature¹⁶¹.

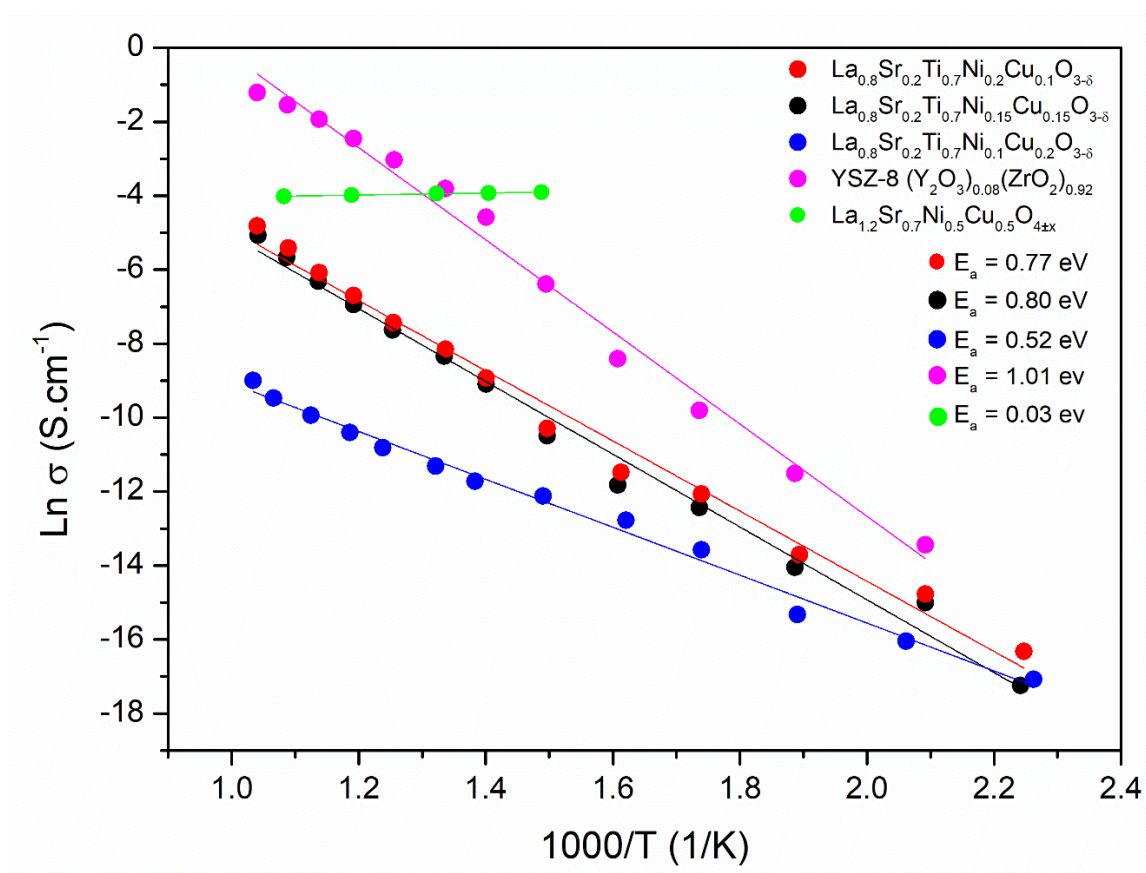
DC resistance was found to decrease with the increase of temperature, this fact indicates that the conduction is thermally activated. The Arrhenius plot can provide information about the activation energy of the carriers for the conduction process. **Equation 17** shows the Arrhenius linearized equation where E_a is the activation energy, T is the absolute temperature, k_B is the Boltzmann constant ($8.61 \times 10^{-5} \text{ eV/K}$) and σ_0 is a pre-exponential factor.

$$\ln \sigma = \ln \sigma_0 - \frac{1}{k_B T} E_a \quad (17)$$

Figure 40 shows the Arrhenius plot of all samples, displaying a linear behavior where the slope of this linear function represents the activation energy. It is evident from the plot that as the temperature increases, the total conductivity also

increases. Another significant inference from the Arrhenius plot is the absence of variation in the slope, indicating a consistent conduction mechanism throughout the temperature range.

Figure 40: Arrhenius plot of total conductivity with variation of reciprocal temperature.



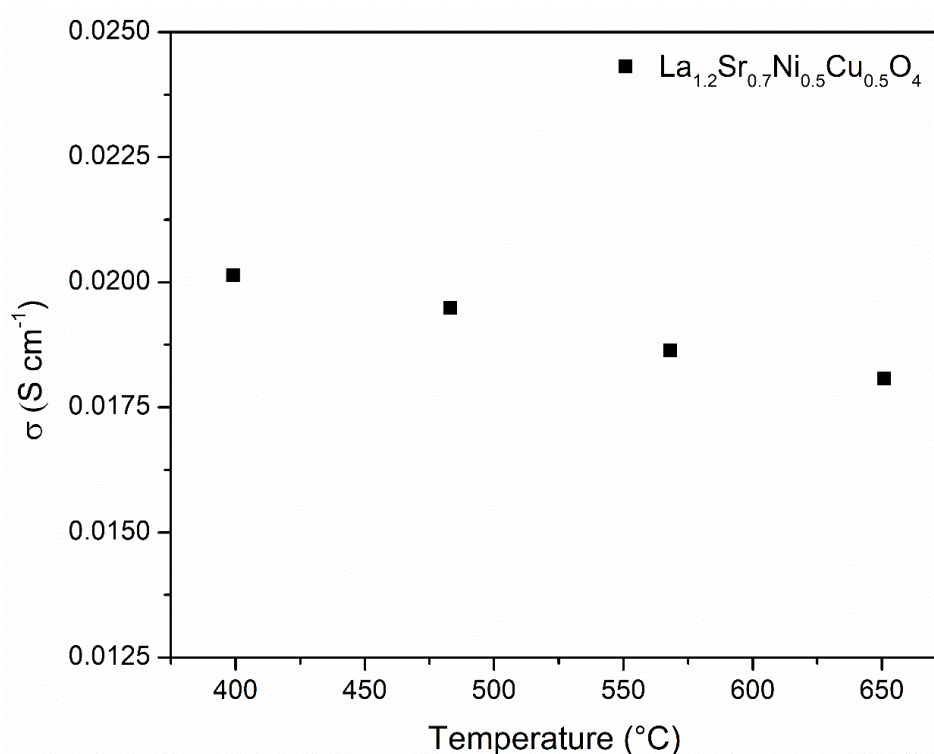
Activation energy values of 0.77 eV, 0.80 eV, and 0.52 eV were found for $\text{La}_{0.8}\text{Sr}_{0.2}\text{Ti}_{0.7}\text{Ni}_{0.2}\text{Cu}_{0.1}\text{O}_{3-\delta}$, $\text{La}_{0.8}\text{Sr}_{0.2}\text{Ti}_{0.7}\text{Ni}_{0.15}\text{Cu}_{0.15}\text{O}_{3-\delta}$ and $\text{La}_{0.8}\text{Sr}_{0.2}\text{Ti}_{0.7}\text{Ni}_{0.1}\text{Cu}_{0.2}\text{O}_{3-\delta}$, respectively. This indicates that the oxygen-ion vacancy migration plays a dominant role in the conduction process across all samples.

The presence of copper and nickel promotes an improvement of electrical properties of $\text{La}_{0.8}\text{Sr}_{0.2}\text{TiO}_{3-\delta}$ system, as the substitution of aliovalent ions at the B-site facilitates the mobility of charge carriers, thereby improving the total conductivity.

Moreover, these results are strongly supported by XPS analysis, as discussed previously, where the presence of Ti^{3+} was found to enhance the electrical properties. The $\text{Ti}^{3+}/\text{Ti}^{4+}$ proportion is 0.3, 0.3 and 0.2 for $\text{La}_{0.8}\text{Sr}_{0.2}\text{Ti}_{0.7}\text{Ni}_{0.2}\text{Cu}_{0.1}\text{O}_{3-\delta}$, $\text{La}_{0.8}\text{Sr}_{0.2}\text{Ti}_{0.7}\text{Ni}_{0.15}\text{Cu}_{0.15}\text{O}_{3-\delta}$ and $\text{La}_{0.8}\text{Sr}_{0.2}\text{Ti}_{0.7}\text{Ni}_{0.1}\text{Cu}_{0.2}\text{O}_{3-\delta}$ respectively. Hence, it was expected that $\text{La}_{0.8}\text{Sr}_{0.2}\text{Ti}_{0.7}\text{Ni}_{0.2}\text{Cu}_{0.1}\text{O}_{3-\delta}$ and $\text{La}_{0.8}\text{Sr}_{0.2}\text{Ti}_{0.7}\text{Ni}_{0.15}\text{Cu}_{0.15}\text{O}_{3-\delta}$ would exhibit better total conductivity due to the enhanced mobility through vacancies.

It is evident from the Arrhenius plot that the conduction mechanism in the RP phase differs significantly from that of titanate perovskites. **Figure 41** illustrates the total conductivity of the RP phase in static air. The maximum total conductivity occurs around 400 °C, after which it decreases with increasing temperature. This behavior is typical of metals, suggesting that electronic conductivity is much more dominant than ionic conductivity in this phase.

Figure 41: Total conductivity of $\text{La}_{1.2}\text{Sr}_{0.7}\text{Ni}_{0.5}\text{Cu}_{0.5}\text{O}_4$ from 400 °C to 650 °C in static air



The presence of $\text{Ni}^+/\text{Ni}^{2+}$ and $\text{Cu}^+/\text{Cu}^{2+}$ pairs, confirmed by XPS data, contributes to the enhancement of the electrical conductivity behavior and provides additional

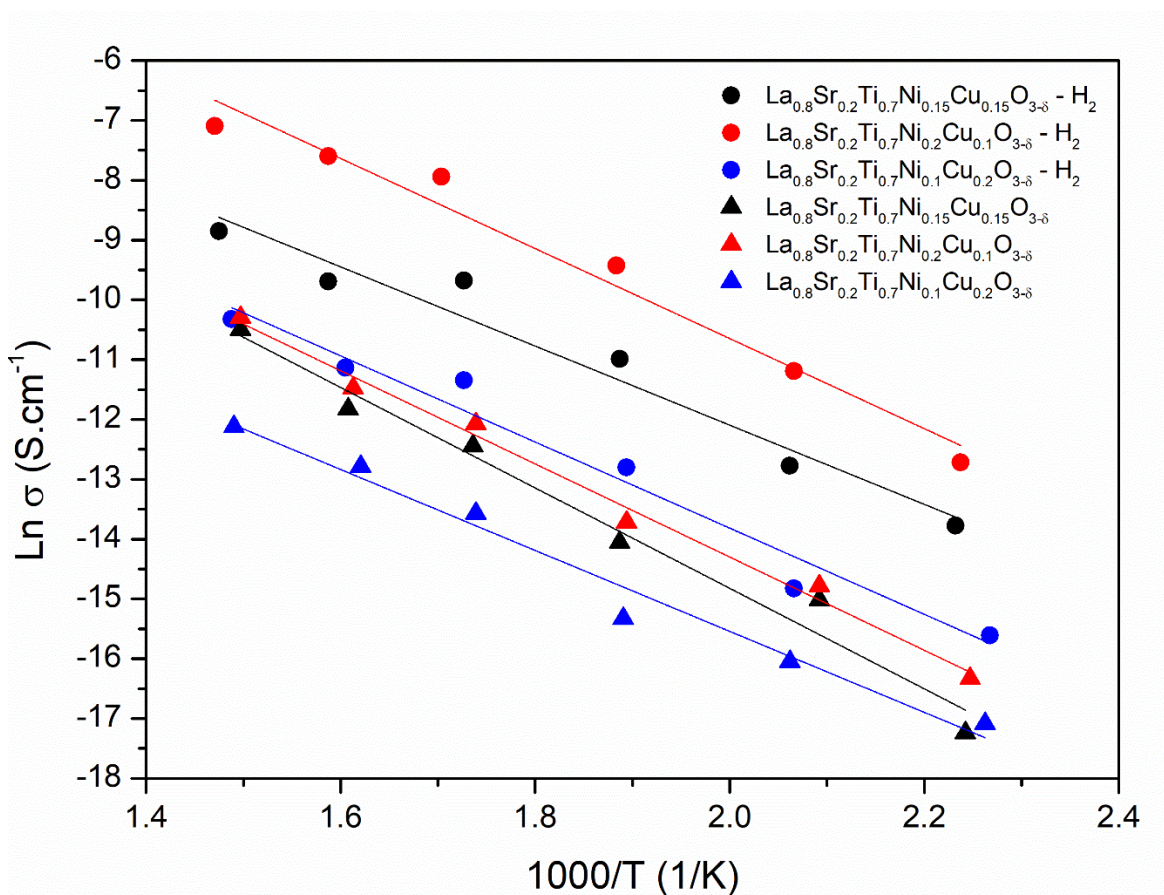
channels for electron hopping. **Table 6** provides information about the total conductivity and activation energy for the RP phase.

Table 6: Temperature (K), DC resistance ($\Omega \text{ cm}^{-1}$), and total conductivity (S cm^{-1}) and activation energy for $\text{La}_{1.2}\text{Sr}_{0.7}\text{Ni}_{0.5}\text{Cu}_{0.5}\text{O}_4$.

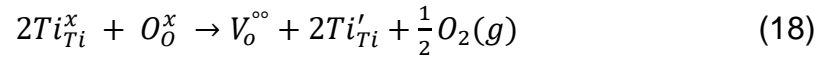
Sample	Temperature (K)	ρ_{DC} ($\Omega \text{ cm}^{-1}$)	σ (S cm^{-1})	E_a (eV)
$\text{La}_{1.2}\text{Sr}_{0.7}\text{Ni}_{0.5}\text{Cu}_{0.5}\text{O}_4$	672	49.64	2.01×10^{-2}	0.03
	756	51.32	1.95×10^{-2}	
	841	53.66	1.86×10^{-2}	
	924	55.34	1.81×10^{-2}	

Finally, to gain a better understanding of the electrical properties of titanates in a reducing atmosphere, electrochemical impedance spectroscopy measurements were conducted at low temperatures ($200^\circ\text{C} - 450^\circ\text{C}$) under a reducing atmosphere (standard mixture of 3% $\text{H}_2 - 97\% \text{N}_2$). **Figure 42** presents an Arrhenius plot comparing the measurements under a hydrogen atmosphere.

Figure 42: Arrhenius plot of total conductivity with variation of reciprocal temperature under 3% $\text{H}_2 - 97\% \text{N}_2$ atmosphere.



Notably, the total conductivity increased by approximately ~2 orders of magnitude in the hydrogen environment. This behavior has been previously observed and can be attributed to the reducing process of Ti^{4+} ions to Ti^{3+} , leading to the formation of oxygen vacancies. **Equation 18** represents the chemical equilibrium of vacancy formation.



Within these data, it was possible to determine the activation energy for the conduction process in a reducing atmosphere. The obtained values were 0.61 eV, 0.53 eV, and 0.58 eV, for $La_{0.8}Sr_{0.2}Ti_{0.7}Ni_{0.2}Cu_{0.1}O_{3-\delta}$, $La_{0.8}Sr_{0.2}Ti_{0.7}Ni_{0.15}Cu_{0.15}O_{3-\delta}$ and $La_{0.8}Sr_{0.2}Ti_{0.7}Ni_{0.1}Cu_{0.2}O_{3-\delta}$ respectively.

6. Conclusion

In summary, it was possible to synthesize the $\text{La}_{0.8}\text{Sr}_{0.2}\text{Ti}_{0.7}\text{Ni}_{0.3-x}\text{Cu}_x\text{O}_{3-\delta}$ ($x = 0.1, 0.15, 0.2$) and $\text{La}_{1.2}\text{Sr}_{0.7}\text{Ni}_{0.5}\text{Cu}_{0.5}\text{O}_{4-\delta}$ without the presence of second phases using the Pechini method. This was evaluated by X-ray diffraction (XRD), where the analysis confirmed the absence of additional phases, validating the results.

The Rietveld refinement technique was then employed to provide crucial information about lattice parameters, crystallite size, and strain in the crystal structure, thereby aiding in the understanding of structural changes that occurred after calcination. It was possible to verify that the increase of copper promoted a lattice parameter expansion and grew the crystal strain.

The samples were treated at various temperatures (900 °C, 850 °C, 800 °C, and 750 °C) for 10 hours in a reducing atmosphere, followed by XRD characterization. The Rietveld refinement offered a deeper understanding of all structural changes that occurred after this treatment and confirmed the presence of Copper-Nickel nanoparticles alloy in some compositions after reduction.

Strain and temperature directly influence the fraction of exsolved metallic nanoparticles, with higher reduction temperatures and greater strain leading to an increased fraction of metallic nanoparticles. As indicated by the refinement, the sample $\text{La}_{0.8}\text{Sr}_{0.2}\text{Ti}_{0.7}\text{Ni}_{0.1}\text{Cu}_{0.2}\text{O}_{3-\delta}$ was the most promising to exsolve nanoparticles due to the strain, and as expected it was the sample that exsolved in all temperatures.

Composition is, another factor that directly impacts the fraction of exsolved metal in the material. An increase in copper content appears to result in a higher fraction of metallic nanoparticles. This can be explained by the fact that copper is more easily reduced at higher temperatures and in a reduction atmosphere. As a result, the presence of copper in the composition promotes higher exsolution of metallic nanoparticles during the reduction process.

The XPS analysis confirmed the presence of the Cu^0 and Ni^0 species after reduction treatment as well as XRD data, corroborating the XRD data and confirming the successful production of exsolved nanoparticles. Besides that, the XPS data shed light on the $\text{Ti}^{4+}/\text{Ti}^{3+}$ pair, providing insights into the improved conduction observed in the $\text{La}_{0.8}\text{Sr}_{0.2}\text{Ti}_{0.7}\text{Ni}_{0.2}\text{Cu}_{0.1}\text{O}_{3-\delta}$ and $\text{La}_{0.8}\text{Sr}_{0.2}\text{Ti}_{0.7}\text{Ni}_{0.15}\text{Cu}_{0.15}\text{O}_{3-\delta}$ samples.

The Scanning Microscope images reveal the presence of spherical nanoparticles firmly anchored on the surface of the host solid oxide, providing visual confirmation of the findings from other analyses. The Transmission Electron Images further validate the presence of the Copper-Nickel alloy within the sample. However, to fully elucidate the dispersion of copper and nickel throughout the sample, an Energy Dispersive X-ray (EDX) analysis must be conducted. EDX analysis will provide elemental information and help gain a better understanding of the spatial distribution of copper and nickel within the sample.

The electrical properties of the titanate samples were measured, providing valuable insights into the transportation mechanisms. From the results obtained, it was possible to conclude that the titanates samples exhibit mixed ionic and electronic conduction, with ionic conduction predominating. On the other hand, RP phase demonstrates pure electronic conduction.

Additionally, measurements conducted under a reducing atmosphere resulted in an enhancement of total conduction. This improvement is likely attributed to the creation of oxygen vacancies and the presence of Ti^{3+} within the samples. The reduction process appears to play a significant role in enhancing the electrical properties of the titanates, making them more conductive under such conditions.

Finally, the material presents chemical and structural stability at reducing atmosphere, a fundamental feature of SOFC electrode. Besides that, present mixed ionic-electronic conductivity in reducing atmosphere, which is crucial for SOFC anodes. Thus, these materials are promising to be used as a SOFC anode.

7. Future work

- Fuel cell test
- Ethanol reforming catalysis test
- EDX - Transmission Electron Microscope aiming to investigate the nanoparticle chemical composition and dispersion.

8. Awards, congress, events, and schools

This work was awarded on the following event:

- Best poster in Material Science division – 46^a Brazilian Chemistry Society (46RASBQ) Águas de Lindoia – SP

This project was presented at the following events:

- XX B-MRS meeting, in Foz do Iguaçu – PR (Poster)
- 46^a Brazilian Chemistry Society (46RASBQ), in Águas de Lindoia – SP (Poster)
- CINE Conference 2022, in Campinas – SP (Poster)
- International Sirius Workshop on Heterogeneous and Hierarchical Materials (H2Mat) – (LNLS), Virtual. (Flash Talk)
- Escola Ricardo Rodrigues de Luz Síncrotron (ER2LS), in Campinas – SP (Poster)
- VII – Nanomat, in Santo André – SP (Poster)

Schools and courses:

- Escola Ricardo Rodrigues de Luz Síncrotron (ER2LS)
- Método de Rietveld 2022 (LCCEM), in Santo André – SP.
- III Escola de eletroquímica do Espírito Santo (UFES), in Vitória – ES
- Células a combustível de óxido sólido: princípio de funcionamento e modelagem
- Células a combustível de etanol direto: a influência da estrutura e do efeito eletrônico nos catalisadores

Bibliography

1. Allan, R. P., Hawikins, E., Belluin, N. & Collins, B. *IPCC, 2021: Summary for Policymakers*. <https://centaur.reading.ac.uk/101317/> (2021).
2. IEA. *Total energy supply by source*. <https://www.iea.org/data-and-statistics/data-browser?country=WORLD&fuel=Energy> (2021).
3. Hua, Y., Oliphant, M. & Hu, E. J. Development of renewable energy in Australia and China: A comparison of policies and status. *Renew. Energ.* **85**, 1044–1051 (2016).
4. Sakah, M., Diawuo, F. A., Katzenbach, R. & Gyamfi, S. Towards a sustainable electrification in Ghana: A review of renewable energy deployment policies. *Renewable Sustainable Energy Rev.* **79**, 544–557 (2017).
5. Scolaro, E. *et al.* Electrification of Agricultural Machinery: A Review. *IEEE Access* **9**, 164520–164541 (2021).
6. Zahedi, A. Australian renewable energy progress. *Renewable Sustainable Energy Rev.* **14**, 2208–2213 (2010).
7. Fan, Y. *et al.* In-situ Exsolved FeNi Nanoparticles on Perovskite Matrix Anode for Co-production of Ethylene and Power from Ethane in Proton Conducting Fuel Cells. *Electrochim. Acta* 139096 (2021) doi:10.1016/j.electacta.2021.139096.
8. Fan, W. *et al.* In situ growth of nanoparticles in A-site deficient ferrite perovskite as an advanced electrode for symmetrical solid oxide fuel cells. *J. Power Sources* **456**, 228000 (2020).
9. Li, B., Irvine, J. T. S., Ni, J. & Ni, C. High-performance and durable alcohol-fueled symmetrical solid oxide fuel cell based on ferrite perovskite electrode. *Appl. Energy* **306**, 118117–118128 (2022).
10. Wei, T., Liu, B., Jia, L. & Li, R. Perovskite materials for highly efficient catalytic CH₄ fuel reforming in solid oxide fuel cell. *INT. J. HYDROGEN ENERG.* **46**, 24441–24460 (2021).
11. Vidal, F. Produção e mercado de etanol. *scritório Técnico de Estudos Econômicos do Nordeste* 1–8 (2020).

12. Renewable Fuels Association. *Global Ethanol Production By Country or Region*.
<https://afdc.energy.gov/data/10331#:~:text=The%20United%20States%20is%20the,while%20Brazil%20primarily%20uses%20sugarcane.> (2021).
13. Sharifian, R., Wagterveld, R. M., Digdaya, I. A., Xiang, C. & Vermaas, D. A. Electrochemical carbon dioxide capture to close the carbon cycle. *Energ. Environ. Sci.* **14**, 781–814 (2021).
14. George, G., Ede, S. & Luo, Z. *Fundamentals of Perovskite Oxides*. vol. 1 (CRC Press, 2021).
15. Som, J. *et al.* Effect of substrate-induced lattice strain on the electrochemical properties of pulsed laser deposited nickel oxide thin film. *Mat. Sci. Eng. B-Solid* **280**, (2022).
16. Kim, H. *et al.* Ru-doped barium strontium titanates of the cathode for the electrochemical synthesis of ammonia. *Solid State Ion* **339**, (2019).
17. Mei, J., Liao, T. & Sun, Z. Metal exsolution engineering on perovskites for electrocatalysis: a perspective. *Mater Today Energy* **31**, (2023).
18. Abatzoglou, J. T., Williams, A. P. & Barbero, R. Global Emergence of Anthropogenic Climate Change in Fire Weather Indices. *Geophys Res Lett* **46**, 326–336 (2019).
19. Kang, J. N. *et al.* Energy systems for climate change mitigation: A systematic review. *Appl. Energy* **263**, (2020).
20. Our World in Data. Energy Production and Consumption. *Our World in Data* <https://ourworldindata.org/energy-production-consumption> (2021).
21. Our World in Data. Global average temperature anomaly. *Our World in Data* <https://ourworldindata.org/grapher/temperature-anomaly> (2019).
22. Habibollahzade, A., Gholamian, E., Ahmadi, P. & Behzadi, A. Multi-criteria optimization of an integrated energy system with thermoelectric generator, parabolic trough solar collector and electrolysis for hydrogen production. *Int J Hydrogen Energy* **43**, 14140–14157 (2018).
23. Ding, C., Shi, J., Wang, Z. & Li, C. Photoelectrocatalytic Water Splitting: Significance of Cocatalysts, Electrolyte, and Interfaces. *ACS Catal* **7**, 675–688 (2017).

24. Bao, C., Wang, Y., Feng, D., Jiang, Z. & Zhang, X. Macroscopic modeling of solid oxide fuel cell (SOFC) and model-based control of SOFC and gas turbine hybrid system. *Prog. Energy Combust. Sci.* **66**, 83–140 (2018).
25. Ramadhani, F., Hussain, M. A., Mokhlis, H. & Erixno, O. Solid Oxide Fuel Cell-Based Polygeneration Systems in Residential Applications: A Review of Technology, Energy Planning and Guidelines for Optimizing the Design. *Processes* **10**, (2022).
26. Boaro, M. & Aricò, A. S. *Advances in Medium and High Temperature Solid Oxide Fuel Cell Technology*. vol. 574 (2017).
27. Minh, N. Q. Ceramic Fuel Cells. *Journal of the American Ceramic Society* **76**, 563–588 (1995).
28. Wang, K. *et al.* A Review on solid oxide fuel cell models. *Int. J. Hydrog. Energy* **36**, 7212–7228 (2011).
29. Marcelo Linardi. *Introdução à ciência e tecnologia de Células a Combustível*. vol. 1 (ArtLiber, 2010).
30. Dunn, B., Kamath, H. & Tarascon, J. M. Electrical energy storage for the grid: A battery of choices. *Science (1979)* **334**, 928–935 (2011).
31. Wachsman, E. D. & Singhal, S. C. Solid Oxide Fuel Cell Commercialization, Research, and Challenges. *J. Electrochem. Soc.* **18**, 38–43 (2009).
32. A. ATKINSON *et al.* Advanced anodes for high-temperature fuel cells. *Nat Mater* **3**, 17–27 (2004).
33. Hanif, M. B. *et al.* Recent progress of perovskite-based electrolyte materials for solid oxide fuel cells and performance optimizing strategies for energy storage applications. *Mater. Res. Bull.* **146**, (2022).
34. Monama, G. R., Ramohlola, K. E., Iwuoha, E. I. & Modibane, K. D. Progress on perovskite materials for energy application. *Results Chem* **4**, 100321 (2022).
35. Mahato, N., Banerjee, A., Gupta, A., Omar, S. & Balani, K. Progress in material selection for solid oxide fuel cell technology: A review. *Prog. Mater. Sci.* **72**, 141–337 (2015).
36. Zarabi Golkhatmi, S., Asghar, M. I. & Lund, P. D. A review on solid oxide fuel cell durability: Latest progress, mechanisms, and study tools. *Renew. Sust. Energ. Rev.* **161**, 112339 (2022).

37. Arrivé, C., Delahaye, T., Joubert, O. & Gauthier, G. Exsolution of nickel nanoparticles at the surface of a conducting titanate as potential hydrogen electrode material for solid oxide electrochemical cells. *J Power Sources* **223**, 341–348 (2013).
38. da Silva, F. S. & de Souza, T. M. Novel materials for solid oxide fuel cell technologies: A literature review. *Int J Hydrogen Energy* **42**, 26020–26036 (2017).
39. Fan, M. S., Abdullah, A. Z. & Bhatia, S. Utilization of greenhouse gases through carbon dioxide reforming of methane over Ni-Co/MgO-ZrO₂: Preparation, characterization and activity studies. *Appl Catal B* **100**, 365–377 (2010).
40. Kilner, J. A. & Burriel, M. Materials for intermediate-temperature solid-oxide fuel cells. *Annu Rev Mater Res* **44**, 365–393 (2014).
41. Zhang, J., Lenser, C., Menzler, N. H. & Guillon, O. Comparison of solid oxide fuel cell (SOFC) electrolyte materials for operation at 500 °C. *Solid State Ion* **344**, (2020).
42. Ishihara, T. *Perovskite Oxide for Solid Oxide Fuel Cells*. (2009).
43. Touahra, F. *et al.* Enhanced catalytic behaviour of surface dispersed nickel on LaCuO₃ perovskite in the production of syngas: An expedient approach to carbon resistance during CO₂ reforming of methane. *Int J Hydrogen Energy* **41**, 2477–2486 (2016).
44. Vielstich, Wolf. *Handbook of fuel cells: fundamentals, technology, and applications*. (John Wiley & Sons, 2010).
45. Minh, N. Q. Solid oxide fuel cell technology - Features and applications. *Solid State Ion* **174**, 271–277 (2004).
46. Cao, T., Kwon, O., Gorte, R. J. & Vohs, J. M. Metal exsolution to enhance the catalytic activity of electrodes in solid oxide fuel cells. *Nanomaterials* **10**, 1–23 (2020).
47. Zhang, J., Gao, M. R. & Luo, J. L. In Situ Exsolved Metal Nanoparticles: A Smart Approach for Optimization of Catalysts. *Chem. Mater.* **32**, 5424–5441 (2020).
48. Cavazzani, J., Squizzato, E., Brusamarello, E. & Glisenti, A. Exsolution in Ni-doped lanthanum strontium titanate: a perovskite-based material for

- anode application in ammonia-fed Solid Oxide Fuel Cell. *Int J Hydrogen Energy* (2022) doi:10.1016/j.ijhydene.2022.02.133.
49. Gregor Hoogers. *Fuel Cell Technology Handbook*. (Society of Automotive Engineers, U.S., 2002).
 50. Dwivedi, S. Solid oxide fuel cell: Materials for anode, cathode and electrolyte. *Int J Hydrogen Energy* **45**, 23988–24013 (2020).
 51. Brian C. H. Steele & Angelika Heinzl. Materials for fuel-cell technologies. *Nature* **414**, 224–231 (2001).
 52. Arrivé, C., Delahaye, T., Joubert, O. & Gauthier, G. Exsolution of nickel nanoparticles at the surface of a conducting titanate as potential hydrogen electrode material for solid oxide electrochemical cells. *J Power Sources* **223**, 341–348 (2013).
 53. Shu, L. *et al.* Advanced perovskite anodes for solid oxide fuel cells: A review. *Int J Hydrogen Energy* **44**, 31275–31304 (2019).
 54. Chen, X. J., Khor, K. A., Chan, S. H. & Yu, L. G. Influence of microstructure on the ionic conductivity of yttria-stabilized zirconia electrolyte. *Mat. Sci. Eng. A-Struct.* **335**, 246–252 (2002).
 55. Yamamoto, O. Solid oxide fuel cells: fundamental aspects and prospects. *Electrochim. Acta* **45**, 2423–2435 (2000).
 56. Chen, Y., Orlovskaya, N., Andrew Payzant, E., Graule, T. & Kuebler, J. A search for temperature induced time-dependent structural transitions in 10 mol % Sc₂O₃ - 1 mol % CeO₂-ZrO₂ and 8 mol % Y₂O₃-ZrO₂ electrolyte ceramics. *J. Eur. Ceram. Soc.* **35**, 951–958 (2015).
 57. Brian C. H. Steele & Angelika Heinzl. Materials for fuel-cell technologies. *Nature* **414**, 224–231 (2001).
 58. Gao, Z., Mogni, L. v., Miller, E. C., Railsback, J. G. & Barnett, S. A. A perspective on low-temperature solid oxide fuel cells. *Energy Environ. Sci.* **9**, 1602–1644 (2016).
 59. Hattori, M. *et al.* Effect of aging on conductivity of yttria stabilized zirconia. *J Power Sources* **126**, 23–27 (2004).
 60. Butz, B. *et al.* Correlation between microstructure and degradation in conductivity for cubic Y₂O₃-doped ZrO₂. *Solid State Ion* **177**, 3275–3284 (2006).

61. Sun, J., Chengli, W., Song, L. & Shijun J. Cathode Materials $\text{LaNi}_{1-x}\text{CuO}_3$ for low temperature solid oxide fuel cells. *J. Korean Ceram. Soc.* **45**, 755–759 (2008).
62. Shi, H. *et al.* Building Ruddlesden – Popper and Single Perovskite Nanocomposites : A New Strategy to Develop High- Performance Cathode for Protonic Ceramic Fuel Cells. *Small* **17**, 2101872–2101881 (2021).
63. Kaur, P. & Singh, K. Review of perovskite-structure related cathode materials for solid oxide fuel cells. *Ceram. Int.* **46**, 5521–5535 (2020).
64. Yang, X., Xu, X., Wu, S., Yu, S. & Bi, L. Enhancing the performance of traditional $\text{La}_2\text{NiO}_{4+x}$ cathode for proton-conducting solid oxide fuel cells with Zn-doping. *Ceram. Int.* **48**, 19626–19632 (2022).
65. Petric, A., Huang, P. & Tietz, F. Evaluation of La-Sr-Co-Fe-O perovskites for solid oxide fuel cells and gas separation membranes. *Solid State Ion.* **135**, 719–725 (2000).
66. L.-W. Tai, M.M. Nasrallah, H.U. Anderson, D.M. Sparlin & S.R. Sehlin. Structure and electrical properties of $\text{La}_{1-x}\text{Sr}_x\text{Co}_{1-y}\text{Fe}_y\text{O}_3$. Part 2. The System $\text{La}_{1-x}\text{SrCo}_{0.2}\text{Fe}_{0.8}\text{O}_3$. *Solid State Ion* **76**, 273–283 (1995).
67. Teraoka, Y., Nobunaga, T., Okamoto, K., Miura, N. & Yamazoe, N. Influence of constituent metal cations in substituted LaCoO_3 on mixed conductivity and oxygen permeability. *Solid State Ion.* **48**, 207–212 (1991).
68. Yang, S. *et al.* Electrochemical performance and stability of cobalt-free $\text{Ln}_{1.2}\text{Sr}_{0.8}\text{NiO}_4$ (Ln=La and Pr) air electrodes for proton-conducting reversible solid oxide cells. *Electrochim Acta* **267**, 269–277 (2018).
69. Jacobson, A. J. Materials for solid oxide fuel cells. *Chem. Mat.* **22**, 660–674 (2010).
70. Laguna-Bercero, M. A. *et al.* Performance of $\text{La}_{2-x}\text{Sr}_x\text{Co}_{0.5}\text{Ni}_{0.5}\text{O}_{4 \pm \delta}$ as an oxygen electrode for solid oxide reversible cells. in *Fuel Cells* vol. 11 102–107 (2011).
71. Xie, W., Lee, Y. L., Shao-Horn, Y. & Morgan, D. Oxygen Point Defect Chemistry in Ruddlesden-Popper Oxides $(\text{La}_{1-x}\text{Sr}_x)_2\text{MO}_{4\pm?}$ (M = Co, Ni, Cu). *J. Phys. Chem. Lett.* **7**, 1939–1944 (2016).
72. Samara, G. A. The relaxational properties of compositionally disordered ABO₃ perovskites. *J. Phys.: Condens. Matter* **15**, 367–411 (2003).

73. Hwang, J. *et al.* Perovskites in catalysis and electrocatalysis. *Science* (1979) **358**, 751–756 (2017).
74. Chemical Structure: Perovskite. <https://the-gist.org/2020/01/perovskites-best-material-youve-never-heard-of/>.
75. Geller, S., Jeffries, J. B. & Curlander, P. J. The Crystal Structure of a New High-Temperature Modification of YGaO₃*. *Acta Cryst.* **31**, 2770 (1975).
76. Robert C. Liebermann, Leonie E. A. Jones & A. E. Ringwood. Elasticity of aluminate, titanate, stannate and germanate compounds with the Perovskite structure. *Phys. Earth Planet. Inter.* **14**, 165–178 (1977).
77. Park, S. *et al.* A sulfur-tolerant cathode catalyst fabricated with in situ exsolved CoNi alloy nanoparticles anchored on a Ruddlesden-Popper support for CO₂ electrolysis. *J Mater Chem A Mater* **8**, 138–148 (2020).
78. Ruddlesden, S. N. & Popper, P. The compound Sr₂TiO₇ and its structure. *Acta Cryst.* **11**, 54–55 (1958).
79. Bassat, J. M., Odier, P., Villesuzanne, A., Marin, C. & Pouchard, M. Anisotropic ionic transport properties in La₂NiO_{4+δ} single crystals. *Solid State Ion* **167**, 341–347 (2004).
80. Boehm, E. *et al.* Oxygen diffusion and transport properties in non-stoichiometric Ln₂ - XNiO₄ + δ oxides. *Solid State Ion* **176**, 2717–2725 (2005).
81. Druce, J., Ishihara, T. & Kilner, J. Surface composition of perovskite-type materials studied by Low Energy Ion Scattering (LEIS). *Solid State Ion* **262**, 893–896 (2014).
82. Wang, S., Tong, J., Cui, L., Zhang, P. & Zhou, F. A layered perovskite La_{1.5}Sr_{0.5}NiO_{4±δ}-molten carbonate dual-phase membrane for CO₂ capture from simulated flue gas. *J Memb Sci* **647**, (2022).
83. Jin, C., Yang, Z., Zheng, H., Yang, C. & Chen, F. La_{0.6}Sr_{1.4}MnO₄ layered perovskite anode material for intermediate temperature solid oxide fuel cells. *Electrochem commun* **14**, 75–77 (2012).
84. Chen, H. *et al.* Enhanced electrochemical performance of Cu-doped La₂NiO_{4+δ} cathode for solid oxide fuel cells. *Journal of Ceramic Science and Technology* **9**, 155–162 (2018).

85. Wang, S. *et al.* Evaluation of Cu-substituted $\text{La}_{1.5}\text{Sr}_{0.5}\text{NiO}_{4+\delta}$ as air electrode for CO_2 electrolysis in solid oxide electrolysis cells. *Ceram Int* **42**, 31509–31518 (2022).
86. Hui, S. & Petric, A. Evaluation of yttrium-doped SrTiO_3 as an anode for solid oxide fuel cells. *J. Eur. Ceram. Soc.* **22**, 1673–1681 (2002).
87. Mccolm, T. D. & Irvine, J. T. S. B-Site Doped Strontium Titanate as a Potential SOFC Substrate. *Ionics (Kiel)* **116**, 116–121 (2001).
88. Slater, P. R. & Irvine, J. T. S. Synthesis and Structure of New Perovskite Phase in the La-Ti-Al-O System. *J Solid State Chem* **146**, 437–348 (1999).
89. Ishihara, T., Matsuda, H. & Takita, Y. Doped LaGaO_3 Perovskite Type Oxide as a New Oxide Ionic Conductor. *J. Am. Chem. Soc* **116**, 3801–3803 (1994).
90. Ishihara, T., Matsuda, H. & Takita, Y. Effects of rare earth cations doped for La site on the oxide ionic conductivity of LaGaO_3 -based perovskite type oxide. *Solid Stat Ion.* **79**, 147–151 (1995).
91. Neagu, D. & Irvine, J. T. S. Perovskite Defect Chemistry as Exemplified by Strontium Titanate. in *Comprehensive Inorganic Chemistry II (Second Edition): From Elements to Applications* vol. 4 397–415 (Elsevier Ltd, 2013).
92. Neagu, D. & Irvine, J. T. S. Structure and properties of $\text{La}_{0.4}\text{Sr}_{0.4}\text{TiO}_3$ Ceramics for use as anode materials in solid oxide fuel cells. *Chemistry of Materials* **22**, 5042–5053 (2010).
93. Cai, W. *et al.* Sulfur-tolerant Fe-doped $\text{La}_{0.3}\text{Sr}_{0.7}\text{TiO}_3$ perovskite as anode of direct carbon solid oxide fuel cells. *Energy* **211**, (2020).
94. Bradha, M., Hussain, S., Chakravarty, S., Amarendra, G. & Ashok, A. Synthesis, structure and total conductivity of A-site doped $\text{LaTiO}_{3-\delta}$ perovskites. *J Alloys Compd* **626**, 245–251 (2015).
95. Miao, J.-P. *et al.* Structure characteristics and valence state study for La Na TiO synthesized under high-pressure and high-temperature conditions. *Mater. Lett.* **42**, 1–6 (2000).
96. Costa, A., Jorge, M. E. M., Carvalho, M. D., Gomes, A. & da Silva Pereira, M. I. $\text{LaNi}_{1-x}\text{Cu}_x\text{O}_3$ ($x = 0.05, 0.10, 0.30$) coated electrodes for oxygen evolution in alkaline medium. *J. Solid State Electrochem.* **17**, 2311–2318 (2013).

97. Alvarado Flores, J. J., Ávalos Rodríguez, M. L., Andrade Espinosa, G. & Alcaraz Vera, J. V. Advances in the development of titanates for anodes in SOFC. *Int. J. Hydrog. Energy* **44**, 12529–12542 (2019).
98. Moradi, G. R., Khosravian, F. & Rahmanzadeh, M. Effects of partial substitution of Ni by Cu in LaNiO₃ perovskite catalyst for dry methane reforming. *Chin. J. Catal.* **33**, 797–801 (2012).
99. Agência Nacional de Mineração. *Anuário Mineral Brasileiro*. www.anm.gov.br (2021).
100. Niemczyk, A. *et al.* High Cu content LaNi_{1-x}Cu_xO_{3-δ} perovskites as candidate air electrode materials for Reversible Solid Oxide Cells. *Int J Hydrogen Energy* **45**, 29449–29464 (2020).
101. Li, J., Zeng, J., Jia, L. & Fang, W. Investigations on the effect of Cu²⁺/Cu¹⁺ redox couples and oxygen vacancies on photocatalytic activity of treated LaNi_{1-x}Cu_xO₃ (x=0.1, 0.4, 0.5). *Int J Hydrogen Energy* **35**, 12733–12740 (2010).
102. Zheng, M., Liu, X. & Su, W. Preparation and performance of La_{1-x}Sr_xCuO_{3-δ} as cathode material in IT-SOFCs. *J Alloys Compd* **395**, 300–303 (2005).
103. Dubois, F., Odier, P. & Choisnet, J. Chemical reduction of LaNi_{0.5}Cu_{0.5}O₃: The oxygen deficient perovskite like cupronickelite LaNi_{0.5}Cu_{0.5}O_{2.25}. *J Mater Chem* **13**, 1737–1742 (2003).
104. British Geological Survey. *World Mineral Production 2016-2020*. (2020).
105. Kartharinal Punithavathy, I. *et al.* Impact of lanthanum ions on magnetic and dielectric properties of cobalt nanoferrites. *Journal of Materials Science: Materials in Electronics* **31**, 9783–9795 (2020).
106. Cheng, Z., Cui, Y., Yang, H. & Chen, Y. Effect of lanthanum ions on magnetic properties of Y₃Fe₅O₁₂ nanoparticles. *Journal of Nanoparticle Research* **11**, 1185–1192 (2009).
107. Shi, H., He, F. & Ye, J. Synthesis and structure of iron- and strontium-substituted octacalcium phosphate: Effects of ionic charge and radius. *J Mater Chem B* **4**, 1712–1719 (2016).
108. Bilgin, B., Atun, G. & Keçeli, G. Adsorption of strontium on illite. *J. Radioanal. Nucl. Chem.* **250**, 323–328 (2001).

109. Steiger, P., Kröcher, O. & Ferri, D. Increased nickel exsolution from LaFe_{0.8}Ni_{0.2}O₃ perovskite-derived CO₂ methanation catalysts through strontium doping. *Appl Catal A Gen* **590**, (2020).
110. Onrubia-Calvo, J. A., Pereda-Ayo, B., De-La-Torre, U. & González-Velasco, J. R. Strontium doping and impregnation onto alumina improve the NO_x storage and reduction capacity of LaCoO₃ perovskites. *Catal Today* **333**, 208–218 (2019).
111. Calì, E. *et al.* Exsolution of Catalytically Active Iridium Nanoparticles from Strontium Titanate. *ACS Appl Mater Interfaces* **12**, 37444–37453 (2020).
112. Steiger, P., Kröcher, O. & Ferri, D. Increased nickel exsolution from LaFe_{0.8}Ni_{0.2}O₃ perovskite-derived CO₂ methanation catalysts through strontium doping. *Appl Catal A Gen* **590**, (2020).
113. Neagu, D. & Irvine, J. T. S. Enhancing electronic conductivity in strontium titanates through correlated A and B-site doping. *Chem. Mat.* **23**, 1607–1617 (2011).
114. Cai, W. *et al.* Sulfur-tolerant Fe-doped La_{0.3}Sr_{0.7}TiO₃ perovskite as anode of direct carbon solid oxide fuel cells. *Energy* **211**, (2020).
115. Li, S., Hao, X., Abudula, A. & Guan, G. Nanostructured Co-based bifunctional electrocatalysts for energy conversion and storage: Current status and perspectives. *J Mater Chem A Mater* **7**, 18674–18707 (2019).
116. Wang, X. *et al.* Nanostructured hexaazatrinaphthalene based polymers for advanced energy conversion and storage. *Chem. Eng. J.* **427**, 130995 (2022).
117. Chauhan, I., Yasir, M., Verma, M. & Singh, A. P. Nanostructured lipid carriers: A groundbreaking approach for transdermal drug delivery. *Adv. Pharm. Bull.* **10**, 150–165 (2020).
118. Shit, S. C. *et al.* Integrated nano-architected photocatalysts for photochemical CO₂ reduction. *Nanoscale* **12**, 23301–23332 (2020).
119. Liu, Y. *et al.* Promises and prospects of two-dimensional transistors. *Nature* **591**, 43–53 (2021).
120. Lindsay, S. M. *Introduction to nanoscience*. vol. 1 (Oxford, 2010).
121. Zanella, R., Delannoy, L. & Louis, C. Mechanism of deposition of gold precursors onto TiO₂ during the preparation by cation adsorption and

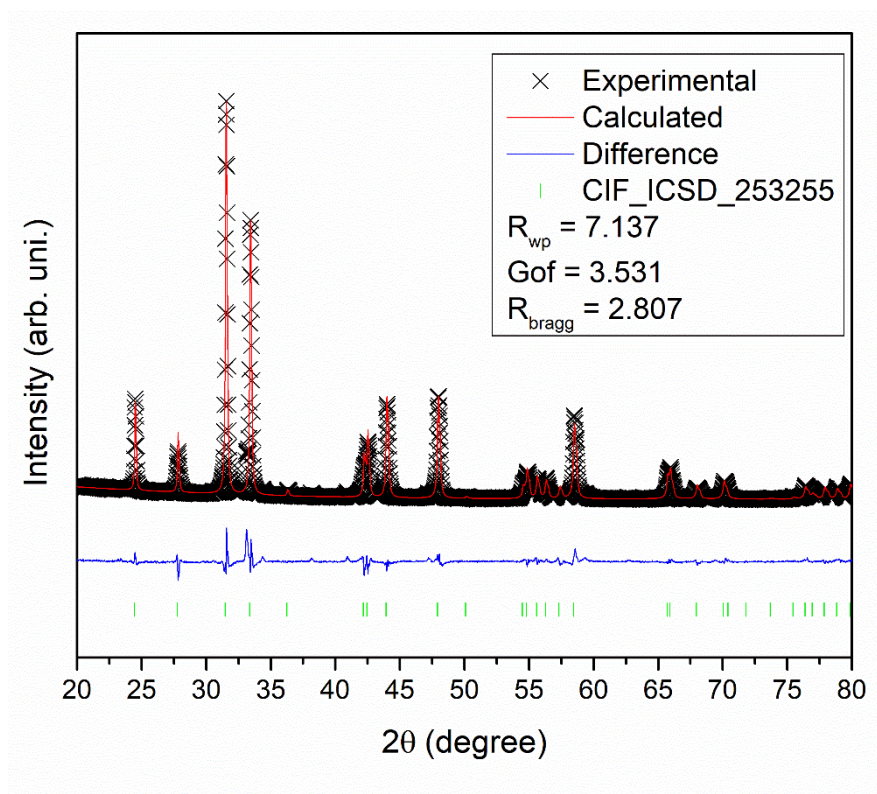
- deposition-precipitation with NaOH and urea. in *Applied Catalysis A: General* vol. 291 62–72 (2005).
122. Guzman, J. & Gates, B. C. Simultaneous presence of cationic and reduced gold in functioning MgO-supported CO oxidation catalysts: Evidence from X-ray absorption spectroscopy. *Journal of Physical Chemistry B* **106**, 7659–7665 (2002).
 123. Bamwenda, G. R., Tsubota, S., Nakamura, T. & Haruta, M. *The influence of the preparation methods on the catalytic activity of platinum and gold supported on TiO₂ for CO oxidation.*
 124. Thommy, L., Joubert, O., Hamon, J. & Caldes, M. T. Impregnation versus exsolution: Using metal catalysts to improve electrocatalytic properties of LSCM-based anodes operating at 600 °C. *Int J Hydrogen Energy* **41**, 14207–14216 (2016).
 125. Lu, J. *et al.* Coking- and sintering-resistant palladium catalysts achieved through atomic layer deposition. *Science* (1979) **335**, 1205–1208 (2012).
 126. Haruta, M. *Catalysis of gold nanoparticles deposited on metal oxides.* vol. 6 (2002).
 127. Zheng, N. & Stucky, G. D. A general synthetic strategy for oxide-supported metal nanoparticle catalysts. *J Am Chem Soc* **128**, 14278–14280 (2006).
 128. Kousi, K., Tang, C., Metcalfe, I. S. & Neagu, D. Emergence and future of exsolved materials. *Small* **17**, (2021).
 129. Kousi, K. *et al.* Low temperature methane conversion with perovskite-supported: exo / endo -particles. *J Mater Chem A Mater* **8**, 12406–12417 (2020).
 130. Neagu, D. *et al.* Nano-socketed nickel particles with enhanced coking resistance grown in situ by redox exsolution. *Nat Commun* **6**, (2015).
 131. Kwon, O., Joo, S., Choi, S., Sengodan, S. & Kim, G. Review on exsolution and its driving forces in perovskites. *JPhys Energy* **2**, (2020).
 132. Gao, Y., Chen, D., Saccoccio, M., Lu, Z. & Ciucci, F. From material design to mechanism study: Nanoscale Ni exsolution on a highly active A-site deficient anode material for solid oxide fuel cells. *Nano Energy* **27**, 499–508 (2016).

133. Hamada, I., Uozumi, A., Morikawa, Y., Yanase, A. & Katayama-Yoshida, H. A density functional theory study of self-regenerating catalysts $\text{LaFe}_{1-x}\text{M}_x\text{O}_{3-y}$ ($\text{M} = \text{Pd}, \text{Rh}, \text{Pt}$). *J Am Chem Soc* **133**, 18506–18509 (2011).
134. Katz, M. B. *et al.* Self-regeneration of Pd-LaFeO₃ catalysts: New insight from atomic-resolution electron microscopy. *J Am Chem Soc* **133**, 18090–18093 (2011).
135. Błaszczak, P., Łapiński, M., Wang, S. F., Jasiński, P. & Bochentyn, B. Exsolution of Ni nanoparticles on the surface of cerium and nickel co-doped lanthanum strontium titanate as a new anodic layer for DIR-SOFC. Anti-coking potential and H₂S poisoning resistance of the prepared material. *Int J Hydrogen Energy* **45**, 29186–29200 (2020).
136. Li, H. *et al.* Exsolved Alloy Nanoparticles Decorated Ruddlesden-Popper Perovskite as Sulfur-Tolerant Anodes for Solid Oxide Fuel Cells. *Energy and Fuels* **34**, 11449–11457 (2020).
137. Neagu, D. *et al.* In Situ Observation of Nanoparticle Exsolution from Perovskite Oxides: From Atomic Scale Mechanistic Insight to Nanostructure Tailoring. *ACS Nano* **13**, 12996–13005 (2019).
138. Neagu, D., Tsekouras, G., Miller, D. N., Ménard, H. & Irvine, J. T. S. In situ growth of nanoparticles through control of non-stoichiometry. *Nat Chem* **5**, 916–923 (2013).
139. Gao, Y. *et al.* Energetics of Nanoparticle Exsolution from Perovskite Oxides. *Journal of Physical Chemistry Letters* **9**, 3772–3778 (2018).
140. Jo, Y. R. *et al.* Growth Kinetics of Individual Co Particles Ex-solved on $\text{SrTi}_{0.75}\text{Co}_{0.25}\text{O}_{3-\delta}$ Polycrystalline Perovskite Thin Films. *J Am Chem Soc* **141**, 6690–6697 (2019).
141. Barsoum, M. W. *Fundamentals of Ceramics*. vol. 1 (Institute of Physics Publishing, 2003).
142. Li, J., Yu, Y., Yin, Y. M., Zhou, N. & Ma, Z. F. A novel high performance composite anode with in situ growth of Fe-Ni alloy nanoparticles for intermediate solid oxide fuel cells. *Electrochim Acta* **235**, 317–322 (2017).
143. Wang, Z. *et al.* Improving electrochemical performance of $(\text{Cu}, \text{Sm})\text{CeO}_2$ anode with anchored Cu nanoparticles for direct utilization of natural gas in solid oxide fuel cells. *J. Eur. Ceram. Soc.* **42**, 3254–3263 (2022).

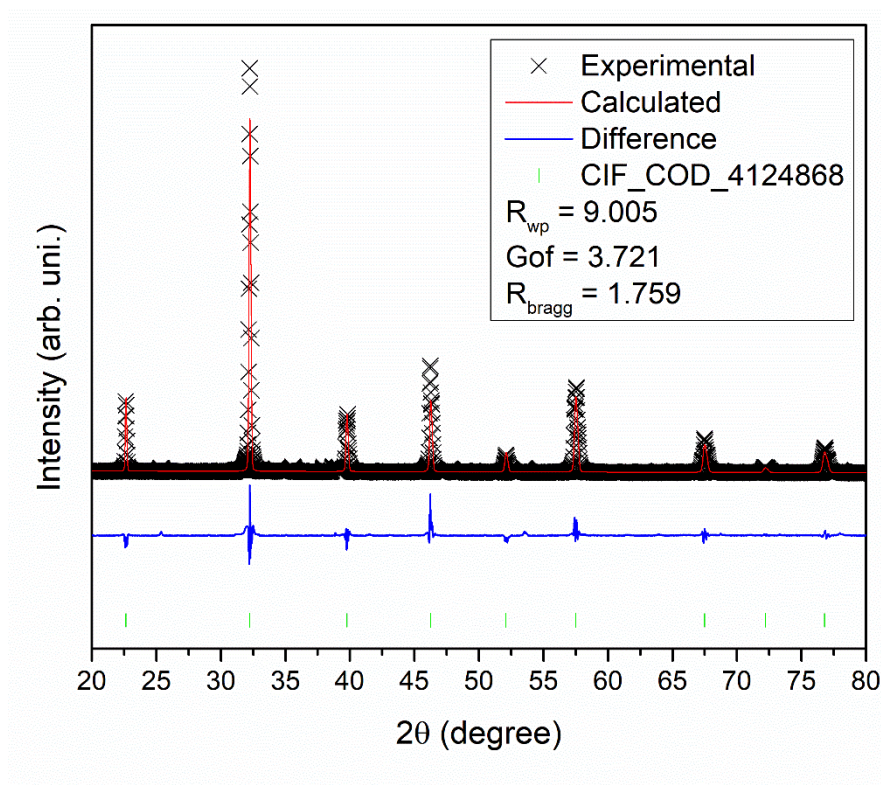
144. Papargyriou, D., Miller, D. N. & Irvine, J. T. S. Exsolution of Fe-Ni alloy nanoparticles from (La,Sr)(Cr,Fe,Ni)O₃ perovskites as potential oxygen transport membrane catalysts for methane reforming. *J Mater Chem A Mater* **7**, 15812–15822 (2019).
145. Spring, J. *et al.* Toward Controlling Filament Size and Location for Resistive Switches via Nanoparticle Exsolution at Oxide Interfaces. *Small* **16**, (2020).
146. Tang, C., Kousi, K., Neagu, D. & Metcalfe, I. S. Trends and Prospects of Bimetallic Exsolution. *Chemistry - A European Journal* vol. 27 6666–6675 Preprint at <https://doi.org/10.1002/chem.202004950> (2021).
147. Lu, J. *et al.* Highly efficient electrochemical reforming of CH₄/CO₂ in a solid oxide electrolyser. <https://www.science.org> (2018).
148. Sun, X. *et al.* Progress of Exsolved Metal Nanoparticles on Oxides as High Performance (Electro)Catalysts for the Conversion of Small Molecules. *Small* vol. 17 Preprint at <https://doi.org/10.1002/sml.202005383> (2021).
149. Li, S., Qin, Q., Xie, K., Wang, Y. & Wu, Y. High-performance fuel electrodes based on NbTi_{0.5}M_{0.5}O₄ (M = Ni, Cu) with reversible exsolution of the nano-catalyst for steam electrolysis. *J Mater Chem A Mater* **1**, 8984–8993 (2013).
150. Spring, J. *et al.* Toward Controlling Filament Size and Location for Resistive Switches via Nanoparticle Exsolution at Oxide Interfaces. *Small* **16**, (2020).
151. Engelhard, M. H., Baer, D. R., Herrera-Gomez, A. & Sherwood, P. M. A. Introductory guide to backgrounds in XPS spectra and their impact on determining peak intensities. *Journal of Vacuum Science & Technology A* **38**, 063203 (2020).
152. Biesinger, M. C., Payne, B. P., Lau, L. W. M., Gerson, A. & Smart, R. S. C. X-ray photoelectron spectroscopic chemical state Quantification of mixed nickel metal, oxide and hydroxide systems. *Surface and Interface Analysis* **41**, 324–332 (2009).
153. Shirley, D. A. High-Resolution X-Ray Photoemission Spectrum of the Valence Bands of Gold. *Phys Rev B* **5**, 4709–4714 (1972).
154. Kuhn, M., Hashimoto, S., Sato, K., Yashiro, K. & Mizusaki, J. Oxygen nonstoichiometry, thermo-chemical stability and lattice expansion of La_{0.6}Sr_{0.4}FeO_{3-δ}. *Solid State Ion* **195**, 7–15 (2011).

155. Zhu, T., Troiani, H. E., Mogni, L. v., Han, M. & Barnett, S. A. Ni-Substituted Sr(Ti,Fe)O₃ SOFC Anodes: Achieving High Performance via Metal Alloy Nanoparticle Exsolution. *Joule* **2**, 478–496 (2018).
156. Cullity, B. D. *Elements of x-ray diffraction*. (Addison-Wesley Publishing Company, Inc, 1978).
157. Nenning, A. & Fleig, J. Electrochemical XPS investigation of metal exsolution on SOFC electrodes: Controlling the electrode oxygen partial pressure in ultra-high-vacuum. *Surf Sci* **680**, 43–51 (2019).
158. Amaya, Á. A., González, C. A., Niño-Gómez, M. E. & Martínez O., F. XPS fitting model proposed to the study of Ni and La in deactivated FCC catalysts. *J Electron Spectros Relat Phenomena* **233**, 5–10 (2019).
159. Tucker, M. C. Progress in metal-supported solid oxide fuel cells: A review. *J. Power Sources* **195**, 4570–4582 (2010).
160. Ding, P. *et al.* Review on Ruddlesden-Popper perovskites as cathode for solid oxide fuel cells. *JPhys Materials* **4**, (2021).
161. Bradha, M., Hussain, S., Chakravarty, S., Amarendra, G. & Ashok, A. Synthesis, structure and total conductivity of A-site doped LaTiO_{3-δ} perovskites. *J Alloys Compd* **626**, 245–251 (2015).

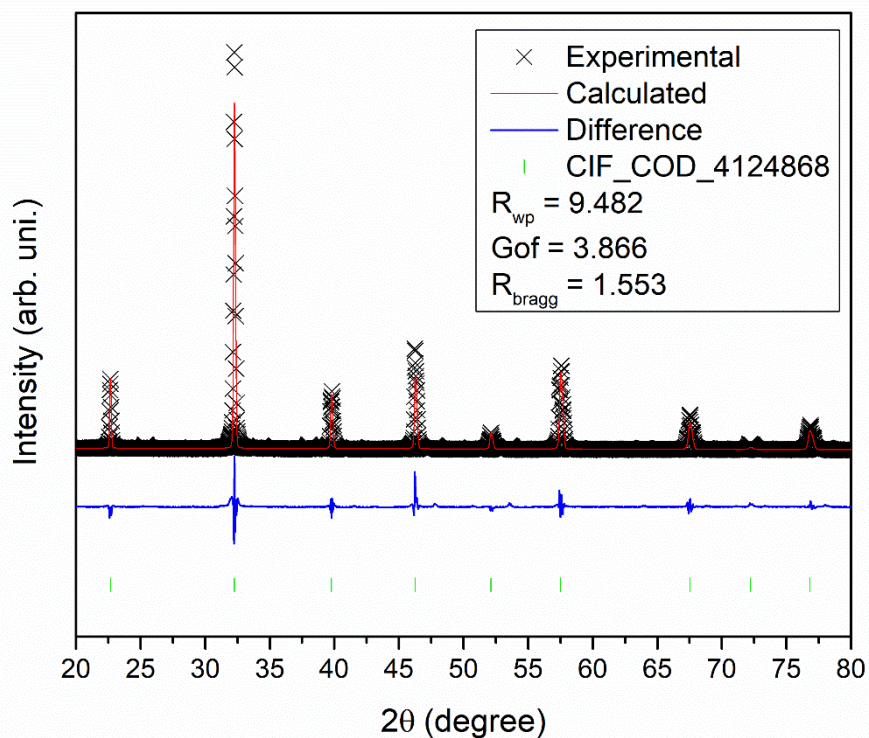
Appendix 1



S.1 – Rietveld pattern refinement of $\text{La}_{1.2}\text{Sr}_{0.7}\text{Ni}_{0.5}\text{Cu}_{0.5}\text{O}_{4\pm\delta}$ as the tetragonal phase (I4/mmm). The observed XRD pattern is shown with x points within the theoretical model, the blue line shows the difference between the theoretical model and the experimental data. Finally, the expected peaks positions are shown above in green bars.



S.2 – Rietveld pattern refinement of $\text{La}_{0.8}\text{Sr}_{0.2}\text{Ti}_{0.7}\text{Ni}_{0.15}\text{Cu}_{0.15}\text{O}_{3-\delta}$ as the cubic phase (Pm-3m). The observed XRD pattern is shown with x points within the theoretical model, the blue line shows the difference between the theoretical model and the experimental data. Finally, the expected peaks positions are shown above in green bars.



S.3 – Rietveld pattern refinement of $\text{La}_{0.8}\text{Sr}_{0.2}\text{Ti}_{0.7}\text{Ni}_{0.2}\text{Cu}_{0.1}\text{O}_{3-\delta}$ as the cubic phase (Pm-3m). The observed XRD pattern is shown with x points within the theoretical model, the blue line shows the difference between the theoretical model and the experimental data. Finally, the expected peaks positions are shown above in green bars.